Design and Implementation of a grid-connected variable-speed PM WECS

By: Stefan Thomas Sager

Thesis submitted to the Department of Electrical Engineering, University of Cape Town, in complete fulfilment of the requirements for the degree of Master of Science in Electrical Engineering

31st of March 2010

Declaration

This thesis is submitted to the Department of Electrical Engineering, University of Cape Town, in complete fulfilment of the requirements for the degree of Master of Science in Electrical Engineering. It has not been submitted before for any degree or examination at this or any other university.

"I know the meaning of plagiarism and declare that all the work in the document, save for that which is properly acknowledged, is my own."

S.T. Sager

31st of March 2010

Acknowledgments

I would like to thank my family for their continuous support throughout my time at UCT. They have been more than generous in their support and encouragement.

My sincere thanks go to my supervisor Dr. M.A Khan and my co-supervisor, Dr. P. Barendse. They have been great mentors and supported me with their guidance throughout this project.

To my fellow members of the AMES group, you have been very good colleagues and hopefully will remain so in the future.

Special thanks go to Chris Wozniak and Phillip Titus, who have been extremely helpful during the long hours in the laboratory and without whom I could not have completed this work.

The financial support provided by the University of Cape Town, the AMES group and the Centre for Renewable Energy Studies is gratefully acknowledged.

Finally, to all my friends, who have been there for me over the past six years, I am very grateful and privileged to have shared this part of my life with you. May this only be the beginning of many more years to come.

Abstract

As renewable energy (RE) sources are increasingly becoming an integral part of the world's power generation capacity, they are becoming more sophisticated and provide a solid platform for power generation today. Wind Energy is the fastest growing RE source. The correct understanding of issues associated with this technology and how to address them is integral in furthering this RE source.

A turbine emulator has been developed and implemented in the laboratory to effectively test the developed system in a controlled environment. This has been achieved through use of a torque controlled DC-machine which emulates the behaviour of a turbine.

The main objective of the work presented in this thesis is the full understanding and implementation of a PM Wind Turbine System. Focus is on a grid-tied Surface Mounted PM Wind Generator, which operates at variable speed without making use of pitch control. The operating conditions of the machine are fully controlled through power electronic converters which also provide the grid connection. Both power converters, on the machine-side and the grid-side are controlled through Space Vector Modulation (SVM).

The control of the PM generator is implemented and investigated in simulation and experimentally. Maximising the energy output under different wind conditions is investigated. Maximum Power Point Tracking (MPPT) is implemented to extract maximum power from the incident wind. Three different control strategies for the operation of the generator are investigated and their impact on generator efficiency investigated.

The grid-connection is provided through a LCL-type grid-filter between the power converter and a step-down transformer to reduce the grid voltage.

A thorough review of work done on this WECS topology has been carried out and the different approaches have been simulated and implemented experimentally in the laboratory.

Certain limitations were encountered which are discussed and addressed in the thesis.

Contents

List of Figures

List of Tables

List of Abbreviations

ADC	-	Analogue to Digital Converter
DAC	-	Digital to Analgoue Converter
d-axis	-	Direct axis (rotor pole axis)
DFIG	-	Doubly-fed Induction Generator
EMF	-	Electromotive force
HCC	-	Hysteresis Current Control
IG	-	Induction Generator
IPMSG	-	Interior Permanent Magnet Synchronous Generator
LEM	-	Line Entrance Module
LMA	-	Loss Minimisation Algorithm
LP	-	Low-pass
MPP	-	Maximum power point
MPPT	-	Maximum power point tracking
PLL	-	Phase-lock loop
PM	-	Permanent magnet
PMs	-	Permanent magnets
PMSG	-	Permaneng Magnet Synchronous Generator
PMSGs	-	Permaneng Magnet Synchronous Generators
PMSM	-	Permaneng Magnet Synchronous Machine
PWM	-	Pulse-Width Modulation
q-axis	-	quadrature axis (rotor inter-pole axis)
RMS	-	Root mean square
SV	-	Space-Vector
SVM	-	Space-Vector-Modulation
TSR	-	Tip-speed-ratio
UPF	-	Unity power factor
WECS	-	Wind Energy Conversion System
WRSG	-	Wound-Rotor Synchronous Generator

List of Symbols

Symbol	Unit	Definition
A	m^2	Area
B_{max}^{n}	*T*	Peak flux density
C_b	*F*	Base capacitance
C_f	*F*	Filter capacitance
C_p		Power Coefficient
f_{grid}	*Hz*	Grid frequency
f_{res}	*Hz*	Resonant frequency
f_{sw}	*Hz*	Switching frequency
i_d	*A*	d- axis current component
i_d^*	*A*	d-axis reference current component
I_{DC}	*A*	DC-link current
i_{dg}	*A*	d-axis component of grid current
i_{ds}	*A*	d-axis component of stator current
I_m	*A*	Mean current
i_{od}	*A*	d-axis current component
i_{oq}	*A*	q-axis current component
$I_{Ph,RMS}$	*A*	Phase RMS current
i_q	*A*	q-axis current component
i_{qs}	*A*	q-axis component of stator
I_{rated}	*A*	rated current
i_{ripm}	*A*	Mean value of ripple current
$J_{generator}$	kgm^2	Generator inertia
$J_{turbine}$	kgm^2	Turbine inertia
K_c	$W/Wbturns^2$	Core loss constant
K_n		Polynomial coefficient
L_b	*H*	Base inductance
L_d	*H*	d-axis inductance
L_g	*H*	Grid inductance
L_{gen}	*H*	Generator side inductance
L_{grid}	*H*	Grid side inductance

Symbol	Unit	Definition
L_{inv}	*H*	Inverter side inductance
L_q	*H*	q-axis inductance
L_s	*H*	Stator inductance
m_a		Modulation ratio
P_{Cu}	*W*	Copper losses
P_{DC}	*W*	DC Power
P_{Fe}	*W*	Iron losses
P_{Gen}	*W*	Real generator power
P_{grid}	*W*	Real grid power
P_{loss}	*W*	Losses
P_{mec}	*W*	Mechanical power
p_n		Pole number
$P_{rectifier}$	*W*	Rectifier losses
P_{Res}	*W*	Resistive losses
P_{shaft}	*W*	Shaft power
$P_{turbine}$	*W*	Turbine power
R_a	*Ω*	Armature resistance
R_C	*Ω*	Core loss resistance
R_s	*Ω*	Stator resistance
r_s	*Ω*	Stator resistance
S_n	*W*	Rated absolute power
T_{em}	*Nm*	Electromagnetic torque
$T_{friction\ ,windage}$	*Nm*	Friction and windage torque
T_g	*Nm*	Generator torque
$T_{generator}$	*Nm*	Generator torque
T_m	*Nm*	Mechanical torque
T_{shaft}	*Nm*	Shaft torque
T_{tower}	*Nm*	Tower torque
$T_{turbine}$	*Nm*	Turbine torque
U_{DC}	*V*	DC-voltage
U_n	*V*	Rated RMS voltage
v_d	*V*	d-axis voltage component
V_{DC}	*V*	DC-voltage

Symbol	Unit	Definition
v_{dg}	*V*	d-axis voltage component of grid
v_q	*V*	q-axis voltage component
v_{wind}	*m/s*	Wind speed
W_c	W	Core losses
W_{core}	W	Core losses
W_{cu}	W	Copper losses
W_{Fe}	W	Iron losses
W_{loss}	W	Total losses
X_S	*Ω*	Stator reactance
Z_b	*Ω*	Base impedance
η_{Gen}	*%*	Generator Efficiency
η_{system}	*%*	System Efficiency
θ_e	*rad*	electrical phase angle
θ_m	*rad*	mechanical angle
λ_d	*Wb-turns*	d-axis flux linkage
λ_{opt}	*Wb-turns*	optimum tip-speed ratio
λ_{pm}	*Wb-turns*	Permanent magnet excitation
λ_q	*Wb-turns*	q-axis flux linkage
λ_s	*Wb-turns*	stator flux linkage
ξ_{lim}		demagnetising coefficient
τ_d	*s*	d-axis time constant
τ_q	*s*	q-axis time constant
ψ_S	*Wb-turns*	Stator flux linkage
ω_b	*rad/s*	Base speed
ω_e	*rad/s*	Electrical frequency
ω_{gen}	*rad/s*	Generator speed
ω_{opt}	*rad/s*	Optimum turbine speed
$\omega_{Ref,MPPT}$	*rad/s*	MPPT reference speed
ω_{shaft}	*rad/s*	Shaft Speed
$\dot{\omega}_{turbine}$	*rad/s*^{2}	Turbine acceleration

Chapter 1

Introduction

1.1. Background

Wind power has been captured and used for hundreds of years in various ways. Its applications include water pumping, milling grain and various other applications which make use of the kinetic energy present in the wind.

The first wind turbine used to generate electricity was built in Scotland in 1887. From that moment on wind turbine technology has evolved steadily. Initial projects focused on rural applications where an independent source of electricity was required, but the first Megawatt Turbine was built in 1941 in Vermont, USA. In spite of the long history of technological development, wind energy and renewable energy sources in general have only really been developed on a large commercial scale over the past 30 years, since the oil crisis in 1970. Wind energy has since developed into a main-stream business sector and is currently the world's fastest growing renewable energy source. The main reason for this is the fast depletion of the world's fossil fuel resources and the growing awareness of the environmental impact of fossil fuels.

Many countries are now investing in and subsidising the development of renewable energy sources in order to reduce their dependence on fossil fuels.

One of the most important aspects associated with development of renewable energy sources is to make them economically competitive. Numerous factors have to be considered to achieve this. Non-technical factors include policy framework and financial support from the responsible bodies such as the government. Improving the efficiency of WECS is an important area which requires attentions. Especially in

areas with low wind speeds any efficiency improvements contribute to making wind energy systems more viable and strengthen their competitiveness. This is the motivation behind the work presented in this thesis.

1.2. Literature Review

A variety of different Wind Energy Conversion System (WECS) Topologies are proposed in the literature. These systems use different types of generators, drive-trains and power electronic converters, and can be configured as stand-alone or grid-tied systems. Furthermore, there are constant, semi-constant as well as variable speed systems. The focus of this work is on the variable-sped grid-tied permanent magnet synchronous wind turbine system. A review of literature on such systems is presented here while a more in depth analysis is presented in chapter 2 and 3.

Variable-Speed Permanent Magnet Synchronous WECSs are connected to the grid by means of a converter which has a machine-side rectifier and a grid-side inverter. There are two main converter topologies available which include an active rectifier plus full-bridge inverter or a diode-bridge rectifier plus full-bridge inverter. All systems found in literature need to make use of a full-bridge inverter with vector control on the grid-side in order to synchronise the output and control the power flow to the grid.

In systems which use a passive diode-bridge rectifier only the active power drawn from the machine can be controlled and hence the operating speed. This allows for Maximum Power Point Tracking (MPPT) to obtain maximum aerodynamic power from the turbine, but does not allow for more efficient control of the generator itself. Such configurations are used in smaller WECSs, where the power loss due to uncontrollable operating variables of the generator are low and therefore does not justify the additional cost of a full active machine-side converter. Power Factor and Machine Efficiency cannot be controlled directly as is the case in systems with an active machine-side converter.
A 25kW WECS employing a diode-bridge rectifier in conjunction with a DC/DC boost converter and a VSI to connect the system to the grid is discussed in [1]. The author discusses the relationship between i_d and i_q and argues that under steady-state conditions and ignoring the diode rectifier's commutation phenomena, the power factor is constantly equal to unity. This imposes a maximum values on the developed

torque which is decreased by the leakage inductance of the machine. This can be considerably large when using a surface-mounted generator. A similar system is presented and analysed in [2], where a diode-bridge rectifier and a DC boost chopper is supplying a DC-Link.
In both the aforementioned works, the generator speed is controlled by controlling the DC/DC converter's duty cycle and therefore the power flow from the generator. This controls the current in the machine, thereby controlling the developed torque. By controlling the developed torque the machine's speed can be controlled and the maximum power point (MPP) is tracked.

For systems in which the generator is controlled by an active rectifier there are several control approaches. Such systems usually make use of a back-to-back converter configuration. This allows for independent control of the generator's d- and q-axis current components. In Surface Mounted PM machines the d-axis current component has traditionally been set to zero in order to minimise the current required at a desired torque level. Furthermore this technique reduces the demagnetising effect on the magnets due to the magnetising (d-axis) current component. Due to improvement in modern magnets the magnetising current can be adjusted more freely to improve machine efficiency.

Numerous strategies are found in literature, which aim at maximising the efficiency of PM machine drives, both in motor and generator mode. These can be categorised into two main approaches, which include the use of a "search algorithm" [3]. The "search algorithm" changes the machine operating variable (in this case i_d) and observes the impact on the output, namely the active power and thus finding the ideal operating point. In [3] the "search algorithm" has been implemented for a Surface Mounted PM machine operating in motor-mode aiming at minimising the input power to the drive. Applying the same principle to a machine operating as a generator means that the maximum output power will be tracked instead. The advantage of such a strategy is that it works on machines without the knowledge of its exact parameters. One drawback however is that the search algorithm can introduce oscillations into the system which may require additional control to stabilise [4].

The second approach is based on exact knowledge of the equivalent circuit and its parameters. The governing equations of the machine can then be used to determine the ideal operating conditions that result in minimum losses. Much work has been

carried out on this type of loss minimisation and an overview of relevant work for this project is given here.

In [5] and [6] the author presents three control strategies which aim at minimising different losses in the machine. By setting the d-axis current reference to zero the copper losses are minimised. This represents the most common control technique for a PM machine. The second approach aims to maintain a maximum power factor, which results in minimum stator voltage, therefore minimising the core losses in the machine. Finally, the author proposes a loss minimisation algorithm (LMA) which aims at minimising the overall losses in the machine. This is achieved by defining the controllable losses, namely copper and core losses, as a function of the d-axis current component, and minimising this expression. Since in a surface mounted machine only the quadrature current component affects the torque produced, which is dictated by the MPPT algorithm to operate at the desired speed, the d-axis current component is derived as a function of quadrature current component and operating speed to minimise the overall losses. In a variable speed wind turbine the relationship between the machine's torque and hence qudrature current and the machine speed is dictated by characteristics of the turbine. The direct current component can therefore be computed as a function of speed or qudrature current. The author compares the traditional maximum torque strategy (id=0) with the proposed maximum efficiency control experimentally for a 3kW WECS at two different wind sites. It was found that an efficiency improvement of between 0.9% and 1.4% respectively was achieved, when using the LMA, compared to the maximum torque strategy.

Similar work is presented in [7], [8] and [9], where the author applies similar arguments to an IPMSG. Based on an equivalent circuit of the IPMSG and the known characteristics of the turbine, the author derives reference values for the d- and q-axis current components as a function of generator speed. No comparison to the traditional approach of zero direct current is given in [8], but the combination of MPPT and efficiency maximisation is proven successful based on accurate models of the machine and turbine. In [7], the author argues that the due to the considerable increase in iron losses at high speed, the loss minimisation control yields a higher efficiency improvement at higher speeds, which is confirmed by the results presented.

The impact of maximum efficiency control on a Surface-Mounted PM Machine is investigated through simulation in [4]. The controllable losses in the machine under consideration are copper and iron losses. Assuming the torque and speed of the machine being dictated by the MPPT algorithm, these losses can be minimised according to the same principles. In simulating and comparing this approach with the traditional maximum torque per current control ($i_d = 0$), the author determines an efficiency improvement of up to 5% at rated speed and torque and close to 10% at rated speed and 140% of its rated torque. This shows that the LMA becomes more effective at higher speeds and loading as was found in the literature discussed in this chapter.

1.3. Research Questions

The research presented in this thesis focuses on the full understanding and implementation, both in simulations and experimentally of a Permanent Magnet Synchronous Generator (PMSG) Wind Turbine System. Special attention is given to the different control strategies used to operate the system at its highest efficiency.

To achieve this, several research questions have been formulated:

- How can a wind turbine be emulated in the laboratory?
- Which system topologies are available for the development of a PMSG WECS?
- How can the PMSG be controlled?
- What options are available to connect the WECS to the grid?
- How can the losses in the machine be estimated and minimised?
- Which control strategies can be utilised to maximise the energy production of the system?

1.4. Objectives

The objectives of the work carried out are to:

- Implement a wind turbine emulator in the laboratory for the research project.

- Develop and implement the control of the PMSG in simulations and experimentally.
- Investigate and identify the appropriate control for the power electronic converter, which provides the grid connection.
- Implement the WECS experimentally in the laboratory by combining the individual components.
- Validate the operation of the WECS through simulations and experimentally.
- Compare and assess the control strategies and compare their effects on the operation of the WECS

1.5. Scope and Limitations

The simulation and experimental work was limited to a 6kW PM wind turbine system that was available for this project. The operating range of the system was limited to 2.5kW due to the restrictions of the hardware available. This translates into a maximum wind speed of about 7m/s which was below the rated speed of 12m/s for the turbine used. Furthermore the absence of a torque transducer in the experimental setup presented a significant challenge to predict the performance of the PM generator accurately.

1.6. Structure

An overview of the most commonly used WECS system topologies and the various components available to construct such a system is presented in chapter 2. In chapter 3, a more specific analysis of the PMSG system and its development is presented together with the control strategies used to maximise its output. An analysis based on the governing equations has is discussed in chapter 4. The simulated system is developed and implemented in chapter 5. Chapter 6 discusses the implementation of the system in the laboratory. The analysis of the results and comparisons between established and expected outcomes are presented in chapter 7. Conclusions and findings are finally presented in chapter 8.

Chapter 2

The Theory and Basic Principles of a WECS

2.1. Overview

The fundamental principles which determine the amount of energy absorbed by a Wind Energy Conversion System (WECS) are presented in this chapter. Furthermore, the dominant system topologies are discussed briefly. A more detailed discussion of the Permanent Magnet Synchronous Generator Wind System is provided together with the different control strategies available for this system. Finally, the theory and control associated with the transfer of power to the grid is presented along with the design of an appropriate grid-filter to minimise current distortions.

2.2. Wind Power

The power obtained from the wind is dependent on several factors, which include: the wind speed, the shaft speed and the turbine characteristics.

The amount of power extracted from the incident wind varies with wind and turbine speed. The power coefficient (C_p) of the turbine describes the ratio of the captured turbine power to the absolute power available from the incident wind. The power coefficient is a function of the Tip Speed Ratio (TSR), which is the ratio of the blade tip speed to the wind speed [10] [11].

The theoretical maximum of the value of $C_p(\lambda)$ is 0.593, which is based on Betz's Law [12]. The value of C_p is a function of wind speed, turbine speed and pitch angle.

For a fixed-blade turbine as used in many small wind power applications, the pitch angle is constant and assumed not to affect C_p. The TSR is calculated according to equation (2.1).

$$\lambda = \frac{\omega \cdot R}{v} \tag{2.1}$$

where ω is the shaft speed, R the radius of the turbine blades and v the wind speed.

The power captured by the turbine is given as:

$$P_{turbine} = {}^{1}/_{2}\,\rho A v^3 C_p \tag{2.2}$$

where A is the area swept by the turbine's blades and ρ is the density of air [13],[14].

The torque developed by the turbine is calculated as a function of wind speed and turbine speed according to equation (2.3).

$$T_{turbine} = \frac{P_{turbine}}{\omega} \tag{2.3}$$

From these formulae, it emerges that for each wind speed there is exactly one turbine speed at which maximum power can be extracted from the incident wind if the blades are fixed. In order to maximize the energy captured of the wind turbine, the system is required to track this maximum power point (MPP) as closely as possible, whilst accounting for other limitations such as rated values and safety limits of the machine and turbine.

2.3. Maximum Power Point Tracking

When dealing with variable-speed wind turbines, the operating speed should be adjusted with wind speed to ensure that maximum power is extracted by the turbine and delivered to the generator. One important differentiation can be made between

systems which employ wind speed sensors and sensor less control approaches. If a wind sensor is available the ideal operating speed of the turbine can be calculated according to the turbine's properties. This type of Maximum Power Point Tracking (MPPT) requires detailed knowledge of the turbine and it's Power vs. Operating Speed curves at different wind speeds and pitch angles. This project deals with a fixed-pitch wind turbine, therefore each wind speed has only one curve relating the power coefficient to the operating speed. The relationship between wind speed, turbine speed and power coefficient is defined through the tip-speed-ratio of the turbine (TSR) [5],[9]. The TSR is defined as the ratio of blade tip-speed to the wind velocity and can be expressed as:

$$\lambda = \frac{\omega \cdot R}{v_{wind}} \tag{2.4}$$

And the power coefficient (C_P) is then given as a function of the TSR (λ).

$$C_p = f(\lambda) \tag{2.5}$$

The relationship between C_P and λ which was used in this project is shown in figure 2.1.

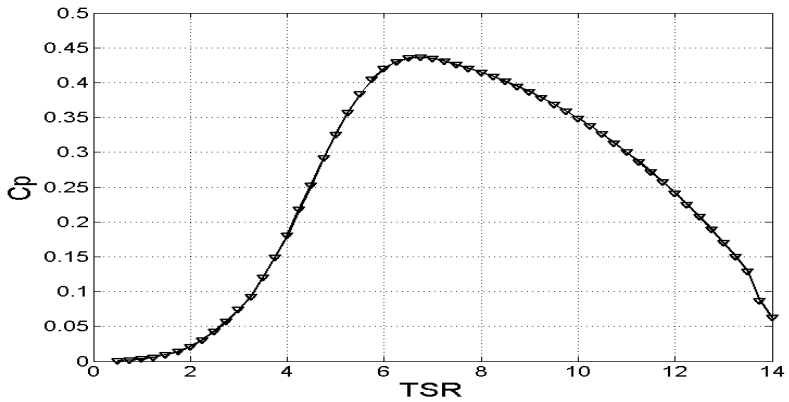

Figure 2.1: Power Coefficient vs. TSR

The ideal rotor speed at which the maximum power is extracted from the incident wind can then be calculated according to the following equation:

$$\omega_{Ref,MPPT} = \frac{\lambda_{opt} \cdot v_{win\ d}}{R} \tag{2.6}$$

This provides the speed reference for the machine, which will ensure that the maximum power is extracted from the wind.

2.4. Other factors impacting the power obtained from the wind

In addition to the basic aerodynamic laws which govern the power captured from the wind, there are other issues which affect the extraction of this power. These are described conceptually in this section and include: tower shadowing, furling, etc.

2.4.1. Tower shadowing

Any horizontal-axis turbine has to be mounted onto a structure, usually a tower, which inevitably has an impact on the wind flow experienced by the turbine. The tower or any other obstruction to the wind will cause the wind speed to decrease in front of such a structure as shown in figure 2.2. Every time a turbine blade passes in front of the tower it experiences a reduced wind speed which results in an overall reduced torque exerted on the shaft of the turbine. This tower shadowing effect results in a ripple in the torque and power of the turbine. This ripple occurs at a frequency determined by the product of the turbine speed and the number of blades. The amplitude of the torque ripple depends on the physical dimensions of the tower as well as the blades [13].

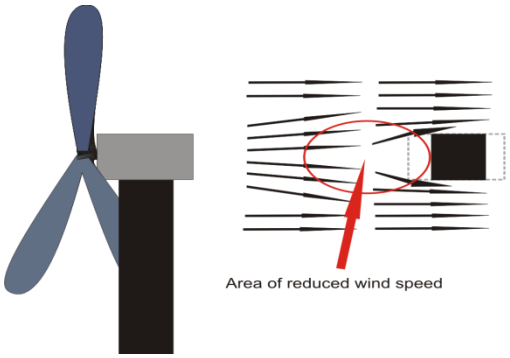

Figure 2.2: Impact of Tower Shadowing on the wind flow

Averaging the torque ripple over one turbine results in equation (2.7) for the turbine torque:

$$T_{turbine} = \frac{{}^{1}/_{2}\rho A v^{3} C_{p}}{\omega} - T_{tower} \qquad (2.7)$$

The torque ripple due to the tower shadowing effect can be incorporated in any simulated and emulated behaviour of a turbine.

2.4.2. Furling

Furling can be used to limit the power absorbed from the wind at high wind speeds in order to protect the turbine and generator from damage. The turbine is turned around either its vertical or horizontal axis in order to decrease the angle of attack from the wind.

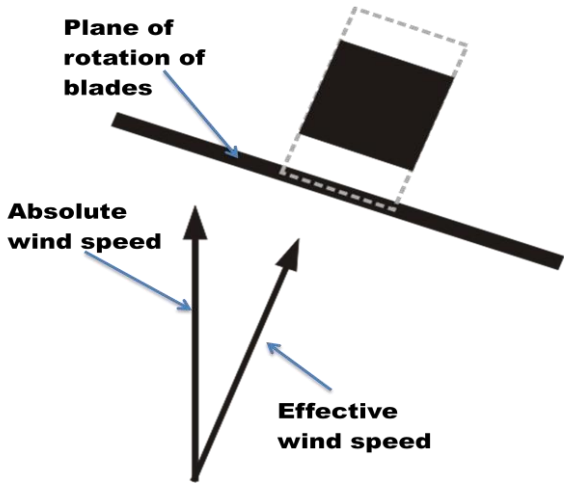

Figure 2.3: Impact of Furling on the effective wind speed experienced by the wind turbine

To account for this effect, only the component of the wind speed perpendicular to the plane of rotation of the blades is considered. Measuring the angle as θ and substituting it into equation (2.2) yields a new, more complete formula for the wind power extracted. This is expressed as equation (2.8).

$$P_{turbine} = {}^{1}/_{2}\,\rho A(v\cos\theta)^{3}C_{p} \tag{2.8}$$

Consequentially, the torque from the wind turbine becomes:

$$T_{turbine} = \frac{P_{turbine}}{\omega} = \frac{{}^{1}/_{2}\rho A(v\cos\theta)^{3}C_{p}}{\omega} \tag{2.9}$$

The effects of tower shadowing and furling can be combined to write an expression of the net turbine torque. This can be expressed as in equation (2.10).

$$T_{turbine} = \frac{1/2\rho A(v\cos\theta)^3 C_p}{\omega} - T_{tower} \quad (2.10)$$

2.4.3. Turbine and Generator Inertia

All mechanical parts of the wind turbine drive train have inertia which will limit the acceleration during transient changes in wind speed.
The change in turbine speed will be limited according to the following equation (2.11).

$$\dot{\omega}_{turbine} = \frac{T_{turbine} - T_{generator}}{J_{turbine} + J_{generator}} \quad (2.11)$$

This formula assumes that the wind turbine and the generator are coupled directly without a gearbox. Furthermore, friction in the bearings of the machine and turbine will reduce the effective torque further and can be included in the equation above. Incorporating all the factors discussed in this section will result in a more accurate model of the aerodynamics of a wind turbine. This becomes especially important when analysing the transient behaviour of the system. Since the main focus of the work presented in this thesis was on the steady-state behaviour the system, the inertia of the drive train was not considered.

2.5. Emulating the behaviour of a wind turbine

The behaviour of a wind turbine can be implemented in simulation with relative ease. However, to test the proposed system experimentally in a laboratory, a wind turbine emulator is required. An emulator provides a better way of testing a wind generator system under controlled but realistic conditions in a laboratory [15]. An overview of the different options available to implement such a system is discussed in this section. The governing equations which determine the behaviour of a wind turbine were presented in section 2.2. These equations provide the basis for the work discussed here.

An approach to emulate a wind turbine by means of a DC motor driven by a commercial DC drive is presented in [15]. The system measures the rotational speed of the turbine by means of a dSPACE control board and then calculates the applicable torque based on the governing equations of the turbine and depends on

the wind speed and blade pitch angle. This reference torque is converted into the applicable reference voltage of the DC drive. Since the DC drive is operated in torque control mode the reference voltage will result in the same torque regardless of the speed it is operating at [15]. The emulator developed is able to emulate a turbine with fixed or variable-pitch blades. In addition, it allows for the implementation of effects such as tower shadowing and furling, which are a mere reduction in torque applied and therefore simple to implement.

A similar approach is presented by Battaiotto in [16]. Similar to [15], the author uses a DC motor which is supplied from an AC/DC converter with current feedback in order to operate in torque control mode. The current reference is supplied by a dual-DSP microprocessor system that calculates the applicable torque based on operating speed, wind velocity and the turbine characteristics. To experimentally confirm the systems viability it was programmed with the characteristics of a fixed-pitch, variable-speed wind turbine and used to drive a grid-connected six-pole induction generator. The system was then fed with a wind profile consisting of numerous step-changes. Both systems presented in the afore-mentioned literature exhibit the expected behaviour as shown in the experimental results.

Neammanee [17] argues, in his work on a wind turbine simulator, for the use of a squirrel-cage induction motor rather than a DC motor. This is due to a number of factors, which include the relatively large-sized DC motor required to meet the torque requirements and the high cost and maintenance requirements associated with this. The proposed system uses a 4kW induction motor which is fed from an inverter and operated in torque control mode. The reference torque signal is generated based on the turbine characteristics in a digital signal control board. In addition to the tower effect which produces a torque ripple, the author also emulates the rotor inertia in his system which limits the rate of acceleration by means of reducing the effective torque acting on the generator [17]. The results presented show a comparison of the calculated power with the actual measured power in the wind turbine as a function of wind speed and turbine speed under varying wind conditions. These results show a close correlation between the calculated and experimental results.

2.6. WECS Topologies

Several WECS topologies are currently used for various applications. These topologies can be classified, depending on whether it is a fixed- or variable-speed system and also the type of generator used. The most common generators are the squirrel-cage induction generator, doubly-fed induction generators, synchronous generators and PMSGs. The various WECS configurations are briefly discussed here.

Fixed-speed WECSs have been popular in the past due to their simple design and low-maintenance. These systems generally have an induction generator, and are directly connected to the grid. This results in almost constant speed operation, limited to the operating slip range of the generator. Induction generators are mechanically simple and have relatively high efficiency, whilst requiring low maintenance. This makes the induction generator popular in fixed-speed WECS applications. The relatively low power factor which is a result of the machines inherent reactive power consumption is a major drawback [18].

A fixed-speed WECS is usually designed to be most efficient at a particular wind speed. This can be overcome by using a generator with 2 sets of windings and a turbine with variable-pitch blades. This will result in more efficient operation at a range of wind speeds. A typical fixed-speed WECS setup with an induction generator is shown in figure 2.4.

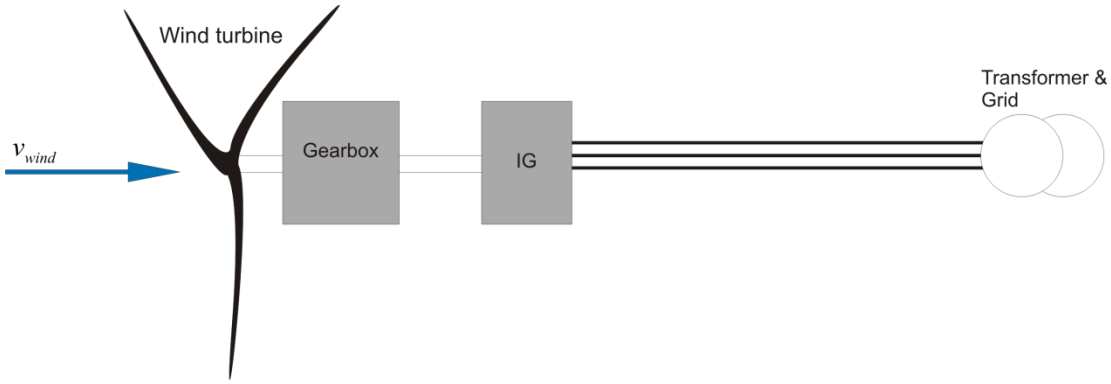

Figure 2.4: Fixed Speed Grid-tied IG WECS

Variable-speed WECS on the other hand have become the preferred topology in recent times. This is largely due to technological advances in power converter technology which decouple the generator from the grid [18]. The ability to change the

rotational speed as desired allows the system to operate at high aerodynamic efficiency as described in section 2.2.

Doubly-fed induction generators (DFIGs) play a major role in variable-speed WECS. Their stators are usually connected directly to the grid while their rotors are excited through power electronic converters, usually a back-to-back AC-AC converter as shown in figure 2.5. This allows for operation over a wide speed range as well as independent control of active and reactive power which renders the DFIG a highly controllable WECS configuration.

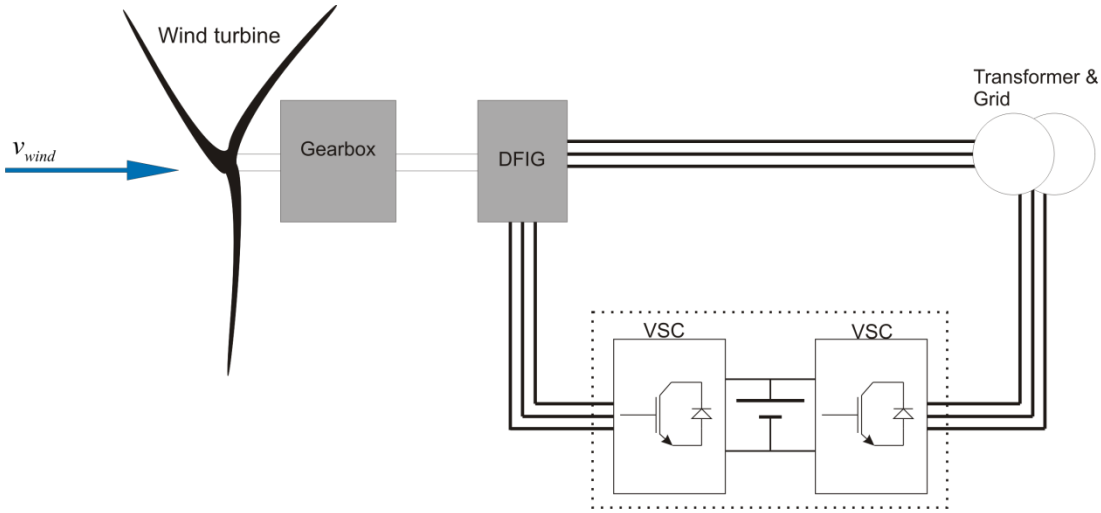

Figure 2.5: Variable-Speed Grid-tied Doubly-Fed IG WECS

In addition to the DFIG, a variable-speed WECS can be based around a squirrel-cage induction generator or synchronous generator. The synchronous generator can either be a wound rotor type (WRSG), also known as a separately excited synchronous generator or a permanent magnet synchronous generator (PMSG). In order to achieve variable speed operation, these generators have to be connected through a back-to-back power converter as shown in figure 2.6.

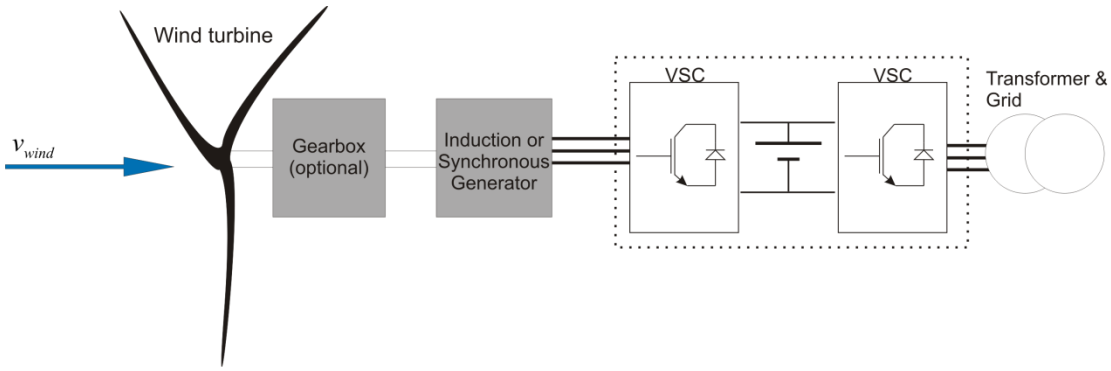

Figure 2.6: Variable-Speed IG WECS with back-to-back grid converter

In order to limit the power at winds above rated speed, a WECS can either make use of stall-control, pitch-control or furling. Larger systems usually have pitch-controlled blades, while smaller systems either make use of blades designed to stall at high wind speeds or furling. Furling and stalling are cheaper to implement, which makes them more popular in smaller systems.

Variable speed WECSs based on PMSGs are discussed in the next section as this forms the basis for the system developed in this project.

2.7. PMSG Wind Energy System Topologies

The focus of this project is on the use of a PMSG in a variable speed WECS. There are several power converter topologies which can be used with the PMSG. The most prominent ones are presented here, although there are several uncommon topologies which are not discussed.

WECSs which make use of PMSGs can either used in be stand-alone systems or grid-connected applications.

Stand-alone systems typically need an energy storage element due to the erratic nature of wind which determines the available energy. The storage element can be a battery or any other form of energy storage. Figure 2.7 shows a typical stand-alone WECS. A diode-bridge rectifier is used to convert the AC output of the machine into DC.

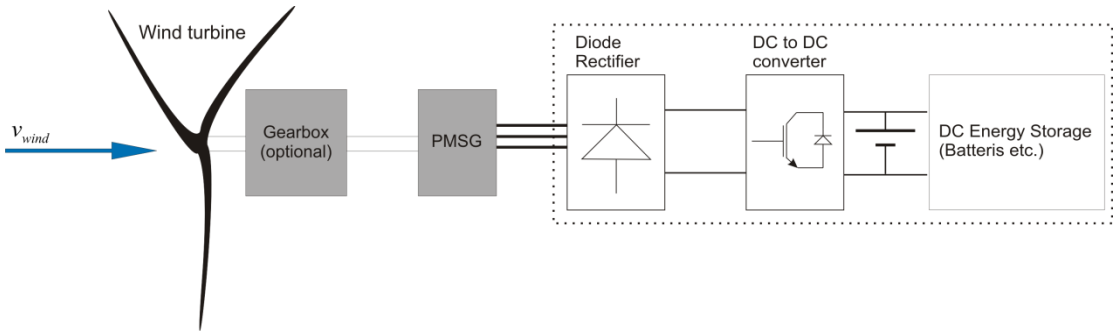

Figure 2.7: Stand-alone PMSG with Diode Rectifier and DC/DC converter

A diode-bridge rectifier only allows for the control of the machine's active power flow. This is achieved by means of controlling the rectifier current through a DC/DC converter. This topology is applicable for small systems where the additional cost of a back-to-back converter is not justifiable. The DC-DC converter can be a boost, buck or buck-boost type and is ultimately responsible for controlling the PMSG's speed. An alternative to storing the produced energy is a grid-tied converter as shown in figure 2.8.

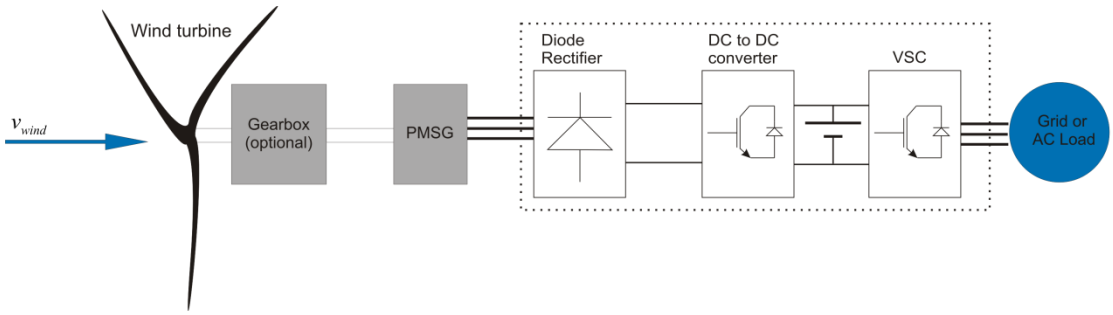

Figure 2.8: Grid-tied PMSG with Diode Rectifier and intermediate DC/DC converter

If more sophisticated control of the machine is required, a controllable converter needs to be used on the machine side. The back-to-back configuration is the most common topology for medium to large PMSG systems, which are primarily grid-connected. This is shown in figure 2.9. Here a full rated converter is required as compared to the $^1/_3$ rating in the DFIG systems.

This represents one of the main drawbacks of PMSGs for large WECSs. However the perceived drawback of the full converter is offset by the absence of a gearbox in large direct-drive PMSG WECSs. The maintenance requirements and unreliability of the gearbox is therefore eliminated in a direct-drive WECS.

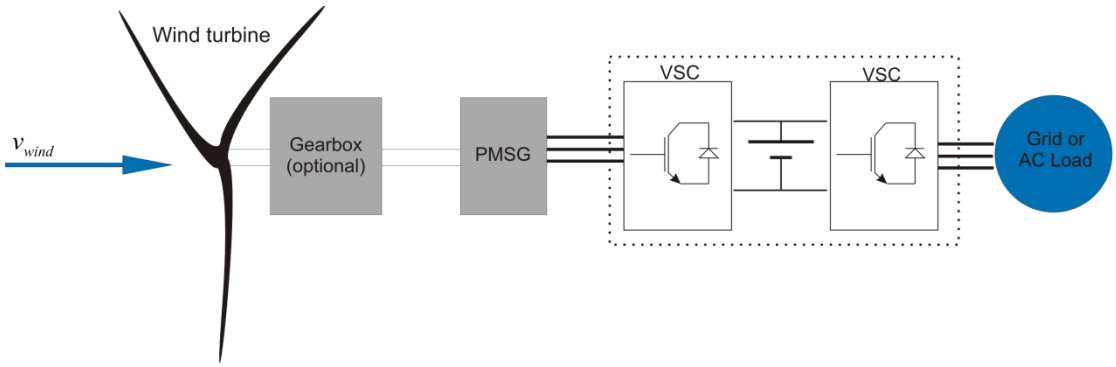

Figure 2.9: Grid-tied PMSG with full back-to-back VSC's

Depending on the generator used and the turbine characteristics the use of a gearbox can improve the systems performance. This depends on several factors, including maintenance, cost, performance, etc. However this is not required in modern direct-drive WECSs.

Another topology for stand-alone WECSs is shown in figure 2.10. Here a fully-flexed converter is used to convert the produced AC into DC and supply an energy storage element. This topology allows for full control of the machine. However, stand-alone WECSs which supply an energy storage element are usually too small. This topology is therefore not popular.

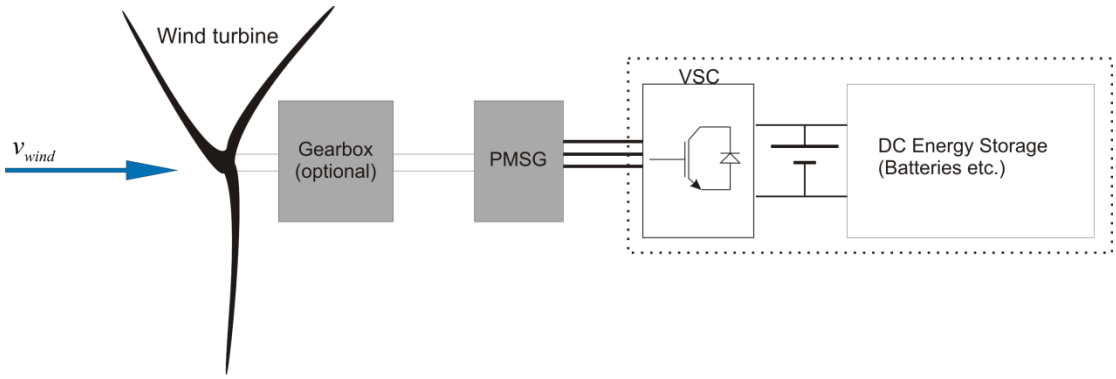

Figure 2.10: Stand-Alone PMSG with fully controlled Rectifier

Energy Storage can be realised in a wide variety of ways, ranging from simple battery banks to pump storage systems. These systems are not discussed here since the focus of the project is on grid-tied systems

A grid-tied system does not require such storage, since all available energy is transferred to the grid. A more detailed comparison between the converter topologies and their respective features is presented in the next section.

2.8. Converter Topologies

Power electronic converters are used to connect a wind turbine to the grid or a standalone network. Throughout literature, numerous topologies are found which depend on the system design and its application. The focus in this project is on grid-connected wind turbine systems with PMSGs, which operate at variable speeds.

WECSs operating at variable speeds require power electronic converters to connect the WECS to the grid or load. Three main categories of rectifier systems are found in literature, namely passive rectifiers, passive rectifiers in conjunction with a DC/DC converter and active controllable rectifiers.
Most systems feature an intermediate storage element in the DC link. This can be either a capacitor or an inductor depending on the type of system [19]. The DC-Link decouples the generator from the grid which is necessary when operating at variable speed and hence frequency. This is in contrast to systems which are directly connected to the grid, such as induction generators. These systems are usually operated at fixed speed or a narrow speed range due to the fixed frequency of the grid [20].

2.8.1. Passive/Diode Rectifier

The use of diode rectifiers has been discussed and investigated by various authors throughout literature. In [21], Tan connects a PMSG to the grid by means of an uncontrolled diode rectifier which feeds into a current-controlled inverter. A current-controlled inverter allows for a wide range of DC-voltages which is necessary in order to operate the machine at variable speed. It must be noted that in this topology the inverter controls the power drawn from the generator which can result in slow responses depending on the time constant of the control system as well as the DC-Link storage element. [19]

In [22] a diode rectifier is used in conjunction with a boost DC/DC converter to supply the required voltage for a grid-connected inverter. This topology allows for two separate control loops, the DC/DC converter controls the generator power while the inverter control loop maintains the desired DC-voltage while transferring the excess power to the grid.

It should be noted that a passive rectifier does not allow for the control of reactive power drawn from the generator, thus making this system configuration unsuitable for optimising the generator efficiency.

2.8.2. Active Rectifier

Using an active or controllable rectifier results in certain advantages compared to the passive alternative.

In [23], Zhang describes a system which uses two back-to-back PWM converters. The generator side converter controls the generator under the desired conditions while the grid side inverter maintains the DC-Link voltage and transfers the power to the grid. The afore-mentioned generator side converter operates as an active rectifier, which can control the active and reactive power drawn from the generator independently. This can be achieved by manipulating the direct and quadrature current components of the generator as discussed in section 2.8.

In [5], Chinchilla proposes the use of Space-Vector-Modulation to control both converters. Using active power converters allows her to impose various different control strategies on the generator which can lead to improved efficiencies. This is discussed in more detail in chapter 3.7.

Morimoto discusses a similar approach in [8] and [7]. He also uses vector controlled converters to control the generator. Although he does not describe the actual converter topology it is implied that an active rectifier is utilised in order to achieve full vector control of the generator currents.

2.9. Controlling a Permanent Magnet Synchronous Generator

The basic control principles of a PMSG are discussed in this section. Furthermore, the different control strategies used to implement variable speed operation of a PMSG are discussed, together with their effect on generator performance. Since this project focuses on fixed-pitch wind turbines, the control of variable-pitch turbines is omitted and attention is given to control by means of active back-to-back power converters.

To achieve better control of the generator is modelled in the dq-reference frame according to the following equations:

$$v_d = -R_s i_d - L_s \frac{di_d}{dt} + L_s \omega_e i_q \tag{2.12}$$

$$v_q = -R_s i_q - L_s \frac{di_q}{dt} - L_s \omega_e i_d + \omega_e \lambda_{pm} \tag{2.13}$$

$$T_{em} = {}^3/_2\, p \cdot \left(\lambda_{pm}\, i_q - \left(L_d - L_q\right) i_d\, i_q\right) \tag{2.14}$$

$$P = {}^3/_2 \left(v_d i_d + v_q i_q\right) \tag{2.15}$$

$$Q = {}^3/_2 \left(v_q i_d - v_d i_q\right) \tag{2.16}$$

$$\lambda_s = \sqrt{\lambda_q^2 + \lambda_d^2} = \sqrt{\left(\lambda_{pm} - L_s i_d\right)^2 + \left(-L_s i_q\right)^2} \tag{2.17}$$

The cross-coupling effect between the d- and q-axis is evident from equations (2.12) and (2.13). In order to control the direct and quadrature current components independently the control has to compensate for the voltage components induced by currents in the other axis as well as the permanent magnet flux linkage component in the quadrature axis. The components added to the d- and q-axis control implementations respectively, are:

$$\Delta v_{d,decoupling} = -L_s \omega_e i_q \tag{2.18}$$

$$\Delta v_{q,decoupling} = -L_s \omega_e i_d + \omega_e \lambda_{pm} \tag{2.19}$$

The speed of the machine is controlled by adjusting the torque producing component of the stator current (ie. quadrature current) and thereby the developed torque which in turn results in an acceleration or deceleration of the machine. The implementation of this control is presented in chapter 3 while an analytical study is carried out in chapter 4. The simulated and experimental results are presented in chapter 5 and 6 respectively.

2.9.1. Maximum Torque per Current Control (id=0) of a PMSG

The most popular approach to controlling a PMSG is to maximise the torque output per ampere of current applied. This approach found in literature ensures that minimum stator current is drawn in order to develop the required torque. When dealing with a surface mounted machine the torque equation is simplified due to the absence of saliency in its magnetic circuit. The generalised expression for torque, presented in equation (2.14) reduces to equation (2.20) since $L_d = L_q$.

$$T_{em} = \frac{3}{2} \cdot p \cdot \lambda_{pm} i_q \tag{2.20}$$

As evident in equation (2.20), the direct current component has no impact on the developed torque and is therefore set to 0 in order to minimise the total stator current in the machine. This in turn minimises the resistive losses which are a function of the total stator current, governed by the relationship in equation (2.21).

$$W_{cu} = 3 \cdot R_s \cdot (i_d^2 + i_q^2) \tag{2.21}$$

Reducing the direct current component to zero clearly minimises this expression and hence the copper losses. However, this does not minimise other losses in the machine, such as core and stray losses.

2.9.2. Unity Power Factor Control

Maximising the power factor at which the machine is operating minimises the incurred core losses in the machine and minimises the overall stator voltage. It must be noted that minimising the core losses by maximising the power factor does not take other losses into account and can in fact result in increased overall losses. The additional non-zero d-axis current component will increase the total stator current and may thereby increase the total losses, depending on the machine parameters.

To achieve unity power factor for the machine the phase angle of the stator current should equal the phase angle of the stator voltages [24]. The voltage and current phase angles in the machine are defined as equations (2.22) and (2.23) respectively.

$$\theta_v = \tan^{-1}\frac{v_q}{v_d} \tag{2.22}$$

$$\theta_i = \tan^{-1}\frac{i_q}{i_d} \tag{2.23}$$

In order for the two phase angles two be equal, it is necessary that:

$$\frac{i_{qs}}{i_{ds}} = \frac{v_{qs}}{v_{ds}} \tag{2.24}$$

Hence the reference value for the d-axis (magnetising current) component is given by equation (2.25).

$$i_d = i_q\frac{v_d}{v_q} \tag{2.25}$$

Another approach to obtain the direct current component which results in unity power factor is based on the reactive power in the machine. By reducing the reactive power to zero, the power factor will become maximised. In a PMSG the reactive power is calculated according to equation (2.16).

To attain unity power factor the reactive power must be zero, therefore:

$$0 = \frac{3}{2}\cdot\left(v_d i_d - v_q i_q\right) \tag{2.26}$$

$$v_d i_d = v_q i_q \tag{2.27}$$

Substituting the governing machine equations (2.12) and (2.13) into equation (2.27) results in the expression in equation (2.28).

$$i_d i_q r_s - \omega L_q i_q^2 = i_d i_q r_s + \omega \lambda_{pm} i_d + \omega L_q i_q^2 \tag{2.28}$$

And hence:

$$-2\omega L_q i_q^2 = \omega \lambda_{pm} i_d \tag{2.29}$$

Solving equation (2.29) for i_d results in the expression shown in equation (2.30).

$$i_d = \frac{-2L_q i_q^2}{\lambda_{pm}} \tag{2.30}$$

Equation (2.30) can be used to produce the reference d-axis current (i_d) as a function of machine parameters and q-axis current reference (i_q). This forms the basis of the Unity Power Factor control strategy applied in this project.

2.9.3. Maximum Efficiency Control

In order to maximize the overall system efficiency, the power extracted from the wind turbine and the generator must be maximised simultaneously. This is required since the generator efficiency varies with loading and speed. Furthermore the total losses in the machine should be considered to maximise its output electrical power. This type of control is only possible with a fully controllable generator side converter, which can impose the desired direct and quadrature current components on the machine. Prior research presented in the literature provides meaningful discussions on how the system's overall efficiency can be improved through sophisticated control of the machine side converter. Furthermore, there are different approaches and conclusions on how best to address this problem.

All approaches discussed in the literature fit into one of the two following categories: They are either based on a search algorithm or a Loss Minimisation Algorithm (LMA) derived from a loss model.

In a surface-mounted PM machine the electromagnetic torque is governed by equation (2.20), and only depends on the q-axis current component. This allows for the d-axis current component to be adjusted in a manner that will improve generator efficiency, although there are limiting factors such as the maximum permissible stator current.

The traditional approach has been to minimise resistive losses in the machine by minimising the stator current. This is achieved by setting the d-axis current component of the stator current to 0 ($i_d = 0$) [5], as discussed in the section on maximum torque per current control. Resistive losses in a PM machine only occur in the stator windings of the machine due to the absence of rotor windings. The copper losses can be calculated according to equation (2.21). This clearly illustrates how a zero d-axis current component will result in minimum resistive losses. Usually this technique is suitable for high torque and low speed operation since the total stator current consists of only the torque-producing q-axis current component [5]. Minimising the resistive losses in the generator does not take into account the core losses or mechanical losses. Mechanical losses are a function of generator speed and friction and windage in the system which are uncontrollable [7],[5]. However, core losses are a function of frequency and the magnetic flux present in the machine, which in turn depends on the stator voltage. By setting the d-axis current component such that the generator operates at unity power factor, the stator voltage is minimised and so are the core losses [5]. In Chinchillas work [5], she expresses the core losses as a function of speed as well as stator current according to equation (2.31).

$$P_{Fe} = K_c(\Omega)\left[\left(\lambda_{pm} - L_s i_d\right)^2 + \left(-L_s i_q\right)^2\right] \tag{2.31}$$

From here she concludes that minimum core loses are obtained by minimising this equation. Since the q-axis current component is dictated by the required torque, the equation is minimised for the following condition:

$$\lambda_{pm} - L_s i_d = 0 \tag{2.32}$$

Hence:

$$i_d = \frac{\lambda_{pm}}{L_s} \tag{2.33}$$

Chinchilla argues that minimising the core losses can result in very high stator currents under high loading and speed, which increases copper losses and possibly exceeds the rated current of the machine. She therefore suggests minimising the sum of both losses as long as current ratings are not exceeded [5]. This is explored in the third control strategy discussed in her work. To achieve this, the author differentiates the sum of all controllable losses as a function of the direct current component, as follows:

$$\frac{d}{di_d}(P_{cu} + P_{core}) = 0 \tag{2.34}$$

$$\frac{d}{di_d}\left(3 \cdot R_s \cdot \left(i_d^2 + i_q^2\right) + K_c(\Omega)\left[\left(\lambda_{pm} - L_s i_d\right)^2 + \left(-L_s i_q\right)^2\right]\right) = 0 \tag{2.35}$$

Solving equation (2.35) for i_d results in the following expression:

$$i_d^* = \frac{P_{Fe,0}(\Omega) L_s \lambda_{pm}}{3R_s {\lambda_{pm}}^2 + P_{Fe,0}(\Omega) L_s^2} \tag{2.36}$$

According to [5] the d-axis current component must be limited to:

$$i_{d\ lim} = \xi_{lim}\ \frac{\lambda_{pm}}{L_s p} \tag{2.37}$$

,where ξ_{lim} is the demagnetising coefficient which depends on the magnet properties and the machine design and p is the pole number. This limit is imposed to prevent permanent demagnetisation of the PMs.

However, Chinchilla states that the rated current will always be lower than this limit which means the actual d-axis current limit is given as:

$$i_{d,lim} = \sqrt{i_{s,rated}^2 - i_q^2} \tag{2.38}$$

In her work, Chinchilla compares the maximum efficiency direct current control with the traditional maximum torque per current control method at two different wind conditions. Under both wind conditions (average wind speeds of 7.5 and 6m/s) the maximum efficiency control proves to be more efficient than the maximum torque per current control. The efficiency improvement is higher at lower wind speeds. For an

average wind speed of 6m/s, Chinchilla found the improvement to be 1.4% compared to approximately 0.9% at the higher wind speed [5].

In [8] it was found that variable speed wind generator systems have to employ different control strategies under varying operating conditions. When the system is operating below rated conditions, maximum power needs to be extracted and the generator should be operated at maximum efficiency.

In [4] a dynamic dq-model of the PMSG is developed in order to estimate the losses at various operating conditions. The model developed is shown in figure 2.11 below.

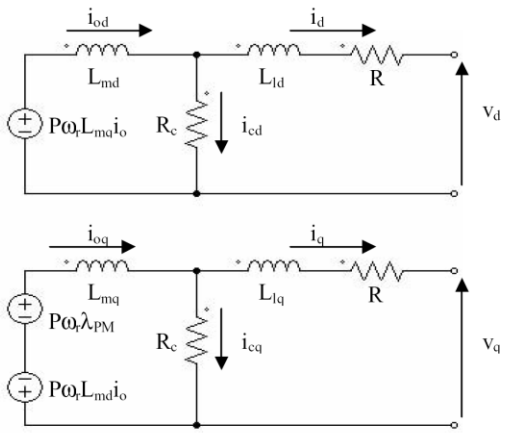

Figure 2.11: d-q axis equivalent circuits of the PMSG [4]

In [4], Di Tommaso develops an expression for the copper and iron losses due to the fundamental components of the stator currents as a function of the operating speed and the d- and q-axis components of the stator current. This can be expressed as:

$$W_c(i_{od}, i_{oq}, \omega) = W_{Cu} + W_{Fe} \tag{2.39}$$

Differentiating this equation with respect to the d-axis current component allows the ideal value for i_{od} to be determined, which results in minimum losses for fixed values of the other two variables (i_{oq}, ω) which are dictated by the MPPT algorithm. The author simulates the machine losses at various loading conditions and compares the resulting losses using this Loss Minimisation Algorithm (LMA) [4] to the traditional approach of maximum torque per current, which only minimise resistive losses. Di Tommaso's simulations show an efficiency improvement of up to 10% at low speed and high torque (138.9% loading), and an improvement of approximately 3% at rated conditions [4].

A similar approach to Output Maximization is presented by Morimoto in [9]. Using the equivalent circuits, shown in figure 2.12, he derives formulae for the core and copper losses in the machine. This is expressed as:

$$W_{loss} = W_{Cu} + W_{core} = R_S\left(i_d^2 + i_q^2\right) + \frac{\omega^2\left\{\left(L_d i_{od} + \lambda_{pm}\right)^2 + \left(L_q i_{oq}\right)^2\right\}}{R_C} \qquad (2.40)$$

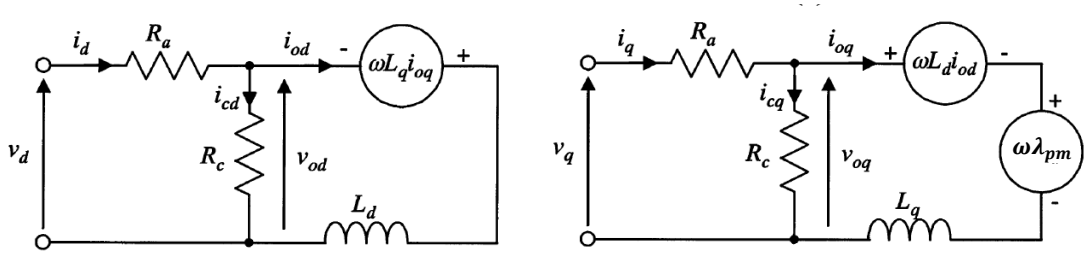

Figure 2.12: d-q equivalent circuit [9]

Furthermore, Morimoto suggests different control strategies depending on the operating conditions. At operating speeds below the base speed, MPPT is applied together with the LMA, which results in the highest possible efficiency. Due to the complexity of the calculations involved in obtaining the ideal reference values for the direct and quadrature current components as a function of torque and generator speed, the author suggests a way of calculating the current components as a third-order polynomial, as a function of speed only. To achieve this he uses the fact that the MPPT conditioning relates each operating speed to exactly one torque value which enables the cancellation of the torque variable from the current reference calculations [9]. This results in the maximum aerodynamic power being obtained from the turbine while the generator losses are minimised.

Morimoto proposes a change in control strategy once the base speed is reached and voltage and current values reach their maximum. To remain within the applicable voltage and current boundaries at speeds above base speed the quadrature current component is reduced while the direct current component increases further according to the formulae shown below [9]:

$$i_d = \frac{\lambda_{pm} L_d - \sqrt{\left(\lambda_{pm} L_d\right)^2 + \left(L_q^2 - L_d^2\right)\left(\left(L_d I_{am}\right)^2 - \left(\frac{V_{om}}{\omega}\right)^2\right)}}{L_q^2 - L_d^2} \qquad (2.41)$$

$$i_q = -\sqrt{I_{am}^2 - i_d^2} \qquad (2.42)$$

where I_{am} and V_{om} are the maximum values of the armature current and induced voltage.

Morimoto proposes a system in which the current references are solely a function of generator speed. These values are calculated in advance and then recorded which means only the speed needs to be measured to obtain the applicable reference values. The author verifies the developed theory through experiments. He uses an AC servomotor to emulate the wind turbine in the laboratory instead of an actual wind turbine [9]. Using the calculated reference currents for the direct and quadrature current components and imposing them onto the generator depending on the operating speeds, the system achieves an overall efficiency of close to 80% at medium to high operating speeds. The generator efficiency exceeds 80% at lower speeds around 40% of rated speed (1800rpm) [9]. Morimoto does not offer any comparison to a system operating the generator at maximum torque per current control (i.e. $i_d = 0$) and he acknowledges that the low generator rating could impact negatively on the generator efficiency, as efficiency generally improves with power rating [9].

In [7] the author addresses the same issue of loss minimisation control in a slightly different approach. Using the equivalent circuits shown in figure 2.13, he derives the ideal values for direct and quadrature axis current components.

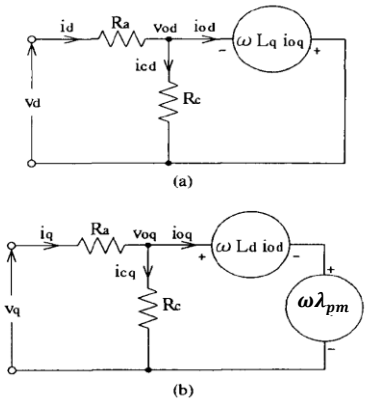

Figure 2.13: (a) d-axis and (b) q-axis equivalent circuit [7]

The author derives the ideal value for i_{od} as:

$$i_{od} = \frac{\omega^2 L_d (R_a + R_c)\lambda_{pm}}{R_a R_c^2 + \omega^2 L_d^2 (R_a + R_c)} \tag{2.43}$$

As the machine has no saliency, the developed torque is independent of the direct current component, which is used to minimise the generator losses, just as in [9] and [8]. The current components which can be controlled are i_d and i_q which are calculated according to:

$$i_{od} = i_d - i_{cd} \tag{2.44}$$

$$i_{oq} = i_q - i_{cq} \tag{2.45}$$

where

$$i_{cd} = -\frac{\omega\rho L_d i_{oq}}{R_c} \tag{2.46}$$

$$i_{cq} = \frac{(\lambda_{pm} + L_d i_{od})}{R_c} \tag{2.47}$$

Using the same principle as in [9] Morimoto suggest an approximation of the LMA in the form of a polynomial which relates the value of i_d to the q-axis current component (i_q) as follows:

$$i_d = K_0 + K_1 i_q + K_2 i_q^2 \tag{2.48}$$

The constants K_0, K_1 and K_2 depend on the operating speed and have to be calculated accordingly. Morimoto compares this LMA in simulation to the traditional approach of maximum torque per current ($i_d = 0$) at rated torque, while varying the speed. His results show a definite improvement in the efficiency of approximately 10%. He points out that this large increase in efficiency is mainly due to the increase in reluctance torque which results in lower armature current and hence reduced copper losses. The second reason for the improvement is due to the reduced flux-linkage, which results in a reduced armature voltage, thereby leading to a decrease in iron losses. In a non-salient machine the direct current component does not contribute to the torque produced and hence the efficiency improvements are expected to be lower [7].

Throughout the works discussed, one fundamental method to minimise generator losses can be extracted, which all authors address in their respective works, the fundamental principle of the LMA. Depending on the type of machine used, salient or

non-salient, the equations differ, but the principle remains the same. Expressing the controllable losses as a function of the controlled variable and minimising this expression as a function of the relevant operating conditions results in minimum losses. For a non-salient machine the only variable which can be changed is the d-axis current component (i_d). Therefore the basic principle of the LMA is to derive an expression for the controllable losses as a function of i_d and then minimising the expression. This forms the basis of the LMA derived for the PMSG in this thesis and is presented in chapter 3.3.3.
It also stands out that machines with saliency are likely to profit more from the LMA than their non-salient counterparts [7], [9].

2.10. Grid-Side Converter and Control Theory

The WECS considered for this project is connected to the grid by means of an inverter and a grid filter. An inverter is required to convert the DC-Link Voltage to the three-phase AC of the utility grid. There are different approaches to control the inverter, each with their respective advantages and disadvantages. These are briefly outlined in this section.

2.10.1. Control Strategies of a Grid-tied Inverter

In [25], Wang and Chang compare two prominent control strategies for the control of a PWM inverters and evaluate their performance. These are Hysteresis Current (HC) Control as well as Space-Vector Control.

The principle of HC control is simple. A reference current band is defined and used to compare with the actual current. If the actual current crosses either boundary of the reference band the switching state of the applicable inverter-leg is inverted, which will drive the current in the opposite direction. The narrower the reference band, the smoother the output current waveform will be. However, there is a limit to how narrow the reference band can be made, which is dictated by the maximum switching frequency of the semiconductors used, and the operating and sampling speed of the control system. The narrower the reference band, the more frequent the boundaries will be breached, which increases the switching frequency [25]. A fast and easily implementable current control is the strong point of this control type, whereas the

demand for fast ADCs and fast and precise current detection can make it relatively expensive.

The Space-Vector Control has become more prominent in recent years and is widely used as an alternative to Sinusoidal PWM. The use of SV-PWM as compared to Sinusoidal PWM results in lower harmonic distortion and up to 15% better utilisation of the DC bus voltage. The improved utilisation of the DC bus allows for a lower DC-Link voltage in grid-tied applications, as the grid-side converter will be able to supply sufficient voltage levels at a DC-Link voltage of 15% lower than that required with Sinusoidal PWM. More recent work on variable speed systems use back-to-back converters and Space Vector control strategy on both converters, as it provides more sophisticated control of the machine and grid-side converter.

The governing equations of the grid-side converter are:

$$v_d = Ri_d + L\frac{di_d}{dt} + \omega_{grid} Li_q + u_d \tag{2.49}$$

$$v_q = Ri_q + L\frac{di_q}{dt} + \omega_{grid} Li_d + u_q \tag{2.50}$$

Where v_d and v_q are the converter voltages while u_d and u_q are the grid voltages in the dq-reference frame. The resistance R and inductance L are the total values of the impedances, and include grid impedances as well as filter impedances.

The real and reactive power components are calculated according to the equations presented below:

$$P_{grid} = \frac{3}{2} v_d i_d \tag{2.51}$$

$$Q_{grid} = \frac{3}{2} v_q i_q \tag{2.52}$$

2.10.2. Grid Filter

Another important aspect of grid-tied variable speed wind turbine systems is the actual connection to the grid.

In [26], [27] the authors discuss the design of a LCL-filter while comparing it to the simpler L- and LC-filter. The advantage of the LCL-filter over a L- or LC-filter is discussed further. The L-filter consists of a single inductance, in between the converter and grid, has a slow response time. This results in poor system dynamics, especially under fast changing conditions [26]. Furthermore the L-filter has a low attenuation (20dB/decade) which necessitates high switching frequencies in order to obtain sufficient attenuation of the resulting harmonics [27]. The LC-filter allows for a lower inductor value due to the additional capacitance, which consequently reduces losses and cost [26]. However, a LC-filter results in a varying resonant frequency as the grid impedance changes, which makes this filter undesirable for grid-connected applications [27].

In [27] and [26] the authors propose the use of a LCL-type grid filters to achieve low grid current distortion, reactive power production and better attenuation of harmonics (60dB/decade) at frequencies above the resonant frequency. The resonant frequency associated with this filter can be expressed as:

$$f_{res} = \frac{1}{2\pi}\sqrt{\frac{L_1+L_2}{L_1 L_2 C}} \tag{2.53}$$

Where L_1 and L_2 are the converter and grid-side inductor values respectively, while C is the capacitor value [27]. From this equation it is clear that the resonant frequency only depends on the filter components values chosen. This yields another advantage of the LCL-filter as it allows for relatively low switching frequencies, while achieving good harmonic attenuation [27].

2.11. Conclusions

The theory and governing equations which determine the performance of a wind turbine have been presented here, as well as the principles of MPPT. Furthermore the various topologies available to construct a WECS have been presented and

discussed. Special attention has been given to a variable-speed PMSG WECS which is the focus in this thesis. The available power converter topologies and their respective advantages and disadvantages have been presented as well as the options available to connect a WECS to the grid. Based on the presented model of a PMSG the available control strategies have been presented and their applications in existing projects discussed.

Chapter 3

A grid-tied Permanent Magnet Synchronous Generator WECS

3.1. Introduction

The system topology implemented in this thesis is presented here. This includes the development of a turbine emulator as well as the control of the machine and grid-side converters. Applicable system parameters, such as the grid-filter components, have been derived, based on the literature and theory discussed in the previous chapter. The previously discussed control strategies have been adopted for the system under consideration.

3.2. Components used in the implementation of a variable-speed PMSG-based WECS

A surface-mounted permanent magnet synchronous generator with 12 pole pairs and a rated speed of 240rpm is connected to the grid through a full back-to-back converter. The converter makes use of space-vector modulation to control the flow of active and reactive power between the machine and the DC-Link, as well as between

the DC-Link and the grid. The generator is assumed to be coupled directly to a fixed-pitch turbine and the converters are connected to the grid through a LCL-type filter. To facilitate the laboratory-based implementation of the system, the actual wind turbine is emulated by means of a DC-motor operated in torque control mode and coupled to the generator through a 6:1 gearbox. The gearbox is treated as part of the turbine and is required to match the rated speed of the DC-machine (1500rpm) to the rated speed of the generator (240rpm). Similarly, the grid voltage is stepped down via a transformer from 380V to 220V for safety and isolation. The transformer is considered as part of the grid and its impact on the operation of the system is neglected. The grid- and machine-side controls are independent and implemented using two dSAPCE DS1104 kits, which are connected to PCs which provide the user-interface. All control loops and signal feedback are implemented and processed in MATLAB/Simulink and the dSPACE Control Desk. A schematic overview of the system is provided below.

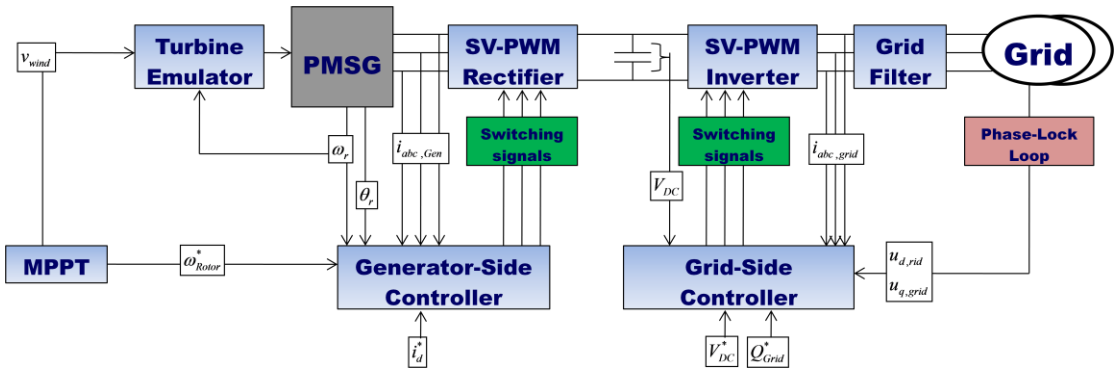

Figure 3.1: Schematic Overview of the Variable Speed WECS

Certain limitations that were encountered in the laboratory implementation of the system were implemented in simulation to allow for meaningful comparison between theory, simulations and experimental results. The DC-machine used to emulate the turbine's behaviour was rated at 3hp (2.24kW) which limits the maximum power and hence wind speed that can be emulated. However, the concept was proven at lower wind speeds of up to 7m/s.

3.3. Machine-Side Converter and Control

The machine-side converter consists of a standard 3-leg IGBT inverter stack. The control makes use of two fast current control loops, which are the inner control loops

of the system, and an outer control loop for speed control. All controllers are of the PI-type.

A schematic overview of the current control loops is shown in figure 3.2 below.

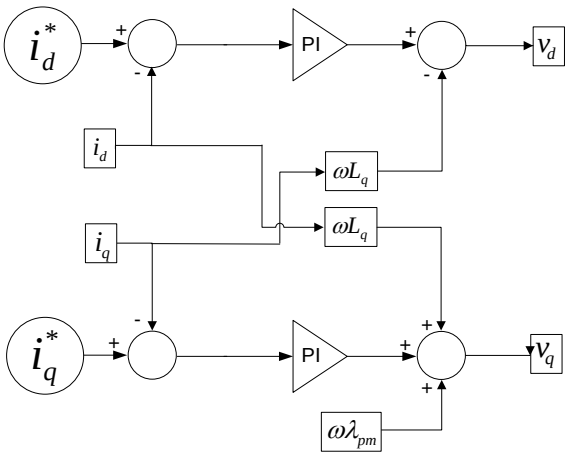

Figure 3.2: Schematic of the Current Control Loops

The speed control of the machine is implemented as an outer control loop which determines the reference value for the quadrature current and hence the applied torque. The d-axis current component can be adjusted independently depending on the control strategy implemented. A schematic overview of this control is provided in figure 3.3.

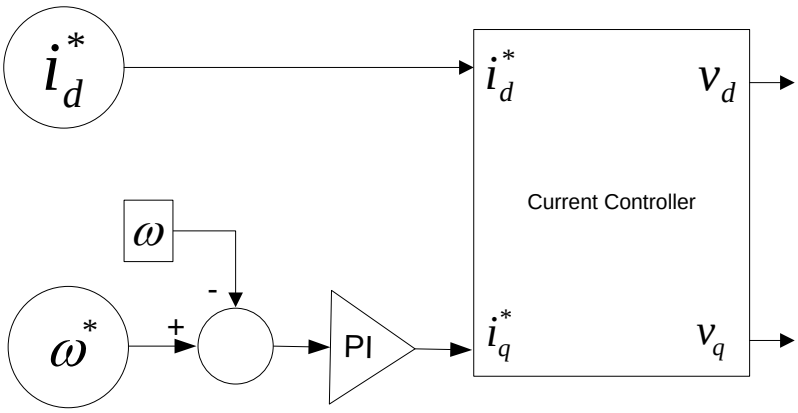

Figure 3.3: Schematic of the Speed-Control Loop

The gains of the PI controllers associated with the control of the machine-side converter are listed in the table below.

Table 3.1: Controller Gains

	d-axis current controller	d-axis current controller	Speed controller
Proportional Gain kP	5	5	0.2
Integral Gain kI	10	10	0.15

The complete machine-side control is shown as a schematic in figure 3.4.

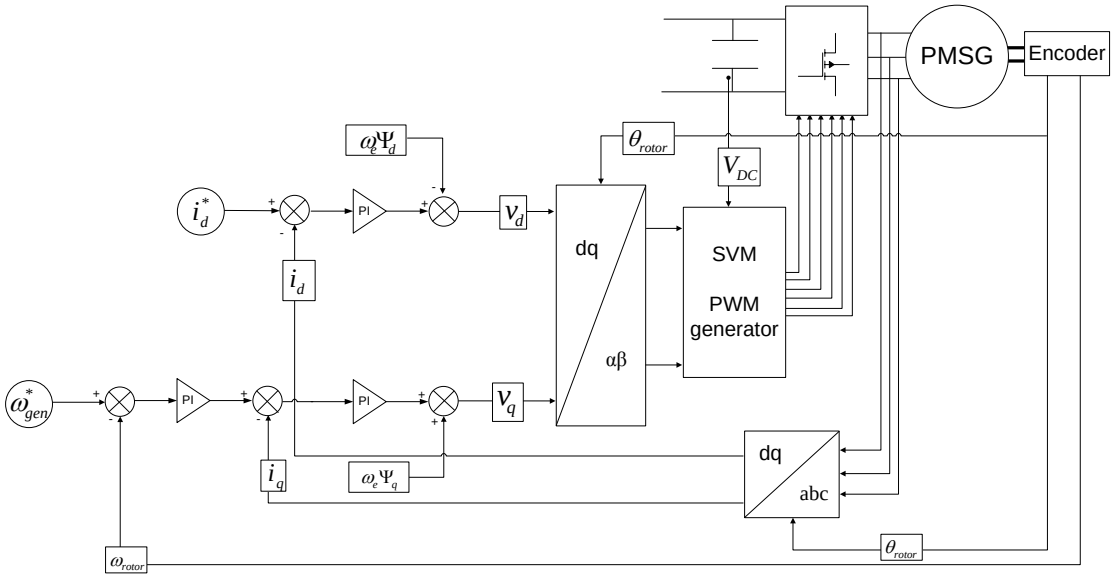

Figure 3.4: Machine-side control scheme

The d- and q-axis reference voltage components determined from the current control loops are converted into the stationary αβ-reference frame components according to the following equations, known as the inverse Parke transform:

$$\begin{bmatrix} v_\alpha \\ v_\beta \end{bmatrix} = \begin{bmatrix} \cos(\theta) & -\sin(\theta) \\ \sin(\theta) & \cos(\theta) \end{bmatrix} \begin{bmatrix} v_d \\ v_q \end{bmatrix} \tag{3.1}$$

where θ is the angle between the rotating dq-reference frame and the stationary αβ-reference frame. Aligning the d-axis with the axis of phase A of the generator means that θ is the angle between the axis of phase A and the rotor.

The resulting αβ-components of the stator voltage phasor are then fed to the SVM-block which calculates the switching times for each of the converter switches.

The measured currents at the generator terminal are converted into the dq-frame. This is done in two steps. First their αβ-components are computed according to the Clarke transform:

$$\begin{bmatrix} i_\alpha \\ i_\beta \end{bmatrix} = \frac{2}{3}\begin{bmatrix} 1 & -\frac{1}{2} & -\frac{1}{2} \\ 0 & \frac{\sqrt{3}}{2} & -\frac{\sqrt{3}}{2} \end{bmatrix}\begin{bmatrix} i_a \\ i_b \\ i_c \end{bmatrix} \tag{3.2}$$

The dq-components are obtained by transforming the αβ-components into the dq-frame according to the Parke transform:

$$\begin{bmatrix} i_d \\ i_q \end{bmatrix} = \begin{bmatrix} \cos(\theta) & \sin(\theta) \\ -\sin(\theta) & \cos(\theta) \end{bmatrix}\begin{bmatrix} i_\alpha \\ i_\beta \end{bmatrix} \tag{3.3}$$

These dq-current components are compared with the reference current values and the resulting errors are fed into PI controllers.

3.4. Grid-Side Converter and Control

The purpose of the grid-side converter is to maintain a fixed DC-Link voltage by transferring power delivered to the DC-Link by the generator, to the grid.

The grid-side converter is synchronised to the grid voltages by means of a Phase-Lock-Loop (PLL). The grid voltage phasor is chosen to coincide with the d-axis.

In addition to the transfer of real power into the grid, reactive power can be supplied independently as required. This is achieved by decoupling the control of the d- and q-axis current components. The principle is similar to the decoupling of the d- and q-axis current components on the machine-side which has been discussed in chapter 2.8. A schematic overview of this control is shown in figure 3.5.

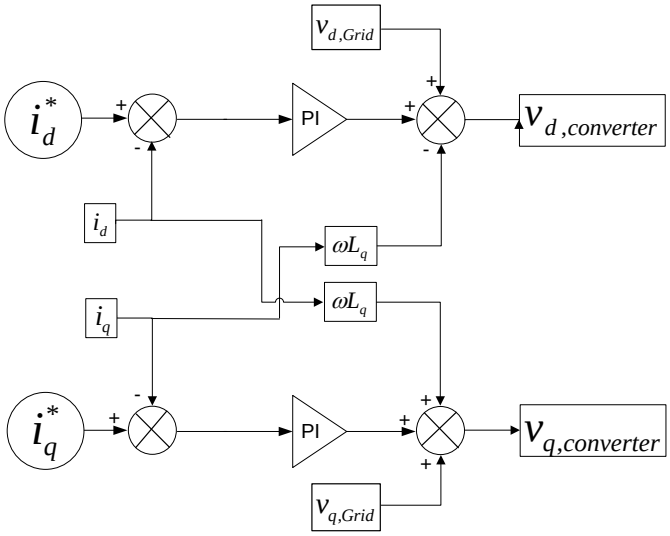

Figure 3.5: Schematic Overview of the Grid-Side Current Controller Loops

As presented in chapter 2, the real power is directly proportional to the d-axis current, since the grid voltage is constant. The DC-Link regulation is therefore implemented by controlling the reference value for i_d as required. This is done by means of an outer control loop as shown in figures 3.6 and 3.7. Notice that the Reference value for the DC-Link Voltage is subtracted from the actual measured value. This is due to the orientation of the reference frame which defines a current flowing into the grid as positive. When the DC-Link Voltage rises above its desired value the reference for i_d is increased by the PI controller and more power is transferred from the DC-Link into the grid.

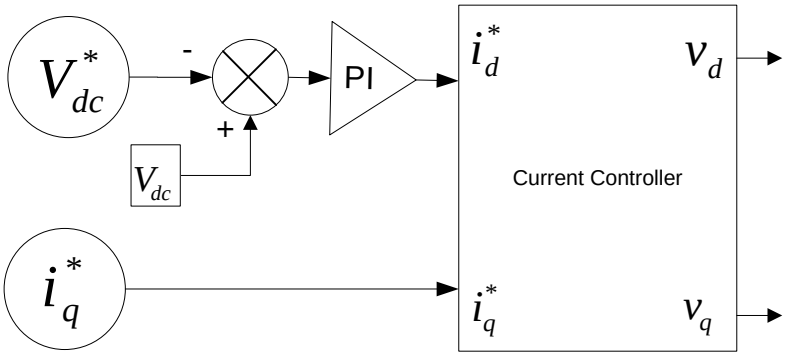

Figure 3.6: Schematic Overview of the DC-Link Control Loop

The complete grid-side control scheme is presented in figure 3.7. It uses the same inverse Parke, Parke, and Clarke transforms as presented in formulae 3.1, 3.2 and 3.3 respectively.

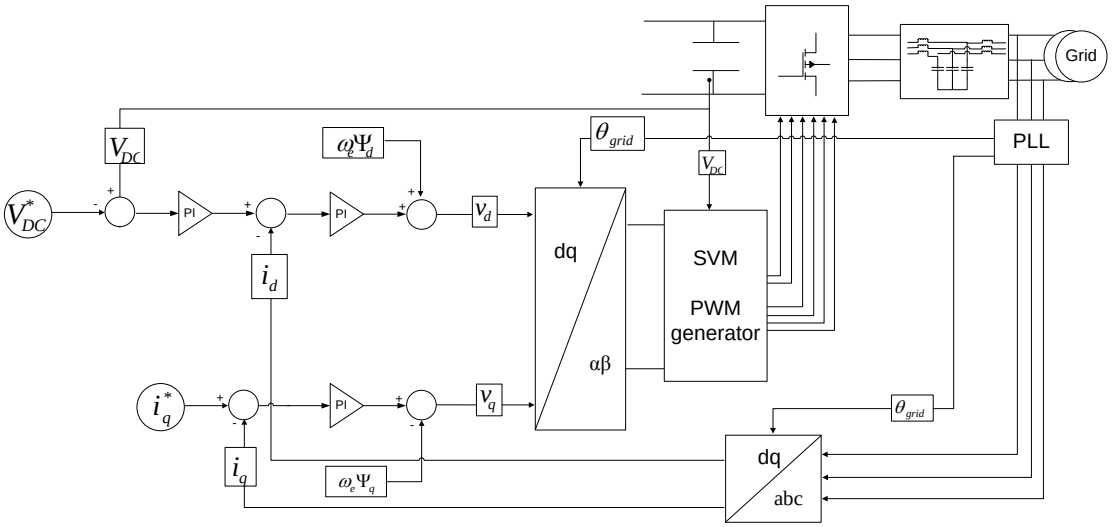

Figure 3.7: Grid-side control scheme

The reference angle for the two stationary reference frames is defined as the phase angle of the grid's phase A voltage. This angle is obtained by means of a Phase-Lock-Loop (PLL).

3.4.1. Grid-Filter Design

The filter connecting the grid-side converter to the grid is a LCL-type filter. This section presents the design process through which the filter component values are derived. To determine the appropriate values for the LCL-type filter, certain parameters need to be known. These are the rated power of the filter (S_n), the line-to-line voltage of the grid (U_n) and the switching frequency of the grid-side converter (f_{sw}).

According to [28], the base impedance is defined by equation (3.4).

$$Z_b = \frac{U_n^2}{S_n} \tag{3.4}$$

The base values for the inductance and capacitance are defined as:

$$L_b = \frac{Z_b}{\omega_b} \tag{3.5}$$

$$C_b = \frac{1}{\omega_b Z_b} \tag{3.6}$$

The ratings of the grid-filter in this project are as follows:

Power: $S_n = 2kVa$

Phase Voltage: $U_n = 220V_{rms}$

Base frequency: $\omega_b = 2\pi \cdot f_{grid} = 314.159\,rad/s$

DC-Link Voltage: $V_{DC} = 400V$

Rated Phase Current: $I_{Ph,RMS}$ =5.25A

Hence, the base impedance is found to be $Z_b = 24.2\Omega$ and the base inductance and capacitance to be $L_b = 0.077H$ and $C_b = 0.1315mF$ respectively.

According to [29] the total inductance of the filter L_T should be within the following range:

$$\frac{V_{DC}}{4\sqrt{3}\cdot i_{rip,peak}\, f_{sw}} \leq L_T \leq \frac{\sqrt{\frac{V_{DC}^2}{3} - U_n^2}}{\omega I_m} \tag{3.7}$$

Allowing the peak ripple current ($i_{rip,peak}$) to be 15% of the peak value of the fundamental (I_m), the total inductance should lie within the range defined by equation (3.8).

$$\frac{400V}{4\sqrt{3}\cdot 1.114A\cdot 10kHz} \leq L_T \leq \frac{\sqrt{\frac{(400V)^2}{3} - (2200V)^2}}{2\cdot\pi\cdot 50Hz\cdot 5.25A} \tag{3.8}$$

$$5.15mH \leq L_T \leq 42.6mH \tag{3.9}$$

During the design of the filter, the available inductor and capacitor values had to be considered to allow for implementation in the laboratory. The available capacitor values are $10\mu F$, $15\mu F$ and $50\mu F$. In order to minimise the reactive power contribution of the filter, a low capacitance value should be chosen. By connecting two capacitors in series the effective capacitance can be reduced to $5\mu F$.

Throughout literature the upper limit for the resonance frequency is given as half the switching frequency [29],[30]. The switching frequency used in this project is 10kHz. The maximum resonance frequency should therefore be lower than 5kHz.

Formulae (3.4) to (3.9) define the boundary values of acceptable filter component values. A simplified design method is used to obtain the values for the filter components. These are then compared to the boundary conditions defined in this section to ensure they are within the permissible limits.

3.4.2. Simplified Design Method

In [29], a simplified design method for grid-tied LCL filters is discussed which was used to derive the values for the grid-filter, while adhering to the derived range for inductance and capacitance as discussed in section 3.4.1. After calculating the relevant parameters they were compared to the limits discussed in the previous section to ensure their compliance for the laboratory implementation.

From [29] the ideal grid-side inductance is defined by equation (3.10).

$$L_g = \frac{U_n}{2 \cdot \sqrt{6} \cdot i_{ripm} \cdot f_{sw}} = \frac{220V}{2 \cdot \sqrt{6} \cdot 0.15 \cdot \sqrt{2} \cdot 5.25A \cdot 5000Hz} = 8.06mH \quad (3.10)$$

To obtain a good filter effect the inverter-side inductance should be half the grid-side inductance.

$$L_g = 2L_{inv} \quad (3.11)$$

Hence

$$L_{inv} = 4.03mH$$

The filter capacitance is obtained according to equation (3.12).

$$C_f = \frac{L_{inv} + L_g}{L_{inv} \cdot L_g \cdot (2\pi \cdot f_{res})^2} = \frac{0.00403 + 0.00806}{0.00403 \cdot 0.00806 \cdot (2\pi \cdot 5000)^2} = 0.38uF \quad (3.12)$$

Finally the capacitor value should be less than 15% of the base capacitance calculated.

$$C_f < 0.15 \cdot C_b \quad (3.13)$$

$$C_f < 19.72uF$$

The condition in equation (3.13) is satisfied by the derived value of $0.38uF$.

However, the smallest capacitance value available for the implementation in the laboratory was found to be $5uF$. This value considers considerably from the ideal value derived in equation (3.12). However the upper limit imposed by equation (3.13) is not exceeded and therefore the available capacitance of $5uF$ is used. The available inductor values were found to be closer to the ideal values. The final component values used in the laboratory implementation are:

$$C_f = 5uF$$
$$L_{gen} = 7mH$$
$$L_{grid} = 2.7mF$$

Calculating the resulting resonance frequency yields.

$$f_{res} = \frac{1}{2\pi}\sqrt{\frac{L_{gen}+L_{grid}}{L_{gen}\cdot L_{grid}\, C}} = \frac{1}{2\pi}\sqrt{\frac{0.007H+0.0027H}{0.007H\cdot 0.0027H\cdot 0.000005F}} = 1026Hz \qquad (3.14)$$

This is well above the fundamental frequency of 50Hz and below, 5kHz, the upper limit for the resonance frequency derived in chapter 3.2.1. Furthermore the total inductance as well as capacitance falls within the applicable limits.

$$5.15mH \leq L_T \leq 42.6mH$$
$$C_f = 5uF < 19.72uF$$

The derived filter parameters therefore fulfil the requirements for a grid-tied LCL filter as found in literature while making use of the components available, although the large capacitance might decrease the power factor on the grid side by introducing a reactive power component.

3.5. Applied Control Strategies

The theory behind the control of a WECS, which maximises its power output, was developed in chapter 2. Three control strategies were analysed and implemented in simulation and experimentally.

3.5.1. Maximum Torque per Current Control

As mentioned previously, this is the most common and established method of controlling a PMSG. The direct reference current component is maintained at zero to minimise the armature current at any given moment. The control strategy aims to minimise the copper losses in the machine under any operating conditions. It does not consider any other losses, such as core or stray losses.

$$i_d^* = 0 \tag{3.15}$$

This control strategy also provides the simplest reference for the d-axis current component as evident from expression (3.15).

3.5.2. Maximum Power Factor Control

In chapter 2.9.2, the unity power factor control has been discussed. Two approached have been discussed, by which a reference value for the d-axis current component leading to UPF, which are expressed in equations (2.25) and (2.30). Equation (2.25) defines the d-axis reference current component as a function of three variables (v_d, v_q, i_q), all of which keep changing and are interrelated. In equation (2.30) the d-axis reference current component only depends on the q-axis current component as well as two machine parameters which are constant. For this reason the d-axis reference current component is calculated according to equation (3.16). This is the same equation as (2.30).

$$i_d^* = \frac{-2L_q i_q^2}{\lambda_{pm}} \tag{3.16}$$

3.5.3. Maximum Efficiency Control

To maximise efficiency, both core and copper losses need to be minimised. This control strategy focuses on minimising the sum of these 2 loss components, thus attempting to maximise efficiency as discussed in section 2.9.3.

The core losses as a function of speed and current are given as:

$$P_{core} = k_h f B_{max}^n + k_e f^2 B_{max}^2 \tag{3.17}$$

The core losses can be approximated by the product of a frequency dependent function $K_c(f)$ and the stator flux (λ_s), which allows for the simplification of equation (3.17) to [31]:

$$P_{core} \approx K_c(f)\lambda_s^2 \tag{3.18}$$

Based on the tests carried out in chapter 6, the following relationship was established for the core and copper losses in the machine under consideration:

$$P_{core}(\omega, i_d, i_q) \approx$$
$$(0.00141 \cdot \omega^2 + 0.166 \cdot \omega) \cdot \left(\left(\lambda_{pm} - L_s i_d\right)^2 + \left(-L_s i_q\right)^2\right) \tag{3.19}$$

Where

$K_c(f) = (0.00141 \cdot \omega^2 + 0.166 \cdot \omega)$

λ_s is defined in equation (2.17)

$$P_{cu} = 3 \cdot i_s^2 \cdot R_s = 3 \cdot (i_d^2 + i_q^2) \cdot R_s \tag{3.20}$$

This results in an expression for the total controllable losses in the machine as a function of speed and stator current as follows:

$$P_{contr\ .losses}(\omega, i_d, i_q) =$$
$$K_c(f) \cdot \left(\left(\lambda_{pm} - L_s i_d\right)^2 + \left(-L_s i_q\right)^2\right) + 3 \cdot (i_d^2 + i_q^2) \cdot R_s \tag{3.21}$$

By differentiating this equation with respect to i_d the loss minimisation condition can be established and the ideal direct current component calculated.
Thus,

$$\frac{d}{di_d}\left[P_{contr\ .losses}\left(\omega, i_d, i_q\right)\right] = -2L_s\lambda_{pm}K_c(f) + 2L_s^2 i_d K_c(f) + 6R_s i_d \quad (3.22)$$

Setting

$$\frac{d}{di_d}\left[P_{contr\ .losses}\left(\omega, i_d, i_q\right)\right] = 0 \quad (3.23)$$

yields the following condition for minimum losses in the machine.

$$i_d = \frac{-K_c(f)L_s\lambda_{pm}}{K_c(f)L_s^2 + 3R_s} \quad (3.24)$$

Applying this to the machine, results in.

$$i_d^* = \frac{-\left(0.00141\cdot\omega^2 + 0.166\cdot\omega\right)\cdot 0.0065H\cdot 0.74Wb}{(0.00141\cdot\omega^2 + 0.166\cdot\omega)\cdot(0.0065H)^2 + 3\cdot 0.76\Omega} \quad (3.25)$$

Plotting equation (3.25) as a function of speed over the applicable range and approximating it as a quadratic function results in equation (3.26).

$$i_d^*(n) = -0.000003094\cdot n^2 - 0.0003682\cdot n \quad (3.26)$$

, where n is the generator speed in rpm.

From the analysis above, it is evident that the ideal direct current component is only a function of speed. This is expected since the quadrature current component is treated as a constant and is dictated by the MPPT algorithm. As discussed in the literature throughout chapter 1 and 2, this makes both current components a function of speed, since the q-axis current component is required to maintain the desired speed. The ideal d-axis current as a function of speed is shown below.

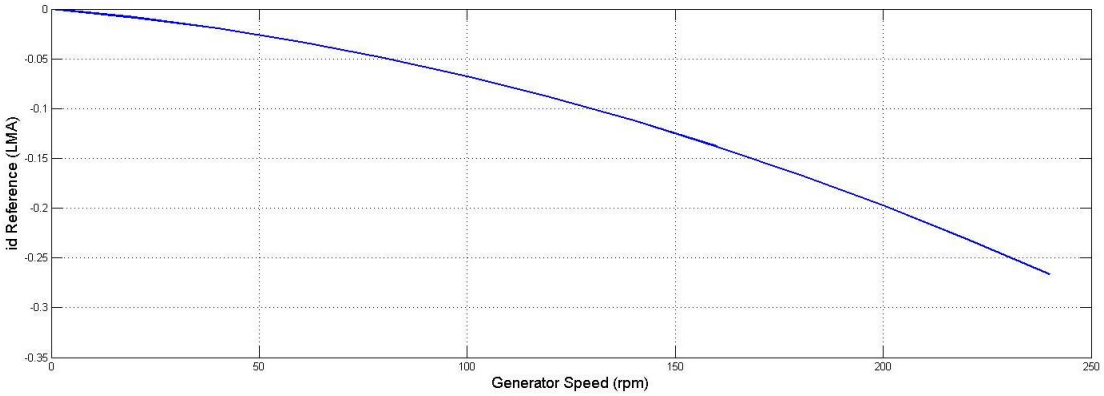

Figure 3.8: id Reference for Loss Minimisation

3.6. Conclusions

This chapter has presented the theory behind and the development of the specific WECS in this thesis. An overview of the components which make up the system is given. The control theory of the individual components, the turbine emulator, generator side converter and grid side converter has been developed and presented here. The adoption of the three control strategies to the specific parameters of the PMSG used in the WECS has been shown and the necessary formulae have been developed.

Chapter 4

Analytical Results

4.1. Introduction

This chapter analyses the WECS's performance theoretically and predicts the expected power production. Machine parameters are obtained from the laboratory as presented in chapter 6. These include stator winding impedance, mechanical losses as a function of speed and core losses as a function of speed and loading. The applicable parameters are listed in table 4.1. Perfect tracking of the reference speed has been assumed throughout the analysis and thus the maximum power is extracted from the wind. The performance of the machine is predicted analytically based on the formulae for the loss components and machine torque presented earlier. The analysis is carried out for the specific WECS in this thesis as well as a modified model to highlight the impact of specific generator parameters on the performance of the different control strategies.

Table 4.1: PMSG parameters as obtained experimentally

Stator Resistance	0.76Ω
d-axis stator inductance (L_d)	6.5mH
q-axis stator inductance (L_q)	6.5mH
PM excitation (λ_{pm})	0.74Wb
Core Loss Constant ($K_c(f)$)	$K_c(f) = 0.01346 \cdot \omega^2 + 1.585 \cdot \omega$
Rotational Losses	$P_{rotational}\ (\omega) = 0.03314 \cdot \omega^2 + 13.75 \cdot \omega - 23.5W$

4.2. Projected power extracted from the incident wind

The range of wind speeds investigated is 4m/s up to 9m/s in steps of 0.2m/s. Based on the curve relating power coefficient to TSR, the maximum power coefficient is maintained for all wind speeds. From equation (2.1) the ideal turbine speed is a function of wind speed according to.

$$\omega_{opt} = \frac{v_{wind} \cdot \lambda_{opt}}{R} \tag{4.1}$$

Based on equation (4.1) the turbine speed reference for MPPT is obtained as a function of wind speed. This is shown in figure 4.1.

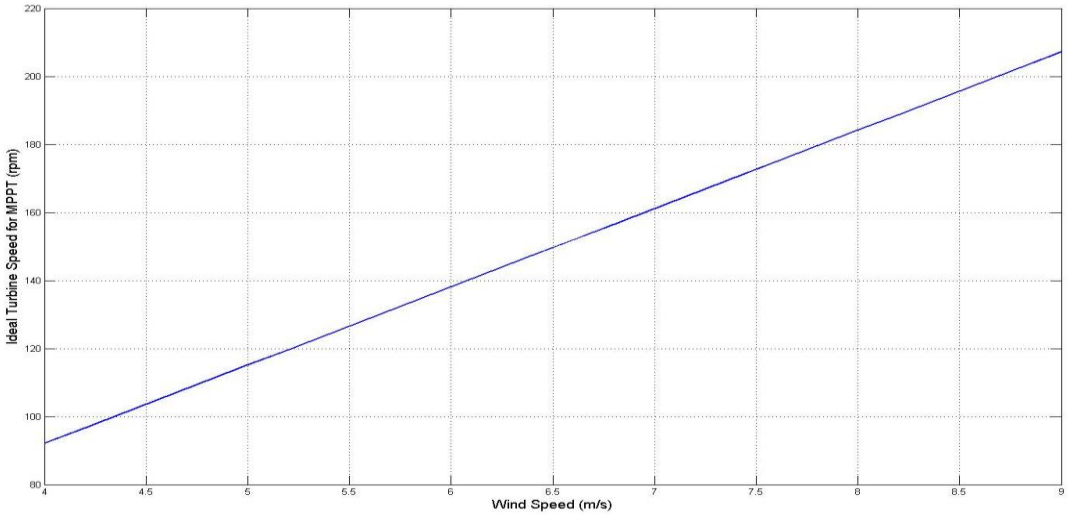

Figure 4.1: Ideal Turbine Speed for MPPT as a function of Wind Speed

The maximum aerodynamic power extracted from the incident wind is calculated according to equation (2.2), as shown in figure 4.2.

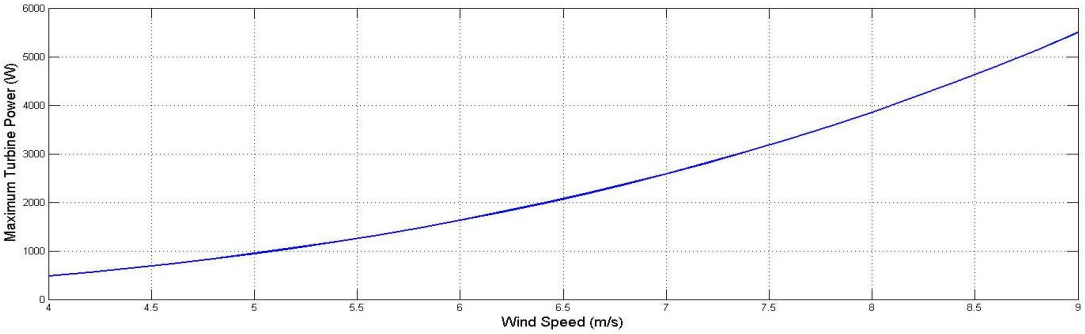

Figure 4.2: Maximum Turbine Power as a function of Wind Speed

The aerodynamic turbine power as a function of wind speed, shown in figure 4.2, assumes that the turbine is operated at its ideal TSR and therefore maximum power coefficient (C_p).

4.3. Projected Generator Performance under different control strategies

From the speed and power values, the applicable turbine torque is obtained which in turn yields the required quadrature current for the generator to maintain that ideal speed according to equation (4.2).

$$i_q = \frac{2 \cdot T_{em}}{3 \cdot p \cdot \lambda_{pm}} = \frac{2 \cdot (T_{shaft} - T_{friction\ ,windage\ })}{3 \cdot p \cdot \lambda_{pm}} \quad (4.2)$$

The required electromagnetic torque is the difference between the developed shaft torque and the torque experienced by the machine due to friction and windage. This is obtained experimentally in the laboratory as described in chapter 6.

The required quadrature current is the same regardless of the control strategy applied, due to the non-saliency in the machine. From equation (4.2) the required quadrature current component is calculated, as shown in figure 4.3 below.

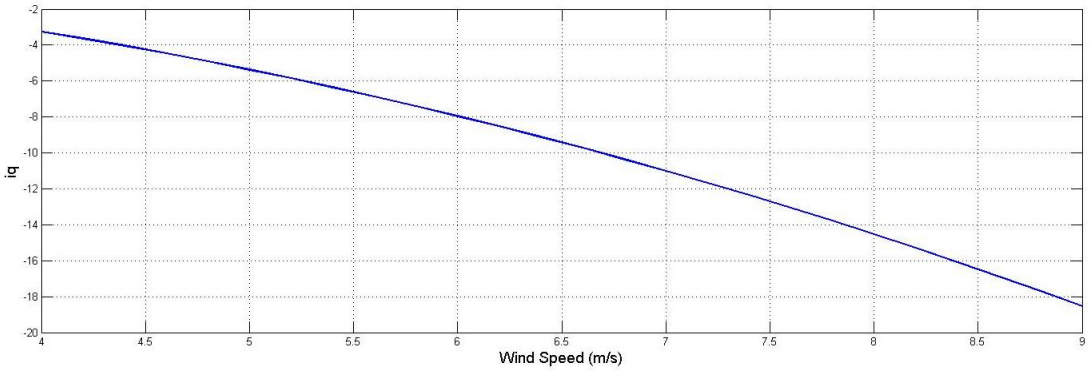

Figure 4.3: Ideal Generator quadrature current as a function of Wind Speed

From the machine speed and loading, the respective direct current component for each of the control strategies are calculated according to the formulae derived in section 2.9.2, 2.9.3 and 2.9.4. The formulae are shown in table 4.2 below.

Table 4.2: Formulas to obtain direct current component

Control Strategy	id Reference:
Max. Torque per Current	$i_d = 0$
Unity Power Factor	$i_d = \frac{-2L_q i_q^2}{\lambda_{pm}}$
Loss Minimisation Algorithm	$i_d = \frac{-K_c(f)L_s\lambda_{pm}}{K_c(f)L_s^2 + 3R_s}$

The resulting trajectories of the direct current components are shown as functions of wind speed in figure 4.4.

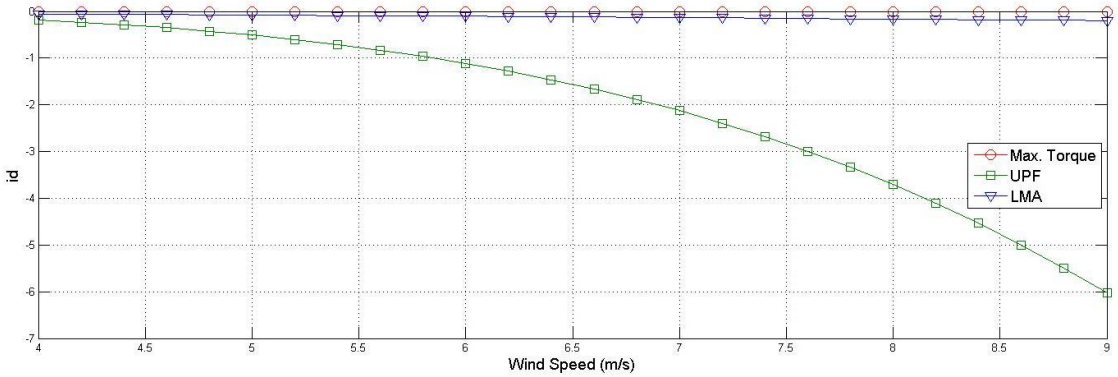

Figure 4.4: Direct current reference as a function of wind speed

From figure 4.4 it can be seen that the d-axis current component obtained from the LMA control differs only slightly from the maximum torque per current control, where it is maintained at zero. Based on this, the performance of the two control strategies is expected to be very similar. The UPF control results in an exponential trajectory for its d-axis reference current component. This implies that the copper losses will increase in a similar manner with wind speed.

The expected generator output power under different control strategies is derived by subtracting the predicted copper losses, core losses as well as friction and windage losses from the calculated shaft power as shown in the power flow diagram in figure 4.5.

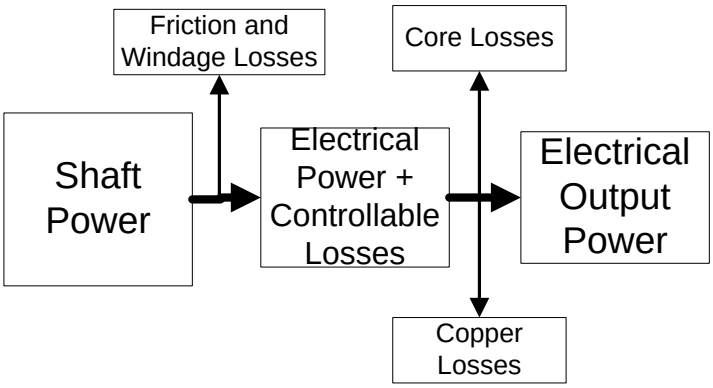

Figure 4.5: Analytical Power Flow diagram

Mathematically this is expressed by equation (4.3)

$$P_{elec.} = P_{shaft} - P_{cu} - P_{core} - P_{friciton\ ,windage} \quad (4.3)$$

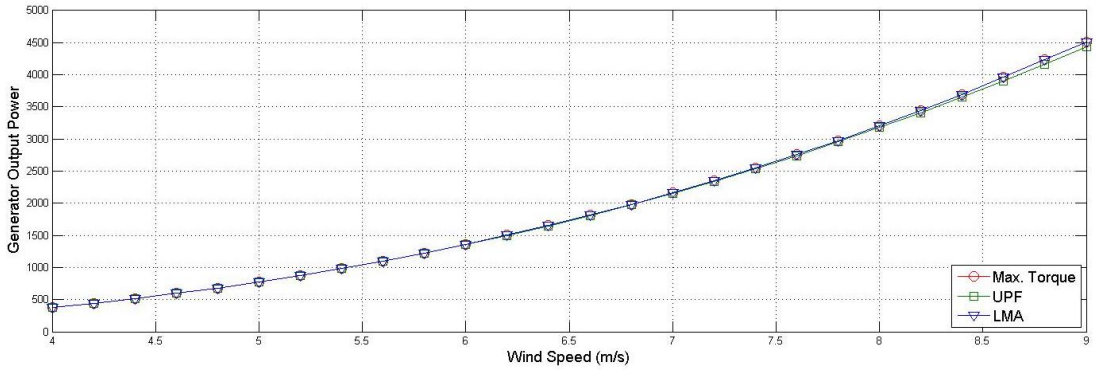

Figure 4.6: Calculated Generator Output Power as a function of wind speed

As shown in figure 4.6, there is very little difference between the theoretical generator output power produced under maximum torque per current control ($i_d = 0$) and the LMA control. This is expected from the almost identical trajectory of their respective d-axis current components. They both perform better than the Unity Power Factor approach although the difference is marginal. The wind speed range extends beyond the range investigated in simulations and experimentally. The difference between UPF Control and the two other control strategies becomes more evident when plotting the projected generator efficiency as a function of wind speed as shown in figure 4.7. The generator efficiency has been calculated according to:

$$\eta_{gen} = \frac{P_{elec.}}{P_{shaft}} \quad (4.4)$$

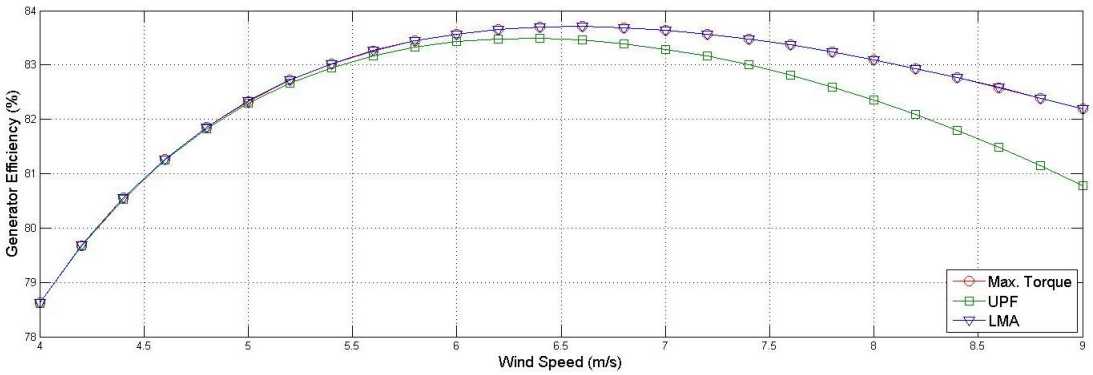

Figure 4.7: Generator Efficiency as a function of wind speed

As expected from figure 4.6, the UPF control becomes less viable at higher wind speeds which translate to higher loading. The resulting increase in stator current makes this approach the least efficient due to the increased copper losses while the maximum torque per current control produces an identical result to the Loss Minimisation Control. Three factors can be cited as reasons for this. Firstly, the estimated core loss contribution to the overall losses in the machine is very small compared to the copper losses which results in the two control principles giving very similar reference values for the d-axis current component as shown in figure 4.4. The second reason for the similar results of the two afore-mentioned control strategies is the low stator impedance of the machine, especially the low inductance. A low stator inductance means that the change in total stator flux due to an applied direct current component is small, as can be seen from the expression for the core losses, shown in equation (3.19). Hence the incurred core losses are only marginally reduced. Increasing the direct current component further decreases the core losses but leads to an even larger increase in copper losses. Finally, the non-saliency of the machine considered means that no reluctance torque component is produced by the d-axis current component as opposed to a machine with saliency. In a machine with saliency the d-axis current component contributed to the developed torque through the reluctance torque which decreases the total stator current and therefore reduces copper losses. This has been discussed in literature in [7] and [9].

To validate the principle of the LMA as well as to verify the argument that the low stator impedance does prohibit the LMA to improve the efficiency of the machine under consideration, the same analysis was carried out with an increased stator impedance as listed in table 4.3. In this analysis the core loss constant as a function of frequency was modified as well to emphasise the core losses compared to the copper losses. The modified core loss constant is shown in figure 4.8.

Table 4.3: Increased Stator Impedance

Stator Resistance	Stator Inductance
2.4Ω	51mH

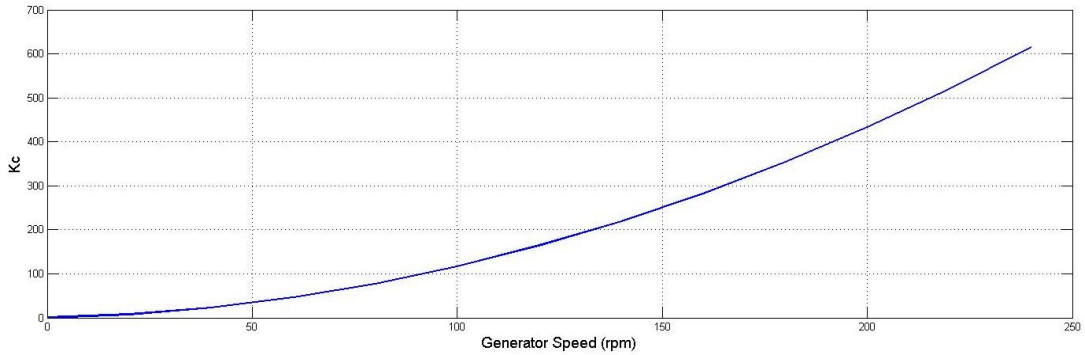

Figure 4.8: Increased Kc vs. Generator Speed

Due to the increased stator current under Unity Power Factor Control, this is not an optimal approach for a machine with high impedance. This is evident from equation (3.16) where the d-axis current reference for UPF control is a square function of inductance. Furthermore, equation (2.21) shows the quadratic relationship between copper losses and stator current. The resulting copper losses under UPF would make this control strategy extremely inefficient. Hence only the maximum torque per current and LMA control have been compared here.

Based on the formulae listed in table 4.2 the applicable reference values for the d-axis current components are plotted as a function of wind speed in figure 4.9. The huge value for id under UPF control is shown which makes this control unsuitable as stated.

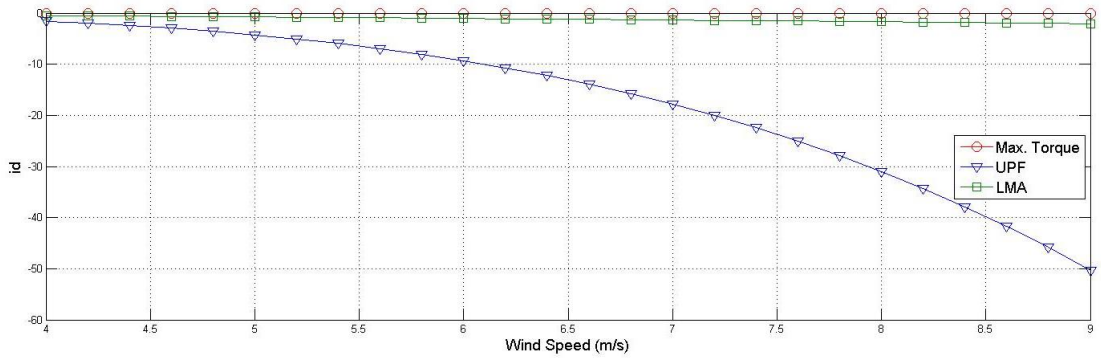

Figure 4.9: Direct current reference vs. wind speed

Taking into account the applicable losses, by including friction and windage, copper and core losses, the projected output power as a function of wind speed was obtained and is shown in figure 4.10.

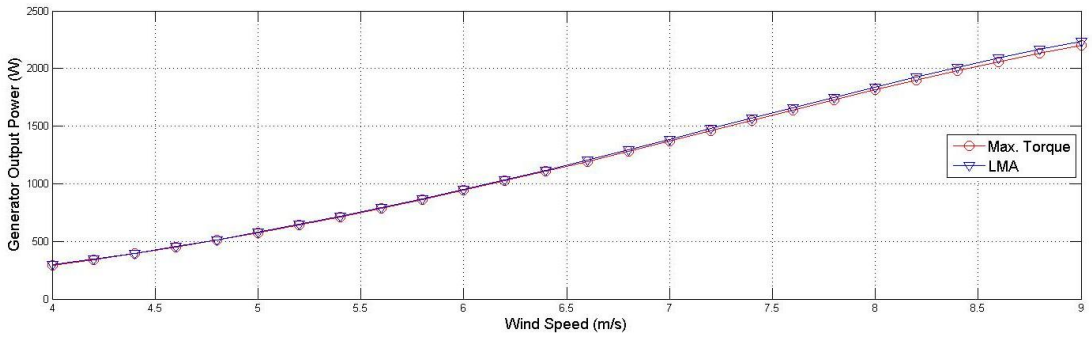

Figure 4.10: Projected generator output power vs. wind speed

With the same turbine characteristics the mechanical power which is extracted from the wind remains the same as shown in figure 4.2. The generator efficiency is calculated as the ratio of output electrical power to the power extracted from the wind, according to equation (4.4). This is shown in figure 4.11.

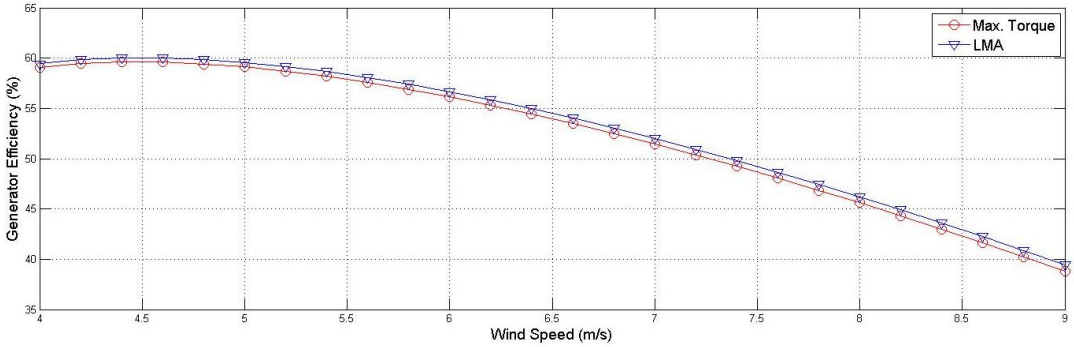

Figure 4.11: Projected Generator Efficiency vs. Wind Speed

A relatively small improvement in efficiency is obtained from the LMA and is compared to the maximum torque per current control. The improvement in efficiency is shown in figure 4.12.

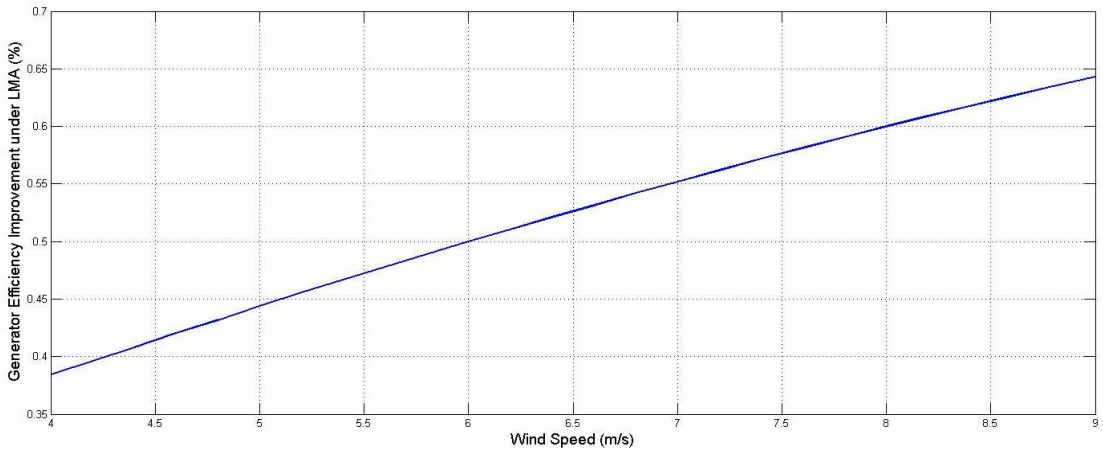

Figure 4.12: Generator Efficiency Improvement under LMA control compared to max. torque per current control

The graph in figure 4.12 shows a slight improvement in generator efficiency which becomes more evident at higher speeds and loading. This is consistent with the findings discussed in literature. However the improvements are very small. It shows that the machine parameters do impact on the performance of the LMA, although this seems to only contribute a small portion. The machines considered in literature which show a more significant efficiency improvement all have saliency. This is the more significant contribution to the efficiency improvement discussed in [4], [7] and [9].

4.4. Conclusions

The performance of the generator under three control strategies has been predicted analytically. Based on the parameters obtained experimentally for the machine in this thesis it was found that the LMA does not improve machine performance, due to the nature of the machine, mainly the absence of reluctance torque component in a surface-mounted machine. A modified version of the PMSG used has been analysed, which shows a slight efficiency improvement under LMA control compared to the maximum torque per current control. The improvement is very slight, nevertheless showing that the LMA can be used to improve machine efficiency. However it is clear that only certain machine types will show a significant improvement.

Chapter 5

Simulation of a variable-speed PM WECS

5.1. Introduction

The implementation of the PM WECS in MATLAB/Simulink is discussed in this chapter. The main parts of the WECS are simulated individually, where after the complete system is simulated. The results obtained from these simulations are presented and discussed here.

5.2. Simulation Overview

The purpose of simulating a system is to provide quick and affordable way of validating the performance of a system implementing it experimentally. As mentioned in the previous chapter, the system was tested at wind speed well below rated wind speed (12m/s) in order to accommodate the smaller DC-machine. The wind range investigated was from 4m/s to 7m/s.

5.3. Turbine Emulator

The turbine emulator was implemented in Simulink. A block diagram of the emulator is shown in figure 5.1.

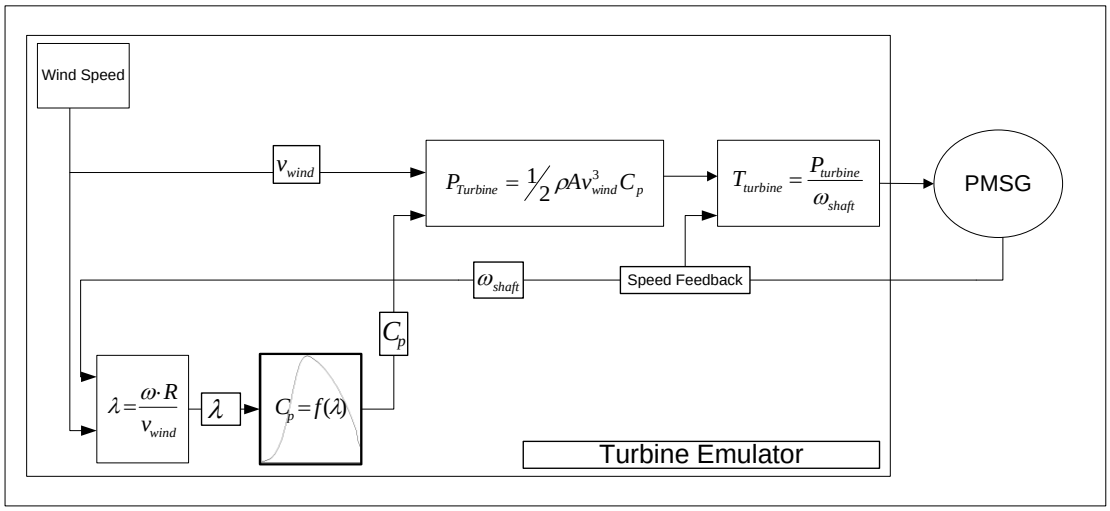

Figure 5.1: Turbine Emulator Scheme

The emulator has two input signals, the wind speed and the machine speed. Based on the on the data supplied by the turbine manufacturer the power curves were implemented in the form of a look-up table. The applied shat torque is then calculated as a function of the wind speed and the instantaneous shaft speed according to equations (2.2) and (2.3). The relationship between shaft speed and the resulting shaft power at different wind speeds is shown below.

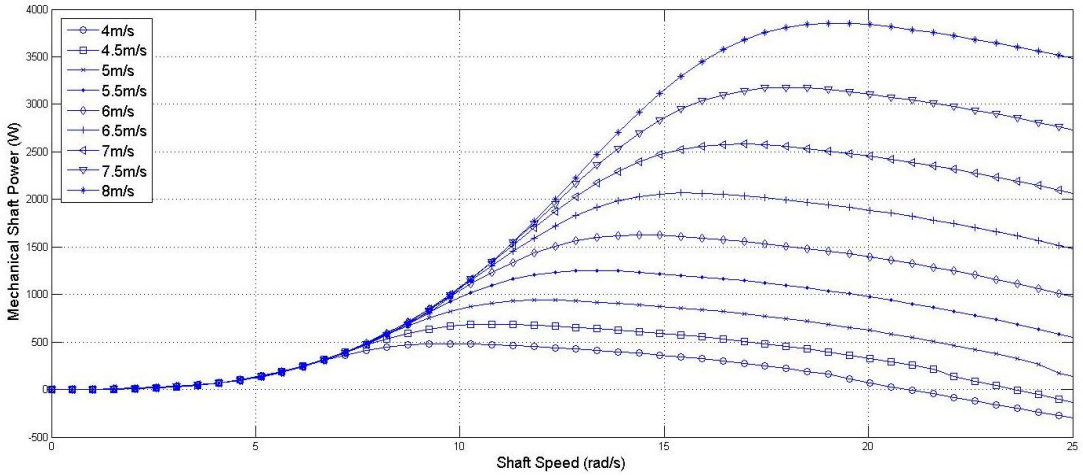

Figure 5.2: Wind Turbine Emulator Simulation

The turbine emulator is operating as expected with no variation between the expected outcome and the simulation. Additional factors which affect the behaviour of the turbine emulator were discussed in chapter 2.3 and include: tower shadowing,

furling as well as the impact of inertia and mechanical losses. These factors have not been included in the simulations or the experimental setup in chapter 6.

5.4. Controlling the Machine-Side Converter

To validate the control principles of the generator side converter, it is simulated alone without the grid-side converter, thus removing any possible external impact on the machine side converter.

5.4.1. Current Control Mode

The machine is controlled by two inner current control loops for the direct and quadrature axis components of the stator current, respectively. To validate the correct operation of the two current control loops, the machine is simulated without the outer speed control loop. The machine speed is simulated to be constant, while the q-axis reference current is stepped and the resulting output observed. The d-axis current component is maintained at zero throughout. A passive impedance resistance of 600Ω is connected across the DC-Link to dissipate the generated power. Initially, the machines speed is set to its rated speed of 240rpm and then stepped down to half its rated value, i.e. 120rpm. Figure 5.3 below shows the current response to a step input in quadrature current reference at both operating speeds.

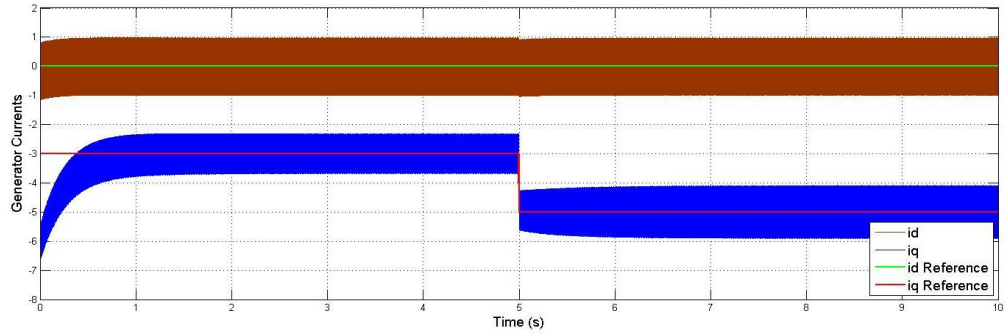

(a)

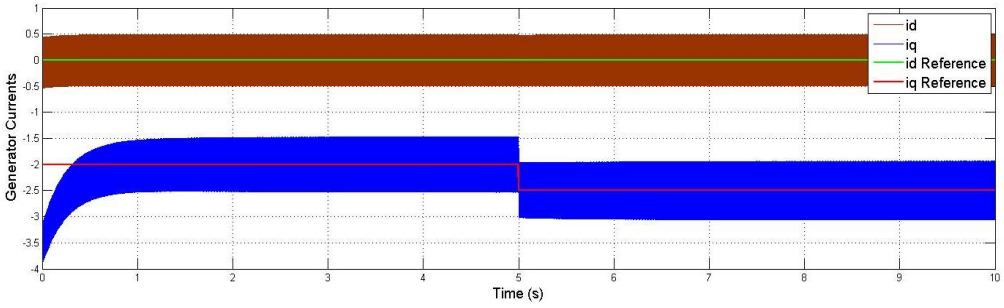

(b)

Figure 5.3: Generator Current Response at rated speed (a) and half rated speed (b)

As shown in figures 5.3 (a) and (b) the direct current component is maintained at zero while the quadrature current is stepped from -3A to -5A and -2A to -2.5A at speeds of 120rpm and 240 rpm respectively. Due to the low impedance of the machine, the current ripple is relatively high.

When the current drawn from the generator is increased, the DC-Link Voltage rises until the current dissipated in the resistor matches the current fed into the DC-Link from the machine. This is illustrated in figures 5.4 and 5.5, which shows the currents flowing in and out of the DC-Link capacitor and the accompanying change in DC-Link Voltage. The current shown have been filtered to remove the current ripple caused by the PWM switching.

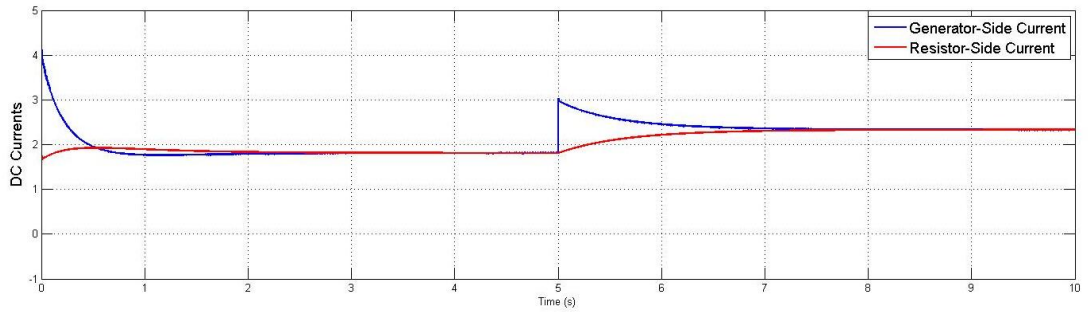

(a)

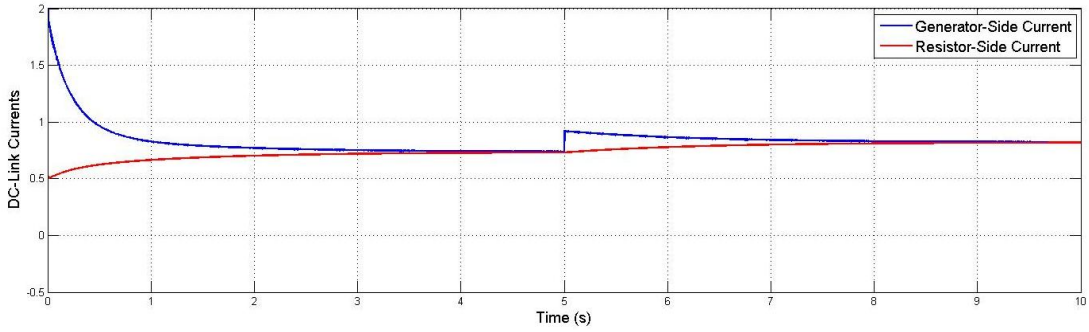

(b)

Figure 5.4: DC-Link Currents (filtered) at rated speed (a) and half rated speed (b)

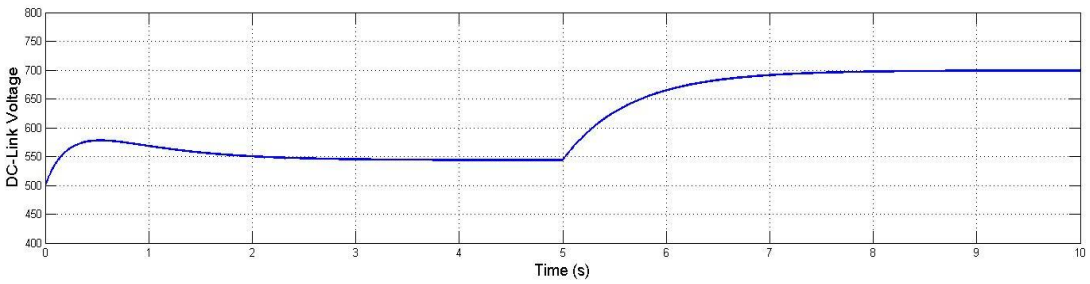

(a)

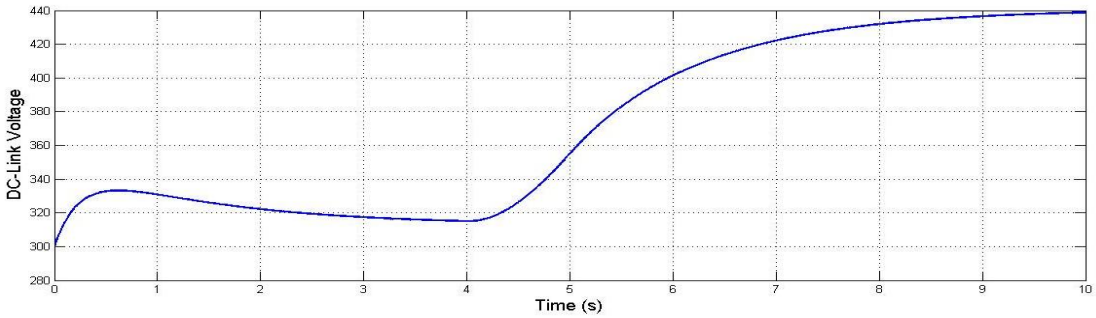

(b)

Figure 5.5: DC-Link Voltage at rated speed (a) and half rated speed (b)

According to equation (2.15) the generated power is proportional to the equadrature current component in the generator. Stepping up the q-axis current component therefore equalt a step increase in power produced. The power dissipated in the resistive load is given as:

$$P_{Res} = \frac{V^2}{R} \tag{5.1}$$

Since the resistance is constant, an increase in DC-Link voltage is expected. This is evident as shown in figure 5.5.

In a surface mounted PM machine the current is directly proportional to the quadrature current component as discussed in chapter 2 and expressed by equation (2.20).

The mechanical power developed is calculated according to:

$$P_{shaft} = T_{em} \cdot \omega_{shaft} \tag{5.2}$$

$$P_{shaft} = {}^{3}/_{2} \cdot p \cdot \lambda_{pm} \cdot i_q \cdot \omega_{shaft} \tag{5.3}$$

Figure 5.6 shows the shaft power developed during the step tests.

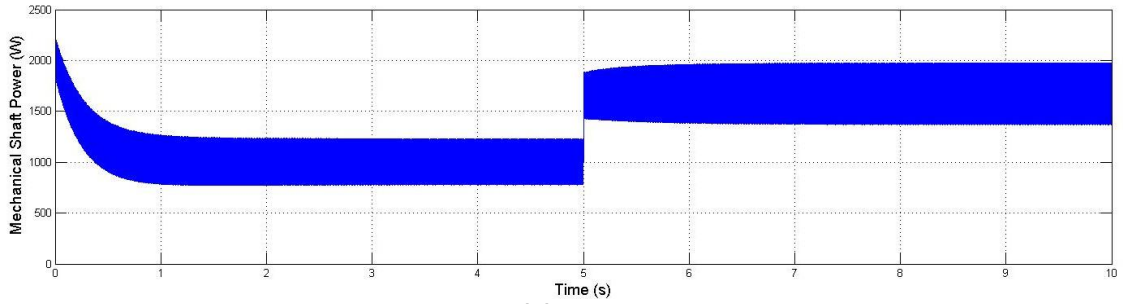

(a)

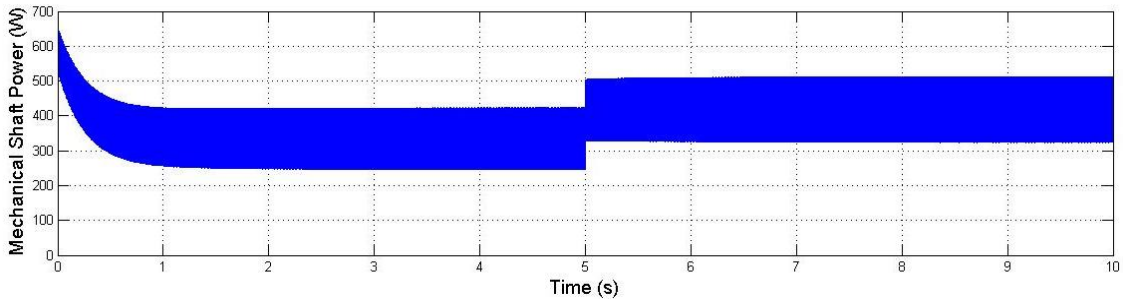

(b)

Figure 5.6: Shaft Power developed at (a) rated speed and (b) half rated speed (b)

The Simulink Model used in these simulations is shown in figure 1 of Appendix D.

5.4.2. Speed control mode for the implementation of MPPT

As discussed in chapter 2.2 the amount of power captured from the wind depends on the turbine and hence generator speed. Good speed control is essential to achieve successful maximum power point tracking. The tracking of a speed set-point is investigated through simulations in this section. This is done by removing the turbine emulator as well as grid-side converter. The shaft torque is therefore manually set to a certain value. Figure 5.7 shows a schematic of the simulation in this section.

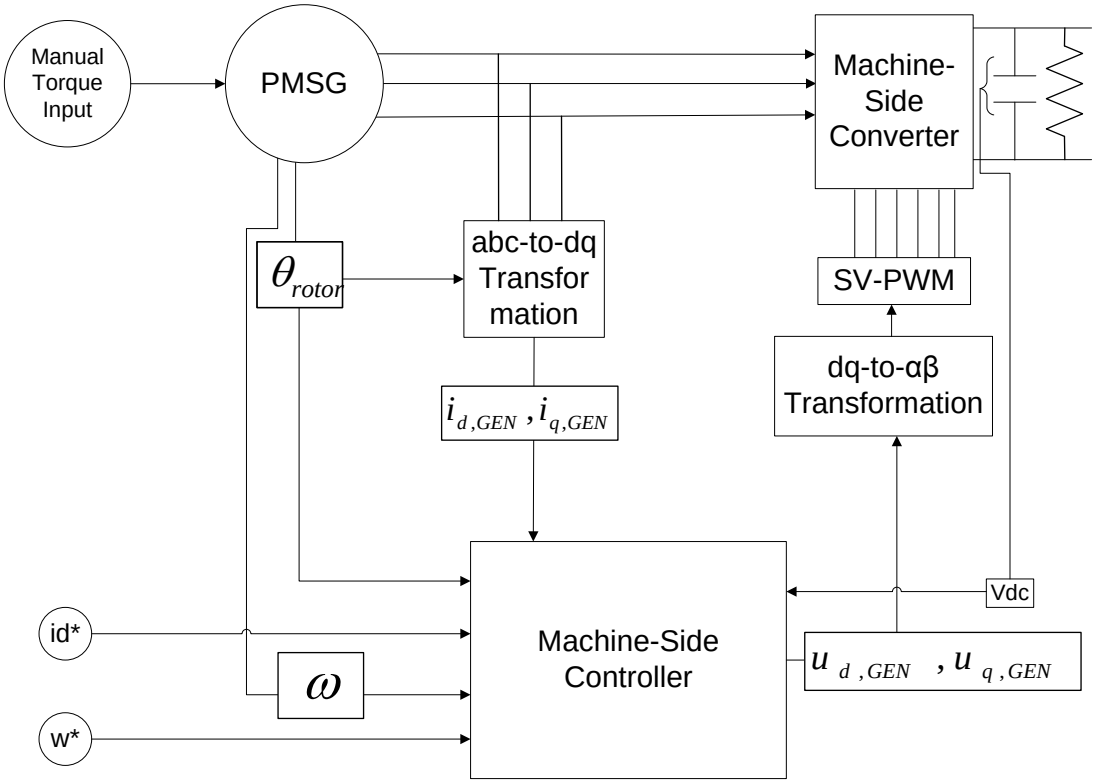

Figure 5.7: Principle speed control scheme

The input signals to the system are the applied shaft torque and the speed set point. Both signals were stepped at different times to investigate the systems dynamic response. During these tests, the direct current reference is maintained at zero since it has no influence on the machines torque and hence does not influence the speed control.

The relationship between applied torque and resulting quadrature current to maintain the desired speed can be observed in figures 5.8, 5.9, and 5.10. At t=1.5 seconds, the speed is stepped from 12rad/s up to 15rad/s, the current controller steps down the quadrature current to allow the generator to accelerate to the desired speed. The response shown is relatively short (0.5seconds) with little overshoot. The applied shaft torque is then increased at t=3 seconds. There is a slight change in generator speed while the quadrature current component is increased proportionally to the increase in torque. Similar behaviour can be observed at t= 7 seconds, when the torque is reduced to 35Nm. This causes a small dip in speed before the quadrature current compensates to achieve the desired speed.

At t= 5 seconds the speed reference is increased while the applied torque is kept constant. In order to increase the generator speed the quadrature current component is reduced until the speed has increased to its reference value.

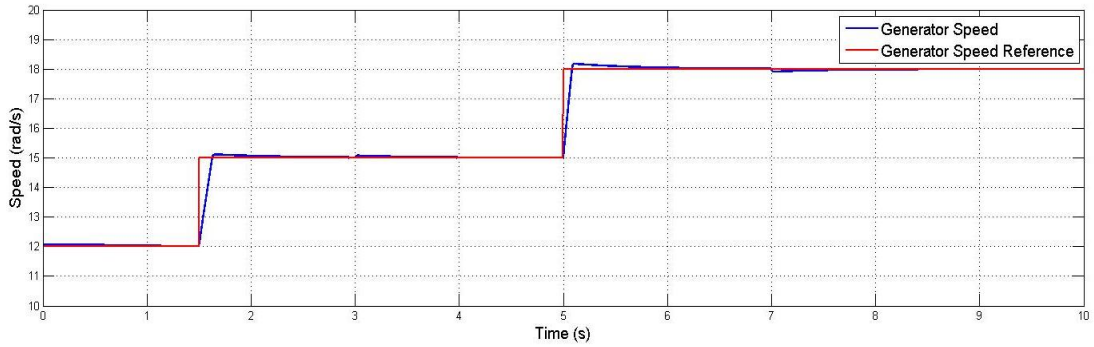

Figure 5.8: Simulated Speed Response

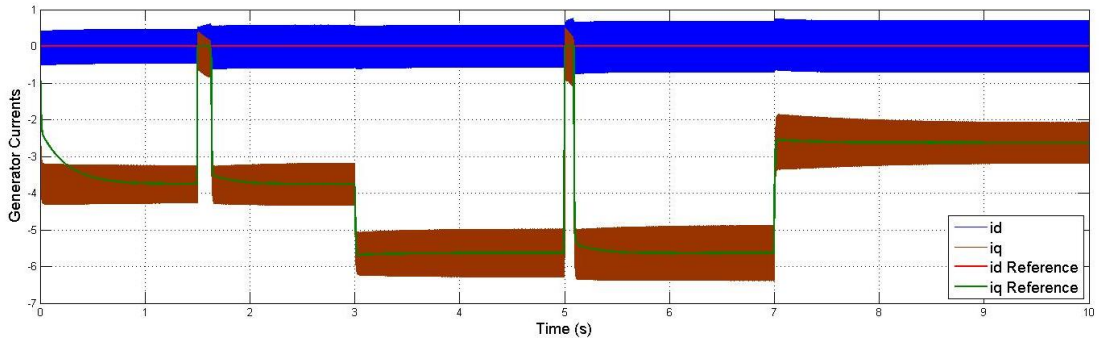

Figure 5.9: Simulated Generator Torques

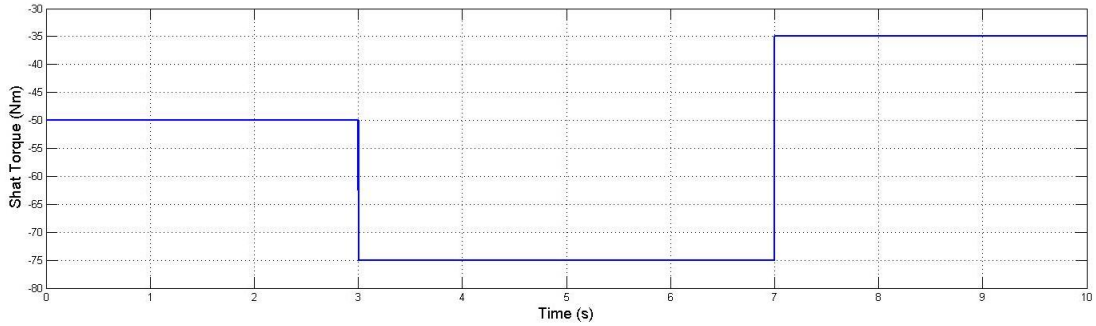

Figure 5.10: Mechanical Shaft Torque applied

The difference between electromagnetic torque developed and the mechanical torque applied determines the acceleration of the machine. The model ignores friction and windage for simplicity.

Hence:

$$\frac{d}{dt}\omega_{gen} = \frac{1}{J}(T_{em} - T_m) \qquad (5.4)$$

This can be observed when the torque difference and the machine speed are overlaid as shown in figure 5.11 below.

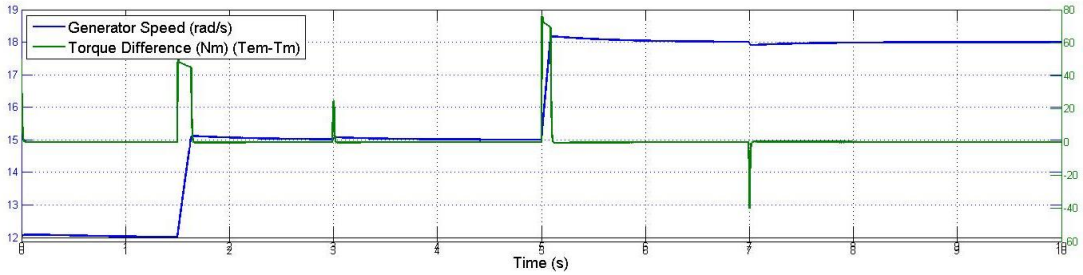

Figure 5.11: Torque difference and Generator Speed

Increasing or decreasing the generator currents results in a proportional change in current flowing into the DC-Link Capacitor. The difference between this current and the current dissipated in the resistor causes a change in DC-Link Voltage as shown in figure 5.12.

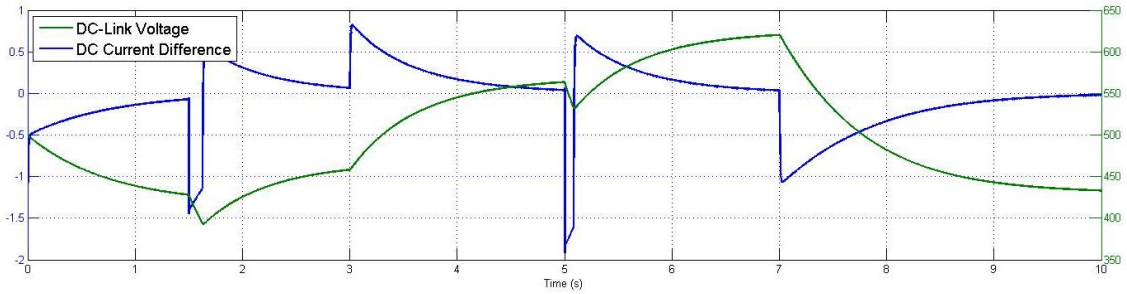

Figure 5.12: DC-Current Difference and Link Voltage

Based on the simulations carried out and the results presented, it can be concluded that the generator-side converter was proven to work as required.

5.5. Grid-Side Converter

The purpose of the grid-tied converter is to transfer energy from the DC-Link to the grid and maintain a stable DC-Link voltage. In a similar manner to the machine-side converter, the control is based around two inner current control loops which regulate the direct and quadrature current components independently. An outer control loop regulates the DC-Link voltage by modifying the direct current reference component

while the quadrature current can be used to regulate the reactive power transferred to the grid.

5.5.1. Current Control

The aforementioned current control loops are simulated by supplying the DC-Link from a constant DC-voltage source. The principle control scheme is shown in figure 5.13.

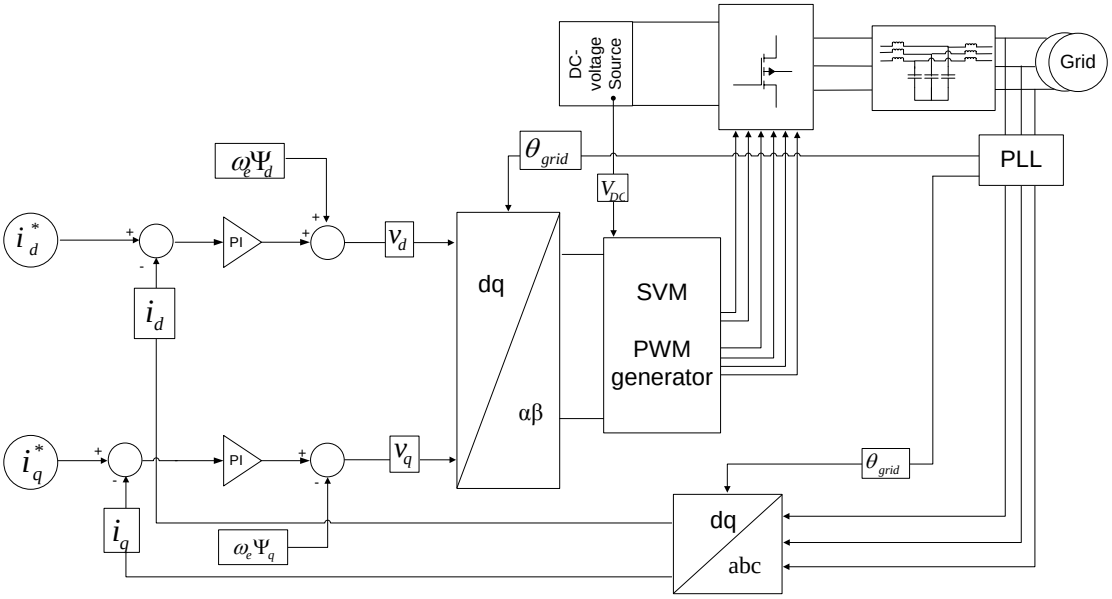

Figure 5.13: Gird-side current control scheme

Throughout the work carried out the quadrature current component is maintained at zero to minimise the reactive power transferred to the grid. A step input was applied to the direct current component and the resultant current flow to the grid measured. A plot of the dq-current responses is shown below.

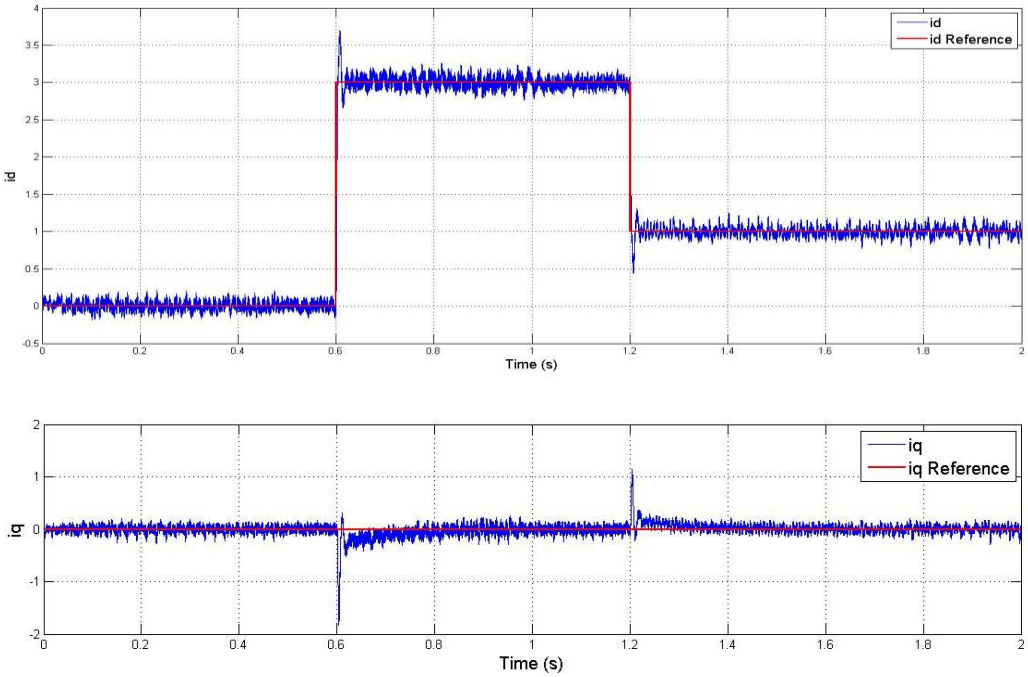

Figure 5.14: dq-axis current response

The response to a step input is very fast and shows little overshoot with some oscillation. This can be attributed to the PI-controller gains used, which were ascertained manually.

The resulting power transfer to the grid is shown in figure 5.15 below. From the graph is can be concluded that the real and reactive power can be controlled independently. No change in reactive power is observed when the real power is stepped up or down.

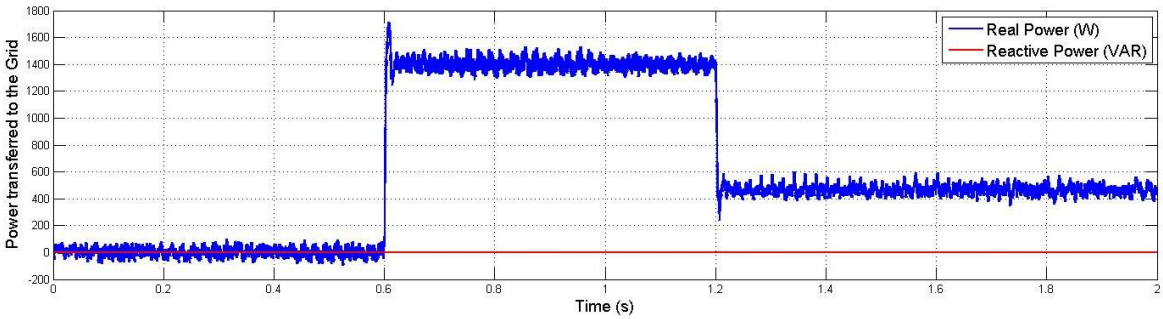

Figure 5.15: Power transferred to the Grid

The filter used in these simulations is a LCL-type filter and its parameters are the same as in the laboratory implementation discussed later on. The actual filter components were derived in chapter 3.4.

5.5.2. DC-Link Control

The purpose of the outer control loop is to regulate the DC-Link voltage, which varies due to the fluctuating current fed into the DC-Link from the generator. The grid-side converter measures the DC-voltage and the error between measured and reference DC-voltage, and determines d-axis current reference to the current controller, in order to vary the real power delivered to the grid, thereby regulating the DC-voltage. A schematic of the simulation is shown in figure 5.16.

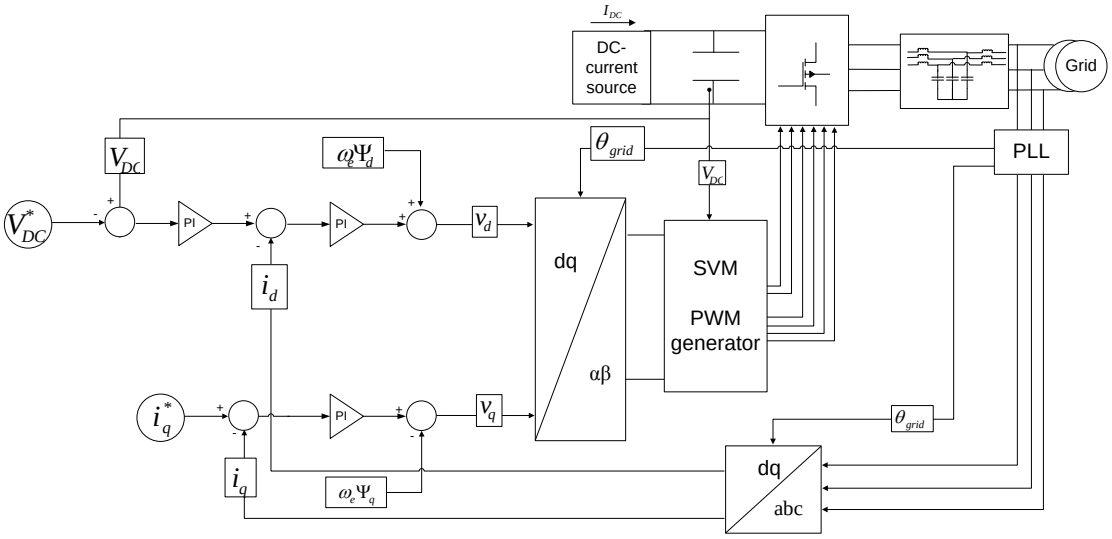

Figure 5.16: Grid-side DC-link control scheme

A programmable current source was placed as the input to the DC-Link and the voltage reference set to 750V. A step-change in DC-Link current represents the worst case scenario, as this does not occur in the final system. The applied DC-Link current is shown in figure 5.17 below.

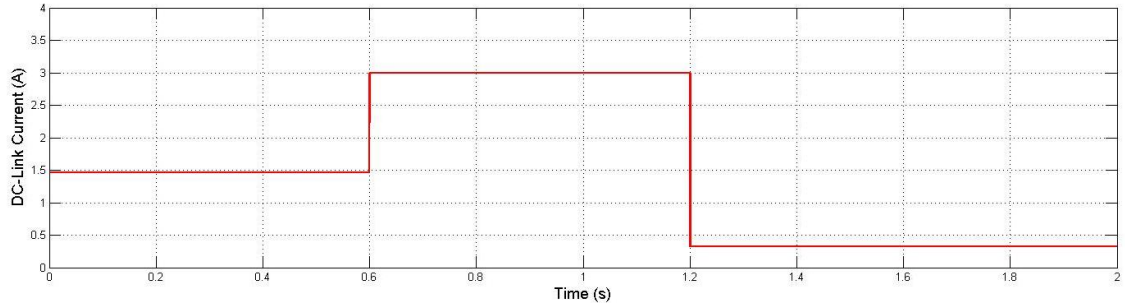

Figure 5.17: Input Current to the DC-Link

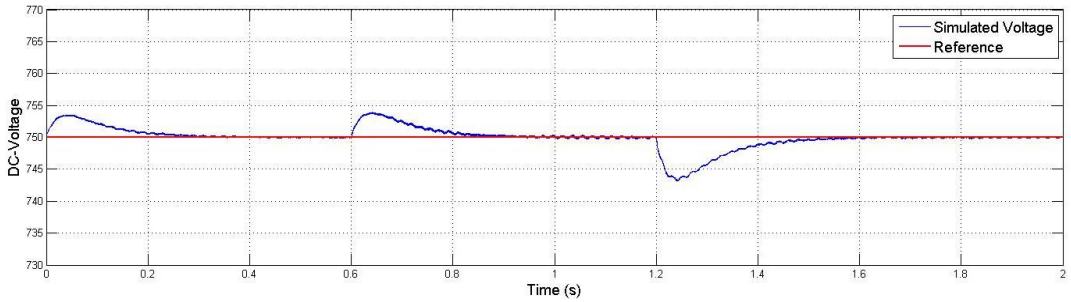

Figure 5.18: DC-Link Voltage

The simulation clearly shows how an increase in DC-Link Current on the Generator-Side results in an initial rise in DC-Voltage as illustrated in figure 5.18, at t=0 seconds and again at t=0.6 seconds. The outer control loop brings the DC-Link voltage back to its reference value by increasing the direct current component which is shown in figure 5.19. At t=1.2 seconds the input current to the DC-Link is reduced to 0.3A. A corresponding dip in DC-voltage is observed in figure 5.18. To counteract this, the d-axis current is reduced, shown in figure 5.19, thereby stabilising the DC-voltage. The quadrature reference current component is maintained at zero throughout, although a small change can be observed during the transient period, as shown in figure 5.20.

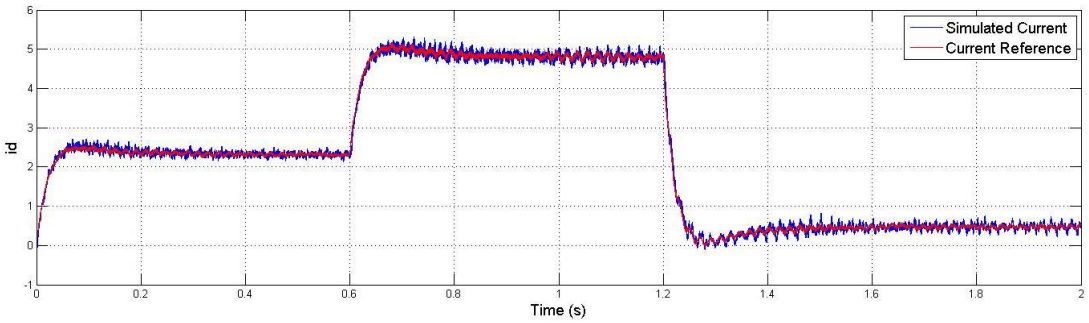

Figure 5.19: direct current component

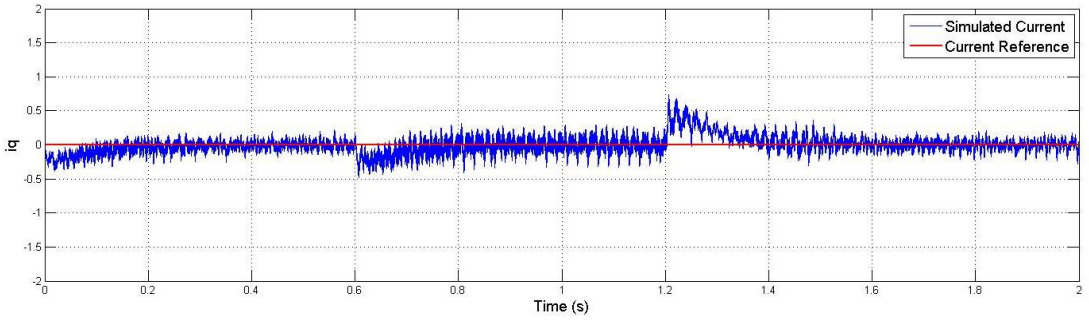

Figure 5.20: quadrature current component

The power transferred to the grid should be equal to the power in the DC-Link minus the losses incurred in the converter and filter. The DC-Power was calculated according to equation (5.5) and is shown in figure 5.21.

$$P_{DC} = V_{DC} \cdot I_{DC} \tag{5.5}$$

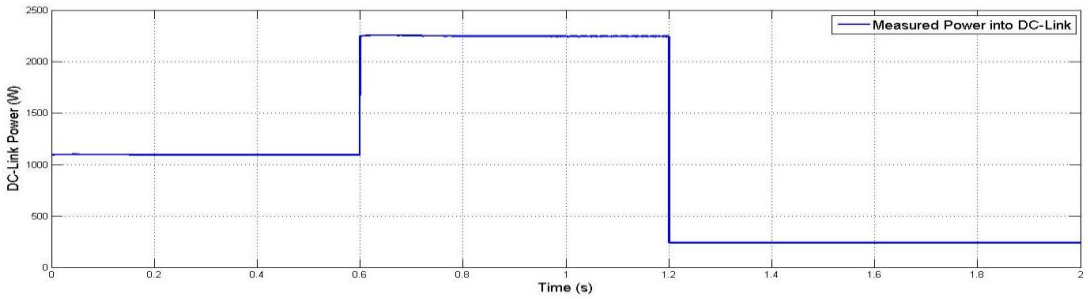

Figure 5.21: Power into DC-Link

The real and reactive power delivered to the grid is then calculated according to equation (5.6) and (5.7).

$$P = \frac{3}{2} \cdot v_{dg} \cdot i_{dg} \tag{5.6}$$

$$Q = \frac{3}{2} \cdot v_{qg} \cdot i_{qg} \tag{5.7}$$

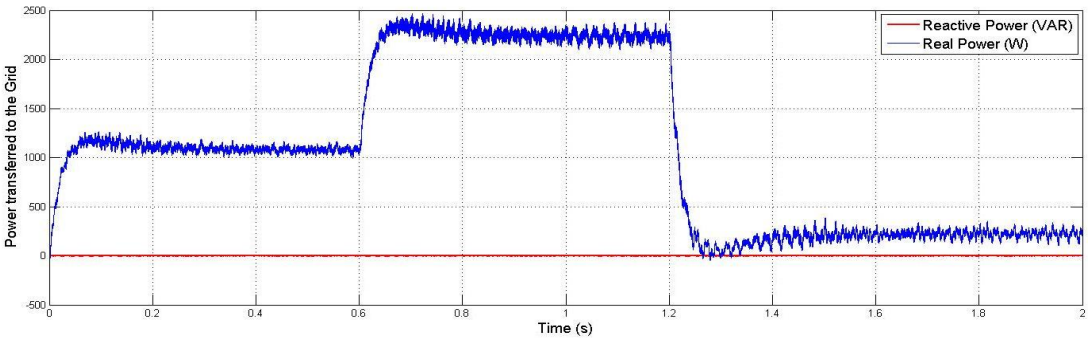

Figure 5.22: Reactive and Real Power transferred to the Grid

A graph of Real and Reactive Power transferred to the grid is shown in figure 5.22. The current ripple is caused by the PWM switching. In figure 5.23, the DC-Link power is overlaid with the real and reactive power transferred to the grid. The waveforms have been filtered to allow for a better comparison between real and reactive power transferred to the grid and DC-Link power.

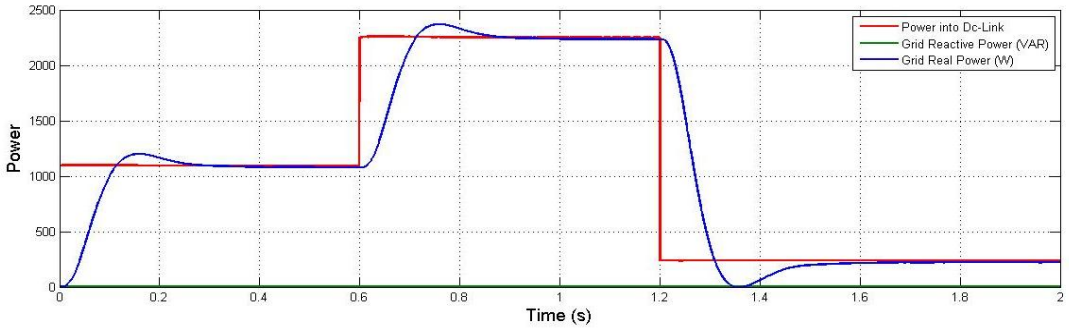

Figure 5.23: Grid and DC-Link Power

As expected, the DC-link power and Real Power transferred to the grid differ during the grid current transient periods, however they settle to the same value once steady-state has been reached.

5.6. Complete System Simulation

Once the individual components were simulated and shown to be working correctly the complete system, consisting of the wind turbine emulator, the generator as well as the power converters and their control were simulated. The sole input to the system is the wind speed in meters per second.

5.6.1. Complete System Response to a Step in Wind Speed

The system response to a step change in wind speed has been simulated and analysed in this section. The wind speed is stepped from 3.5m/s to 4m/s as shown in figure 5.24.

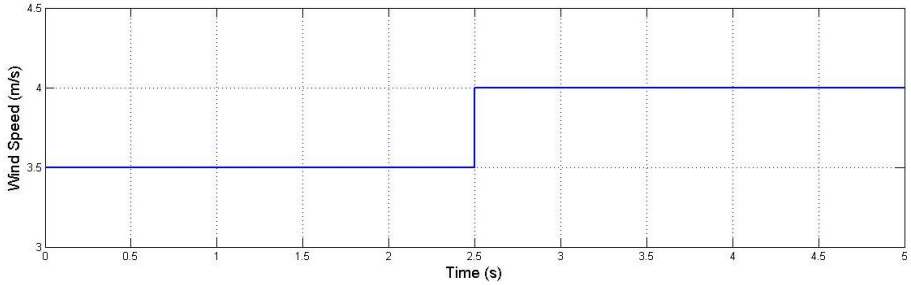

Figure 5.24: Wind speed step Input

In order to track the MPP, the controller adjusts the generator and therefore turbine speed accordingly. This is achieved by reducing the q-axis current component at

t=2.5seconds as shown in figure 5.25, thereby allowing the generator to accelerate to its desired speed.

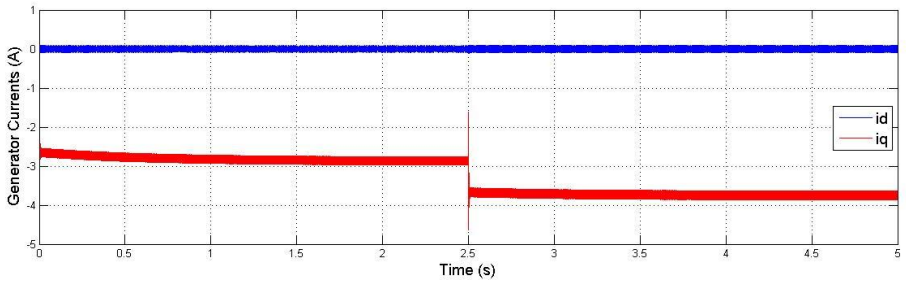

Figure 5.25: Generator current response to a step in wind speed

Figure 5.26 shows the speed response of the system. As expected the machine accelerates to the new MPP at t=2.5seconds. The acceleration appears instant due to the absence of inertia in the simulated system. There is some overshoot in the response and some settling time until the steady-state speed is reached.

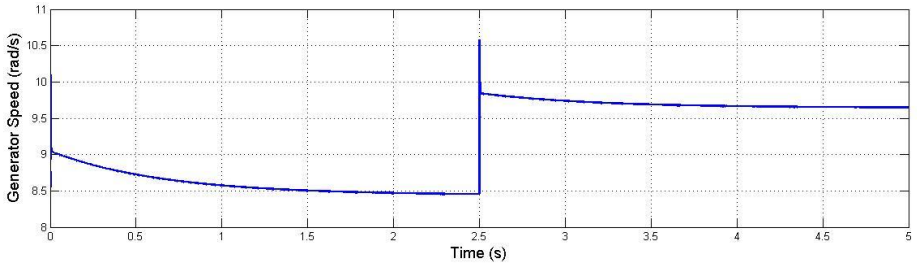

Figure 5.26: Generator speed response to a step in wind speed

Based on the wind speed and the turbine shaft speed, the power coefficient is calculated, as shown in figure 5.27 below.

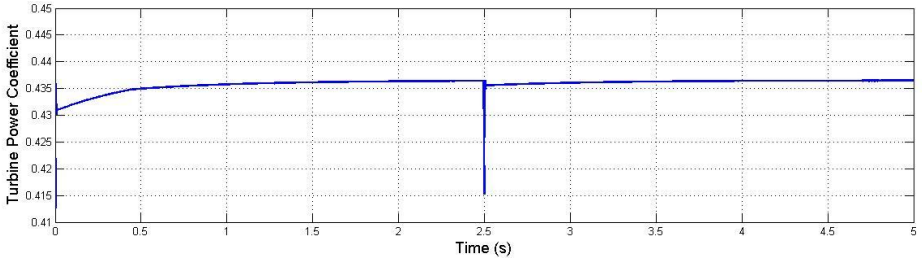

Figure 5.27: Turbine power coefficient response to a step in wind speed

During the transient period the power coefficient dips until the new optimum speed is reached. This is in accordance with equation (2.5), which describes the relationship between power coefficient and the optimum TSR. During the transient period the turbine speed differs from the MPP which results in a lower power coefficient.

The grid-side converter maintains the DC-link voltage by adjusting the d-axis component of the grid current, as shown in figure 5.28 below.

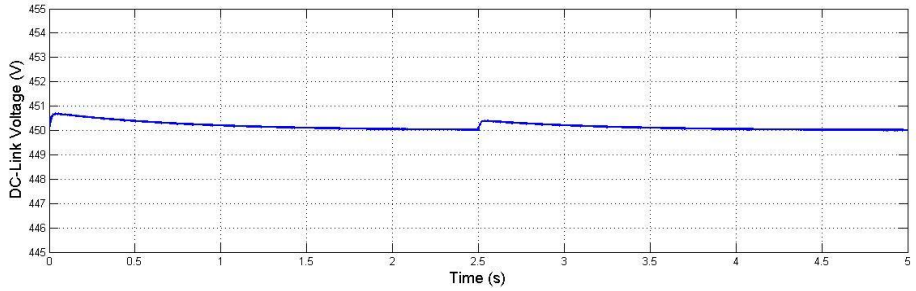

Figure 5.28: DC-link voltage

A small rise in DC-voltage, as shown in figure 5.28, occurs during the transient period before the grid-side controller compensates by increasing the d-axis current components. The corresponding grid current components are shown in figure 5.29 below.

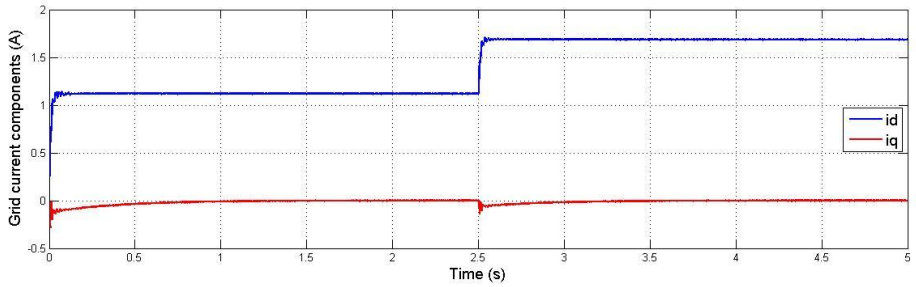

Figure 5.29: Grid current components

Based on equations (2.51) and (2.52), the real and reactive components of the power transferred to the grid are calculated as shown in figure 5.30.

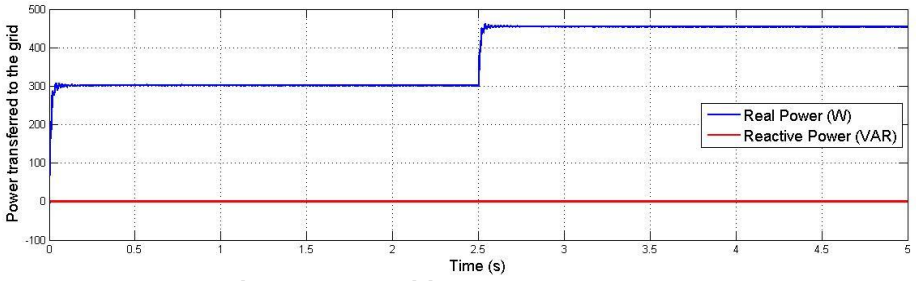

Figure 5.30: Grid power components

From the simulated system response as presented in this section it is concluded that the system has been simulated correctly. The absence of inertia and friction result in very fast response times. This needs to be considered when comparing the simulated results to values obtained experimentally.

5.6.2. Steady-State Performance of the complete System

The complete system was simulated over a time period of 5 seconds, while maintaining a constant wind speed. This demonstrated the performance of the system under steady-state conditions. In all simulations carried out the mechanical losses, namely friction and windage losses, have been ignored. However, the model of the friction and windage losses derived in section 6.1.2 was computed as a function of speed and subtracted from the simulated results. Under all three control strategies the system is simulated at wind speeds ranging from 4m/s to 7m/s at intervals of 0.5m/s while the relevant parameters were recorded.

In figure 5.31 and 5.32 the real power transferred to the grid at different wind speeds is shown.

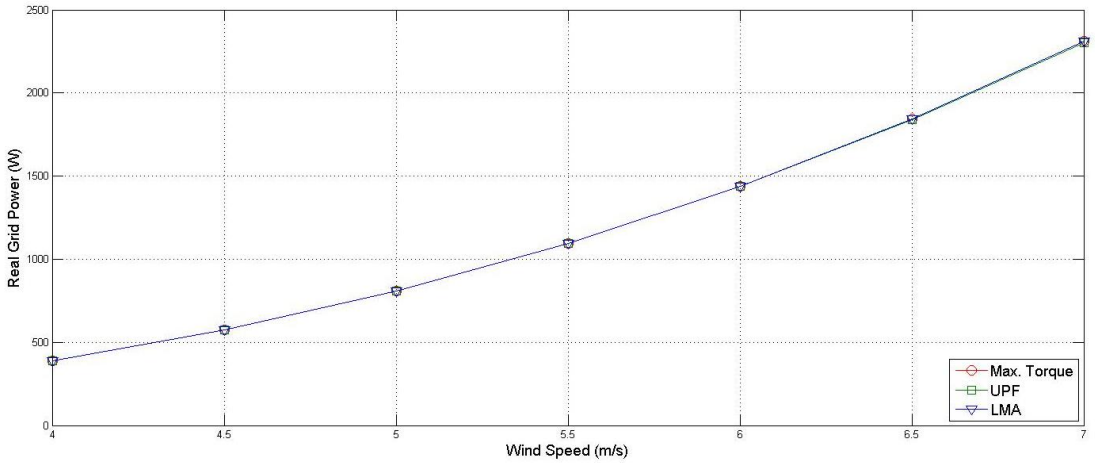

Figure 5.31: Real Grid Power as a function of wind speed

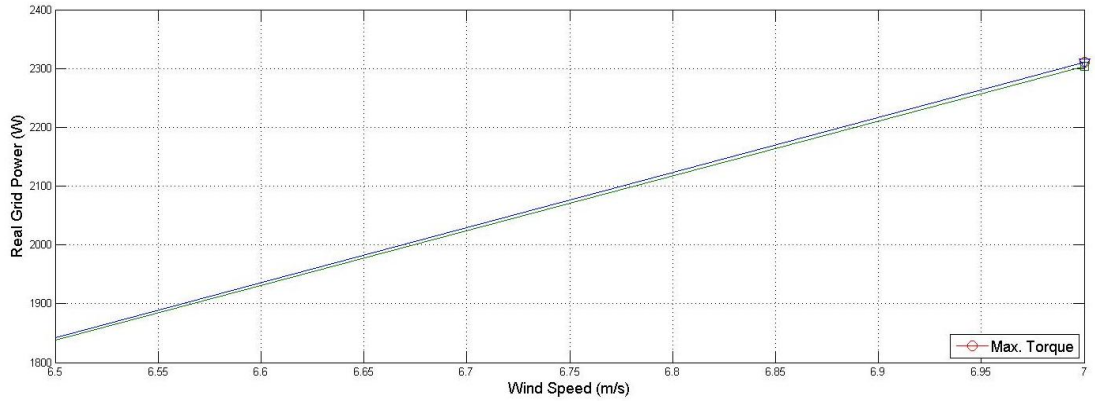

Figure 5.32: Real Grid Power as a function of wind speed (6.5m/s - 7m/s)

The real power transferred to the grid is nearly the same under all three control strategies as displayed in figure 5.31. However when the generator is operated at

maximum power factor (UPF control) the real power is less than under the maximum torque per current and LMA control, especially at higher wind speeds as shown in the enlarged graph, shown in figure 5.32. This is in accordance with the analytical results obtained in the previous chapter.

The overall efficiency of the system is calculated according to:

$$\eta_{system} = \frac{P_{grid}}{P_{turbine}} \cdot 100\% \qquad (5.8)$$

The wind turbine output under MPPT only depends on the turbine speed and the wind speed, and is therefore the same in all three control modes. The calculated system efficiency is shown in figure 5.33.

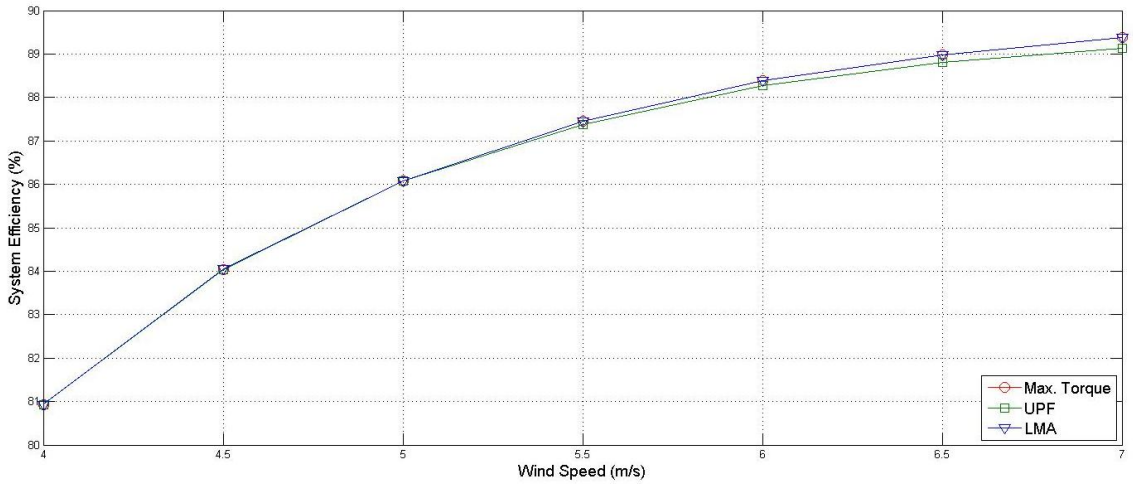

Figure 5.33: Simulated System Efficiency as a function of wind speed

The performance of the UPF control can be seen to deteriorate as the wind speed increases. Although the difference is small, it is evidently increasing with wind speed. The LMA and maximum torque per current control methods do not differ in the wind speed range investigated.

The exact numerical values obtained through the simulations are listed in Appendix B.

5.7. Conclusions

A thorough analysis was conducted in simulation of the 2 main sections of the system, the machine- and grid-side converter, independently. The complete system was integrated and simulated. From the simulated results it can be concluded that the system control was implemented correctly and that the system behaved as expected.

Chapter 6

Experimental Setup – hardware & software implementation

6.1. Introduction

In this chapter, the experimental implementation of the system in the laboratory is discussed. Furthermore, the process of obtaining relevant parameters of the various components is presented. Certain problems and limitations were encountered during the laboratory implementation. These are discussed together with the manner in which they were addressed and their impact on the results obtained.

6.2. Overview of Laboratory Setup and Components

A schematic overview of the experimental setup is provided in figure 6.1.

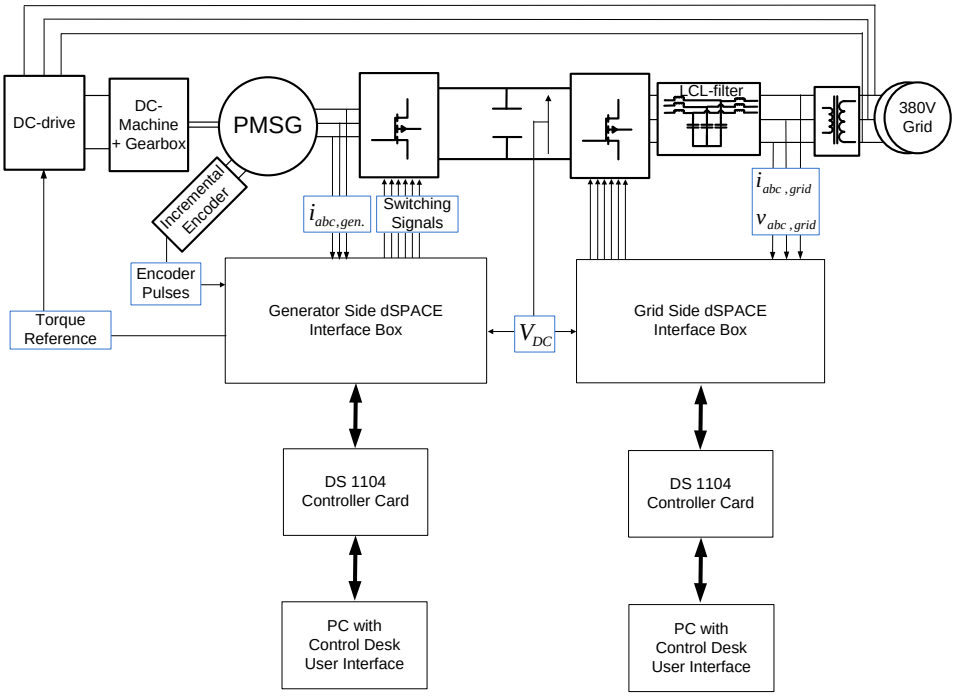

Figure 6.1: Schematic of the overall experimental setup

The system is implemented in the laboratory using a 6kW Scirocco E5.6-6 PMSG Generator. All control algorithms are implemented in MATALB/Simulink while two dSPACE kits provide the required real-time interfaces. Currents and voltages are measured through LEM modules, which reduce high voltages and currents to acceptable voltage. These signals are fed into the ADCs on the respective dSPACE kits. User-Interfaces are implemented in Control Desk on two PCs which are connected to the dSPACE interface through a DS1104 Controller Card. An incremental encoder is mounted on the generator shaft which provides the position and speed feedback. The back-to-back converter used is a 20kVA Semikron converter with a built-in DC-Link. The DC-Link capacitance is 4700uF. The turbine is emulated through a DC-motor operating in torque control mode, which is coupled to the generator through a 6:1 gearbox. The DC-motor is driven by a thyristor drive which receives its control signal from a DAC channel on the dSPACE kit. The complete setup in the laboratory is shown in figure 6.2 below.

Figure 6.2: Experimental Setup in the laboratory

6.3. Generator Parameter Estimation

The control of the machine requires knowledge of the relevant machine parameters, both for the DC-machine as well as the PMSG. How the relevant parameters were obtained and their values are presented in this section.

The permanent magnet excitation is established from the open terminal voltage of the generator. Under open-terminal condition no currents are flowing and the governing equations (2.12) and (2.13) are reduced to:

$$v_d = 0 \tag{6.1}$$

$$v_q = \omega_e \lambda_{pm} \tag{6.2}$$

Running the generator under these conditions and measuring the voltage is then used to obtain the permanent magnet excitation (λ_{pm}) according to:

$$\lambda_{pm} = \frac{v_q}{\omega_e} = \frac{v_q}{p \cdot \omega_m} \tag{6.3}$$

Figure 6.3 shows the recorded values for v_q at different speeds.

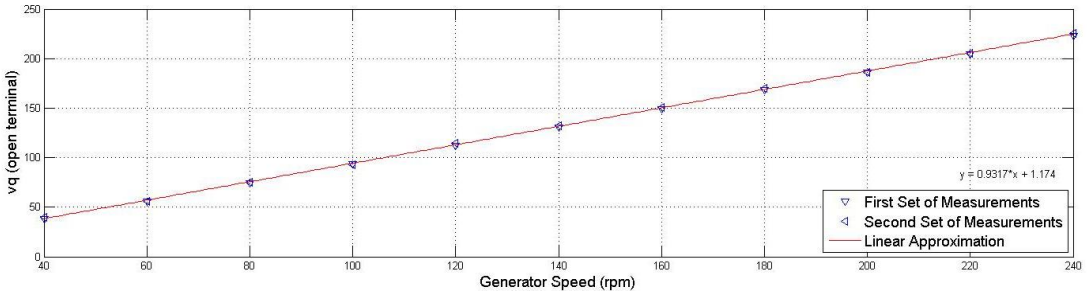

Figure 6.3: Generator Open Terminal Voltage vs. Speed

Substituting the linear approximation of v_q as a function of machine speed into equation (6.3) results in permanent magnet flux value of:

$$\lambda_{pm} = 0.74Wb$$

The stator d-axis and q-axis inductance of the PMSG are obtained according to the method described in [32]. Aligning the rotor with the relevant axis as shown in figure 6.4 (a) and (b) and then applying a voltage step while observing the current response yields two results, the stator resistance and time constant along the respective axis.

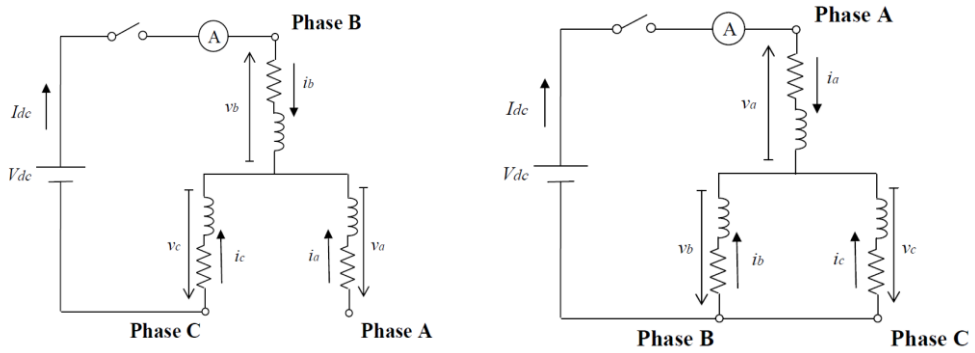

a) **b)**

Figure 6.4: Rotor alignment with d-axis (a) and q-axis (b)

The time constants τ_d and τ_q are the time it takes for the current to rise to 63% of its final value. By plotting the current response as a function of time, these values were obtained experimentally from the plots shown below.

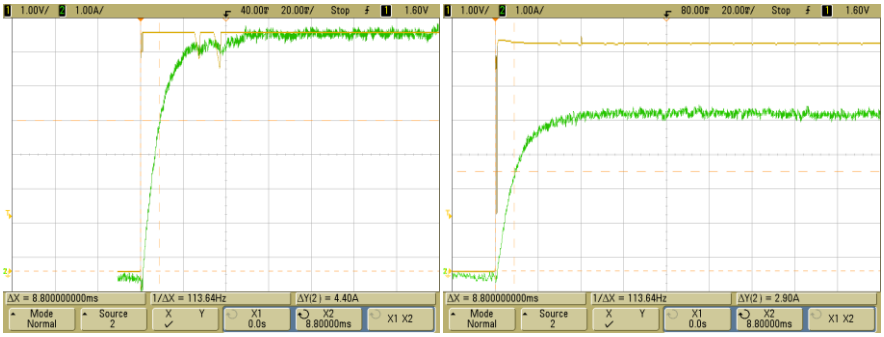

Figure 6.5: Current Response to a Voltage Step across the d and q axis

The stator resistance is calculated according to equation (6.4).

$$r_s = \frac{v_{d,final}}{i_{d,final}} \tag{6.4}$$

Where $v_d = \frac{2}{3}V_{DC}$ and $i_d = I_{DC}$

The stator resistance was found to be $r_s = 0.76\Omega$.

From the current responses in figure 6.5 the time constants are found.

$$\tau_d = 8.8ms \text{ and } \tau_q = 8.8ms$$

The stator inductances are calculated according to equation (6.5) and (6.6) below.

$$L_d = r_s \cdot \tau_d \tag{6.5}$$

$$L_q = r_s \cdot \tau_q \tag{6.6}$$

From equations above, the respective inductance values along the d-axis and q-axis are obtained.

$$L_d = 6.5mH \text{ and } L_q = 6.5mH$$

These results are expected since the machine is a surface-mounted permanent magnet machine which implies that the d- and q-axis inductance should be equal.

6.3.1. Estimating Core Losses as a function of Speed and Loading

For the loss minimisation control to effectively minimise the overall machine losses a model of the core losses as a function of generator speed and loading is required. Separating the core losses from friction and windage losses is difficult due to the presence of core losses under no-load conditions in a PM machine. The absence of a torque transducer further complicates this task as the mechanical shaft power had to be estimated based on the input to the DC-machine used for the turbine emulator.

The losses in the DC-machine were estimated as described here. It should be noted that the gear-box was treated as part of the DC-machine and its mechanical losses are included in the friction losses of the DC-machine. The DC-machine was decoupled from the generator and run under no-load conditions. It's no-load losses, which include friction, windage, copper and core losses were then measured as input power. All no-load losses were considered to be a function of speed.

The DC-machine used in the turbine emulator has the flowing parameters.

Table 6.1: DC-machine parameters

Rated Speed	Rated Power	Rated Voltage	Armature Resistance
1500rpm	3hp	220V	1.3Ω

The armature resistance is measured directly after running the machine under load to bring it up to operating temperature. As the machine is separately excited the copper losses in the field winding can be ignored.

The different loss components under no-load conditions are shown in figure 6.6.

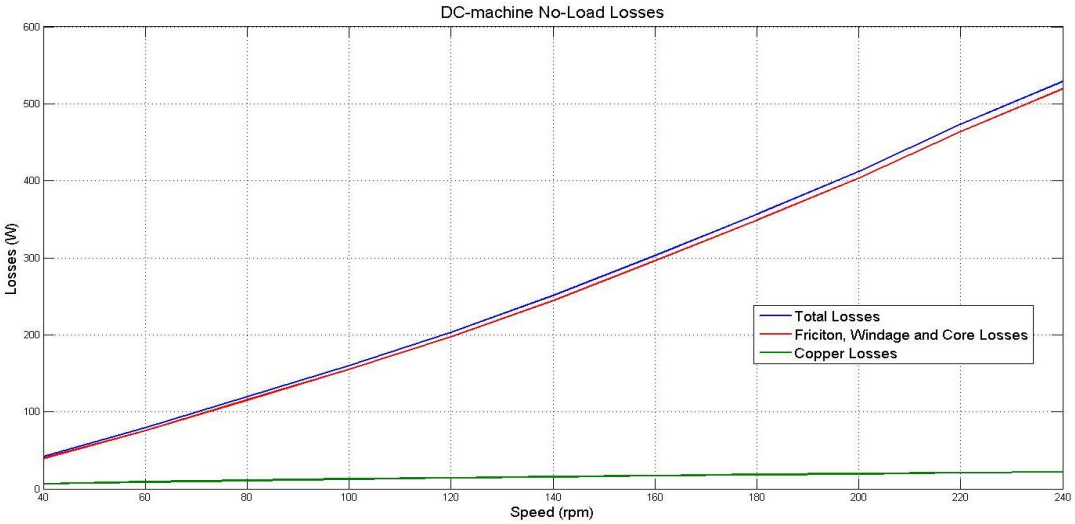

Figure 6.6: DC-machine losses at No-Load

By subtracting the copper losses under no-load conditions from the total losses the friction, windage and core losses were determined. Assuming the core losses to remain constant under loaded conditions, the friction and windage losses are extracted as a function of speed. From the recorded results a best-fit curve was found which is described by equation (6.7).

$$P_{rotational}\ (\omega) = 0.03314 \cdot \omega^2 + 13.75 \cdot \omega - 23.5W \qquad (6.7)$$

The derived polynomial for rotational losses as a function of speed does not comply with the theory of machines since it yields negative values at low speed. Theoretically the formula should not include any constant and be a purely quadratic function of speed. The losses were only investigated for speeds greater than 40rpm which is the likely cause for the error in equation (6.7). To remain consistent with the laboratory results, the offset in equation (6.7) was maintained, although it does not confirm with the theory.

The shaft power produced by the DC motor is estimated according to equation (6.8).

$$P_{shaft}\,(\omega, V_{dc}, I) = V_{dc} \cdot I_{dc} - P_{cu}(I_{dc}) - P_{rotational}\ (\omega) \qquad (6.8)$$

By coupling the generator to the DC-machine and running it on open circuit, the no-load losses of the generator are established. These losses include friction, windage and core losses due to the permanent magnet excitation as shown in figure 6.7.

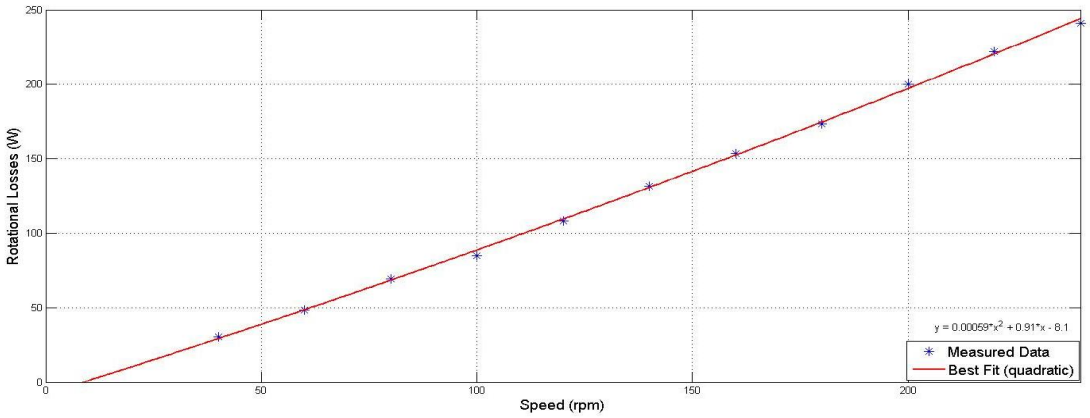

Figure 6.7: Rotational Losses in the PMSG under no-load

The core losses of the PMSG can be approximated by equation (6.9).

$$P_{core}(f,B) \approx K_c(f) \cdot \lambda_s^2 \approx K_c(f) \cdot \left(\left(\lambda_{pm} - L_s i_d\right)^2 + \left(-L_s i_q\right)^2\right) \qquad (6.9)$$

Under no-load conditions the core losses are purely a function of the flux established by the permanent magnets, λ_{pm}, and can be expressed by equation (6.10).

$$P_{core,no-load}(f,B) \approx K_c(f) \cdot \lambda_s^2 \approx K_c(f) \cdot \lambda_{pm}^2 \qquad (6.10)$$

To establish the core loss constant $K_c(f)$, a function is fit to the no-load core loss data. The effect of loading on the core losses is included in the model. For this, the machine is loaded with a resistive load and the power dissipated is measured. By subtracting the power in the resistive load as well as the copper and no-load core losses from the shaft power, the increased core losses due to loading were found. This is used to establish the core losses as a function of speed and loading. Mathematically this can be expressed by equation (6.11).

$$\Delta P_{core}(f,\Delta B) \approx K_c(f) \cdot \Delta\lambda_s(\Delta i_s) \qquad (6.11)$$

Loading the PMSG with a purely resistive load results in operation at unity power factor. From [31], the relationship between i_d, i_q and total stator current i_s is defined by equations (6.12) and (6.13).

$$i_d = \frac{L_s}{\lambda_{pm}} \cdot 2i_s^2 \qquad (6.12)$$

$$i_q = \sqrt{\frac{\lambda_{pm}}{L_s} i_d - i_d^2} \qquad (6.13)$$

Substituting equation (6.12) into (6.13) yields the quadrature component as a function of total stator function according to equation (6.14).

$$i_q = \sqrt{2 \cdot i_s - (\frac{L_s}{\lambda_{pm}} \cdot 2i_s)^2} \tag{6.14}$$

Substituting equations (6.12) and (6.14) into equation (6.9) results in equation (6.15), expressing the core losses as a function of total stator current and speed.

$$P_{core\,,unity\ \ PF}(f,B) \approx$$
$$K_c(f) \cdot \left(\left(\lambda_{pm} - \frac{L_s^2}{\lambda_{pm}} \cdot 2i_s^2 \right)^2 + \left(-L_s \sqrt{2 \cdot i_s - \left(\frac{L_s}{\lambda_{pm}} \cdot 2i_s \right)^2} \right)^2 \right) \tag{6.15}$$

Hence:

$$K_c(f) \approx \frac{\Delta P_{core}\ (f,B)}{\left(\lambda_{pm} - \frac{L_s^2}{\lambda_{pm}} \cdot 2(\Delta i_s)^2 \right)^2 + \left(-L_s \sqrt{2 \cdot \Delta i_s - (\frac{L_s}{\lambda_{pm}} \cdot 2\Delta i_s)^2} \right)^2} \tag{6.16}$$

Measurements of stator current and speed under load and no load conditions were taken and substituted into this formula to establish the equation for $K_c(f)$:

$$K_c(f) = 0.01346 \cdot \omega^2 + 1.585 \cdot \omega \tag{6.17}$$

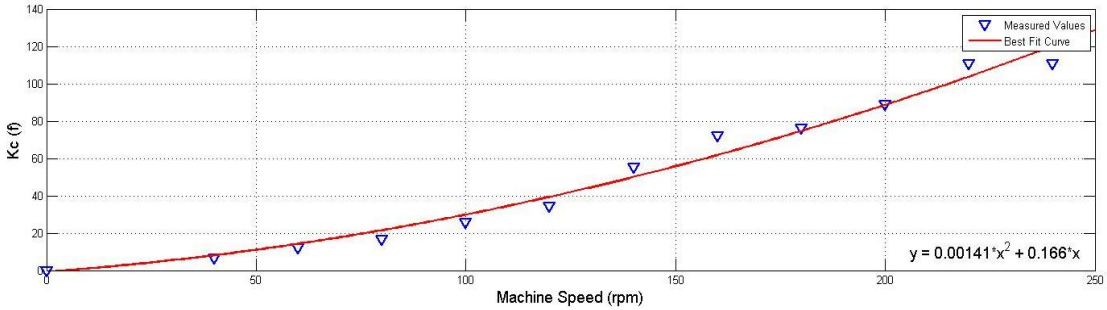

Figure 6.8: Core Loss Constant vs. Machine Speed

Based on these results the core losses under load-conditions can be approximated as a function of stator currents and speed to be:

$$P_{core}\left(\omega, i_d, i_q\right) \approx K_c(f) \cdot \left(\left(\lambda_{pm} - L_s i_d \right)^2 + \left(-L_s i_q \right)^2 \right) \tag{6.18}$$

This equation forms part of the basis for the loss minimisation control described in chapter 3.3.3.

It has to be noted that several assumptions were made in order to obtain these results. Firstly, the mechanical power on the shaft was estimated from the electrical input power to the DC-machine minus rotational and copper losses. This was necessary due to the absence of a torque transducer. Furthermore the mechanical losses, attributed to the coupling between the gearbox and the generator were assumed to be zero. The impact of temperature on the machine impedance as well as the operation of the gearbox has been omitted.

6.4. Wind Turbine Emulator

To emulate the behaviour of a wind turbine, a DC-motor was operated in torque control mode. A 3hp DC-motor was used in combination with a 6:1 gearbox to allow for low speed operation as required by the generator. The speed measurement was obtained from the position encoder by differentiating the position measurement. A schematic overview of the turbine emulator and its components is provided in figure 6.9.

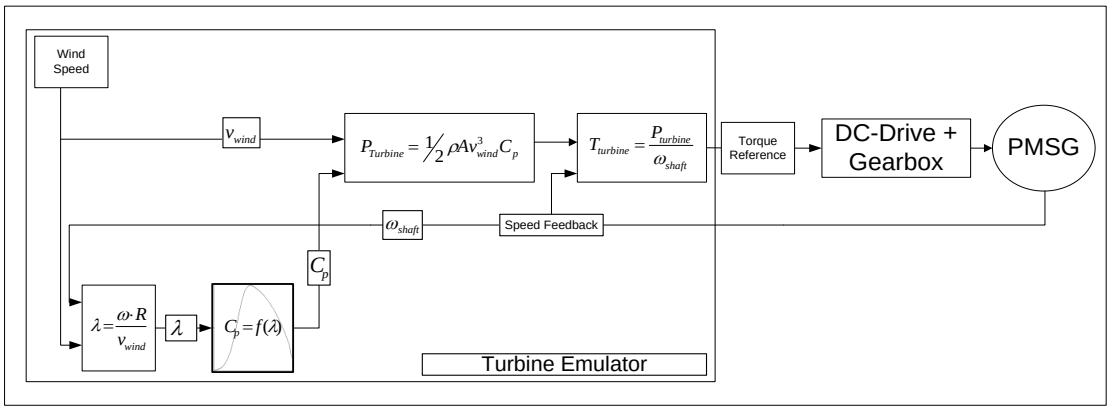

Figure 6.9: Turbine Emulator (Diagram)

As can be seen from the diagram in figure 6.9, the turbine emulator only requires the generator speed and the wind speed as an input. Since a fixed blade turbine configuration is investigated, the blade angle is constant at all times and therefore does not impact on the performance.

The DC-drive is shown in figure 6.10.

Figure 6.10: DC-thyristor drive

In torque control mode, the resulting torque from the DC-motor is proportional to the applied control voltage to the drive. A series of tests were conducted to establish the relationship between voltage and torque. The DC-machine was loaded and the developed power measured according to equation (6.8). The shaft torque was then calculated according to equation (6.19).

$$T_{shaft} = \frac{Pshaft\,(\omega, V_{DC}, I_{DC})}{\omega} \tag{6.19}$$

The relationship between applied voltage and resulting torque was found to in this was and is shown in figure 6.11.

This relationship is linear, and a best-fit straight line can be expressed as:

$$T(V) = -149.9v + 6.14Nm \tag{6.20}$$

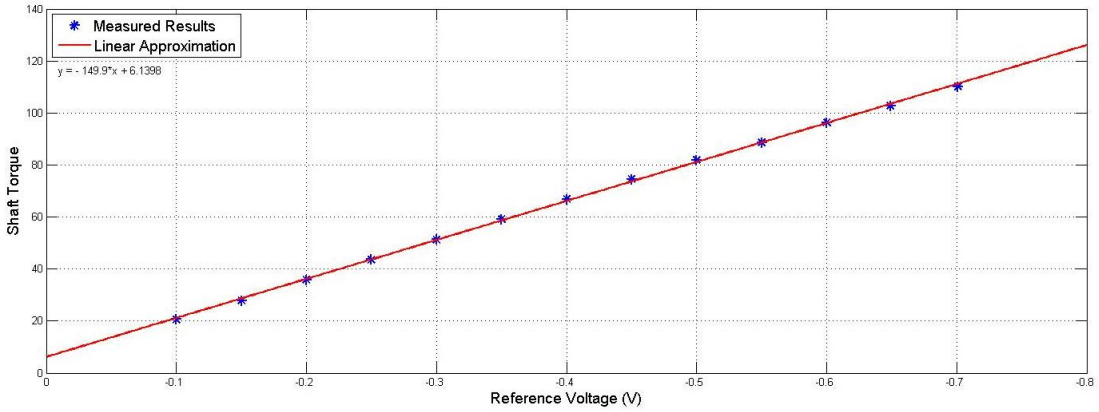

Figure 6.11: Torque vs. Reference Voltage

The relationship between applied voltage to the DC-drive and the developed torque, expressed in equation (6.20) is assumed to hold throughout the experimental implementation. To verify the correct operation of the emulator, it was coupled to the generator which was loaded to different operating points by means of a variable resistive load. The wind speed was set to different values and measurements of the electrical power dissipated in the resistive load were taken. The reason for the wind speed being limited to 6.5m/s is that the DC-machine used to emulate the turbine was limited to 3hp (2.23kW).

The mechanical shaft power was calculated from the measurements and is displayed in figure 6.12 below.

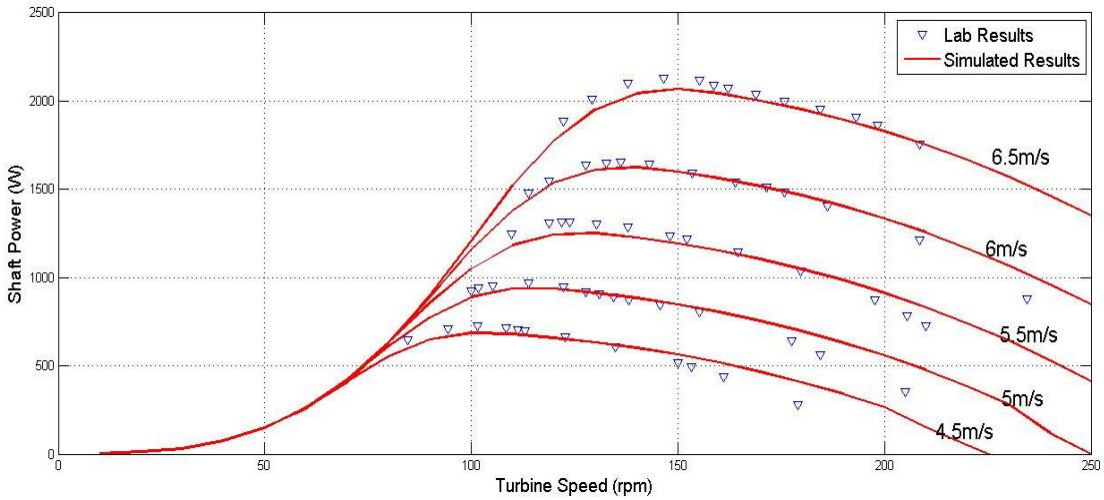

Figure 6.12: Mechanical Shaft Power

The difference between the laboratory and simulated results can be attributed to numerous factors. These include, assuming the core losses of the DC motor to be constant under no-load and load conditions will contribute to the error as well as the assumption that resistance in the machine remains constant. Changes in operating

temperature will change the winding resistance which impacts on the total losses in the machine. As can be seen from the graph in figure 6.12 the error is small enough to be considered negligible for the purpose of this thesis.

The power coefficient of the turbine was calculated from the measured power and compared to the curve from the manufacturer. This is shown in figure 6.13.

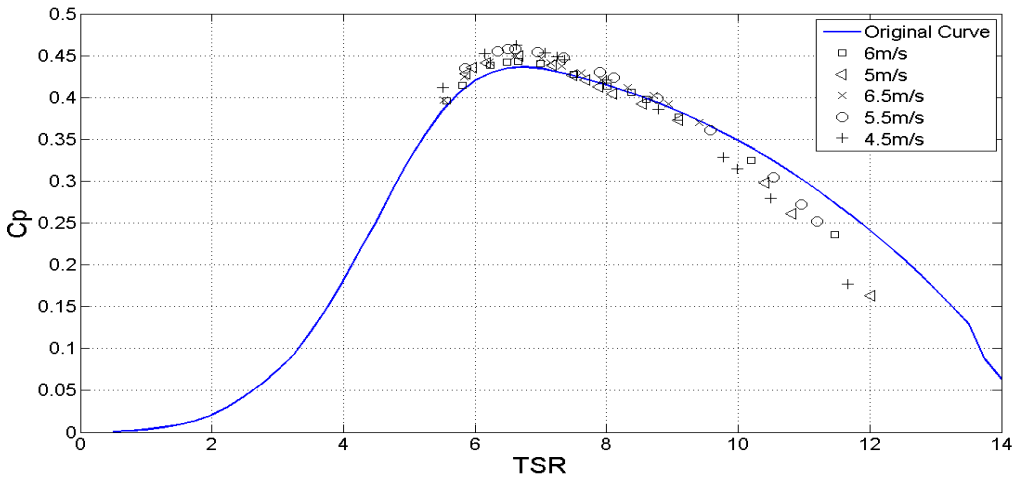

Figure 6.13: Cp vs. TSR (Lab Results and Original curve)

It can be seen that the power coefficient curve exhibits a similar error as the power curves in figure 6.12 which it is based on.

6.5. Machine-Side Controller Implementation

The machine side converter and its control are implemented on a dedicated dSPACE kit. The rotor position is measured by means of an incremental encoder with a resolution of 5000 pulses per revolution. The encoder is of the Type Sendix incremental Type 5000 made by KÜBLER. Figure 6.14 shows the PMSG mounted in the laboratory together with the incremental encoder.

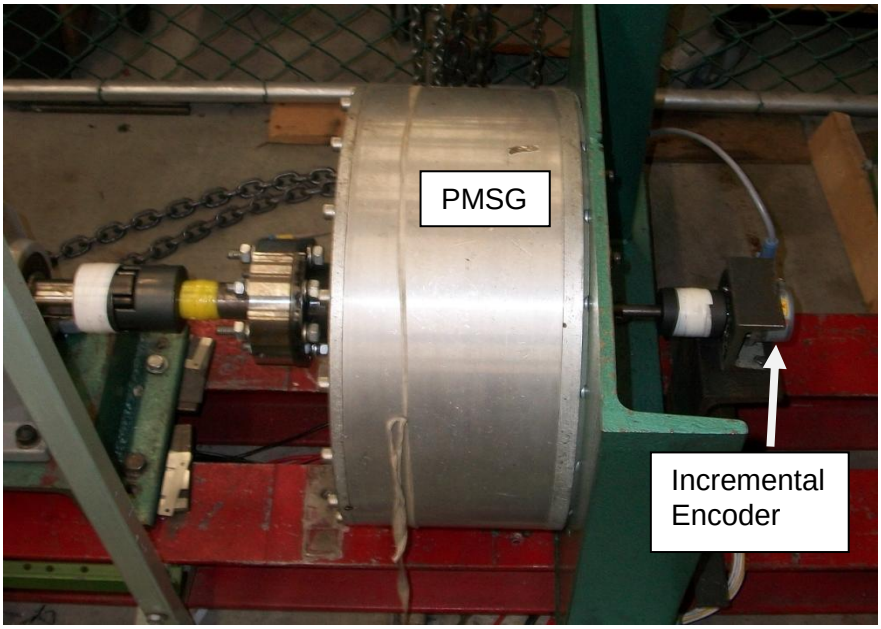

Figure 6.14: PMSG and the incremental encoder in the laboratory

Using the Incremental Encoder Interface on the DS1004 the rotor position is measured with a resolution of:

$$\Delta\Theta = \frac{360°}{5000} = 0.072° \tag{6.18}$$

During setup, the rotor was aligned with the d-axis and the encoder mounted such that its position is reset to 0 every time it passes this position. In this way the encoder position signal is equivalent to the mechanical rotor position. Multiplying this position by the number of pole pairs (p=12) yields the machines electrical position with respect to its d-axis.

$$\theta_e = p \cdot \theta_m \tag{6.19}$$

The current control of the generator-side converter is implemented according to the theory presented in section 2.8. To allow for independent control of the d- and q-axis, the cross-coupling components are compensated for according to equations (2.18) and (2.19). Figure 6.15 shows the schematic overview of the machine side control, excluding the outer speed loop.

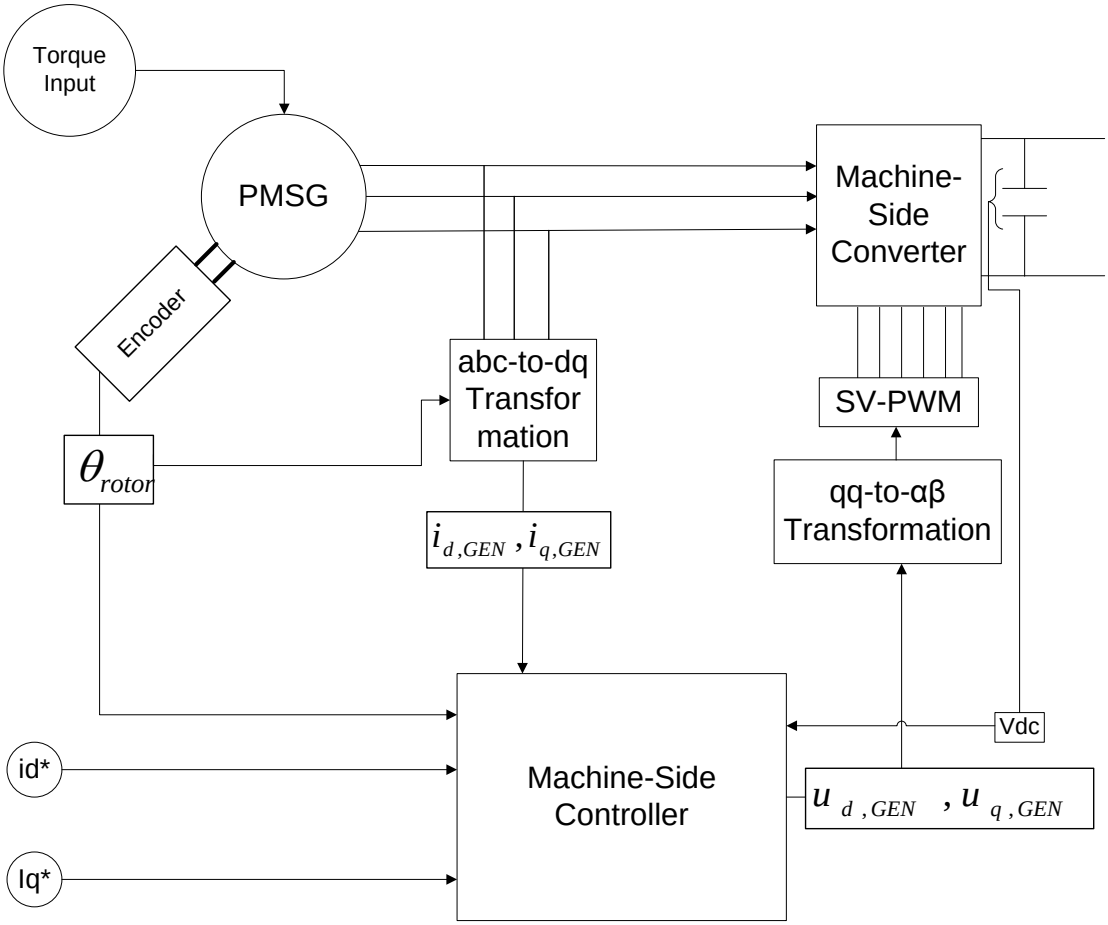

Figure 6.15: Generator-Side Current-control Scheme

A reference value for the torque producing component of the stator current (i_q) is obtained from an outer control loop which regulates the machine's speed. The magnetising current component (i_d) is regulated independently according to the control strategy applied. The complete system schematic is shown in figure 6.19.

6.6. Grid-Side Controller Implementation

To connect the system to the 3-Phase grid in the laboratory the phase voltage is reduced from 380V to 220V by means of a variable transformer. The grid filter was designed with 6 inductors and 6 capacitors as described in section 3.2.2. The control is implemented on a separate dSPACE kit and PC. The control scheme is shown figure 6.16.

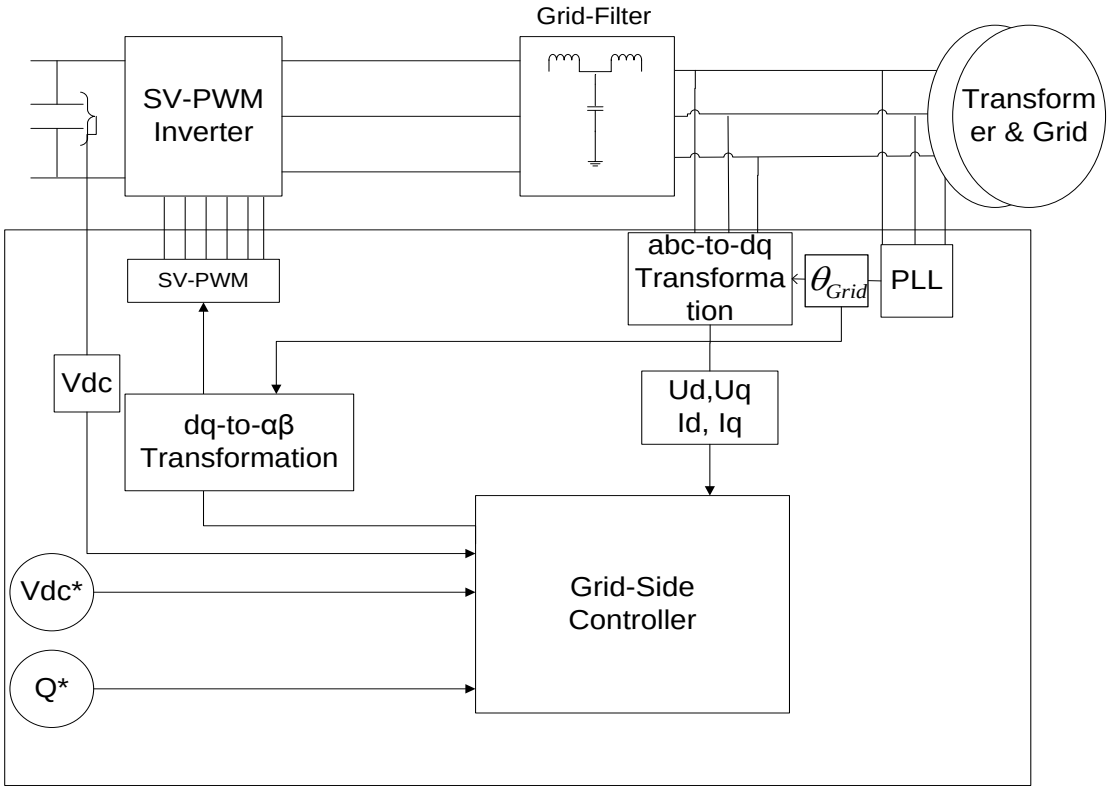

Figure 6.16: Grid-Side Converter Schematic

To effectively control the power flow to the grid, the exact phase angle of the grid voltage is required. Phase A of the grid voltage is aligned with the d-axis in the dq frame and forms the reference angel for all transforms. A LEM module reduces the grid voltage to acceptable levels for the ADCs where it is digitised. A software PLL is used to extract the phase angle of phase A.

The grid currents are measured through a current LEM which converts the currents into voltage signals. These are then digitised through the dSPACE's ADC channels before being transformed to the dq-reference frame.

The various transforms used have been presented in section 3.1. They are based on the same formulae as the transformations on the machine side, but the reference angle is obtained differently as discussed above.

The current flow to the grid is governed by equations (2.49) and (2.550). To simplify the control, only the inductive components of the grid-filter have been considered in the control implementation.

The real and reactive power flowing to the grid is calculated according to equations (2.51) and (2.52).

Throughout this thesis the reactive power flow to the grid is kept to zero and forms the set-point for Q^* as shown in figure 6.16. This implies that the q-axis current component remains zero. The DC-Voltage is set to 400V thereby forming the second input to the grid side controller.

The power converter used in this thesis is shown in figure 6.17.

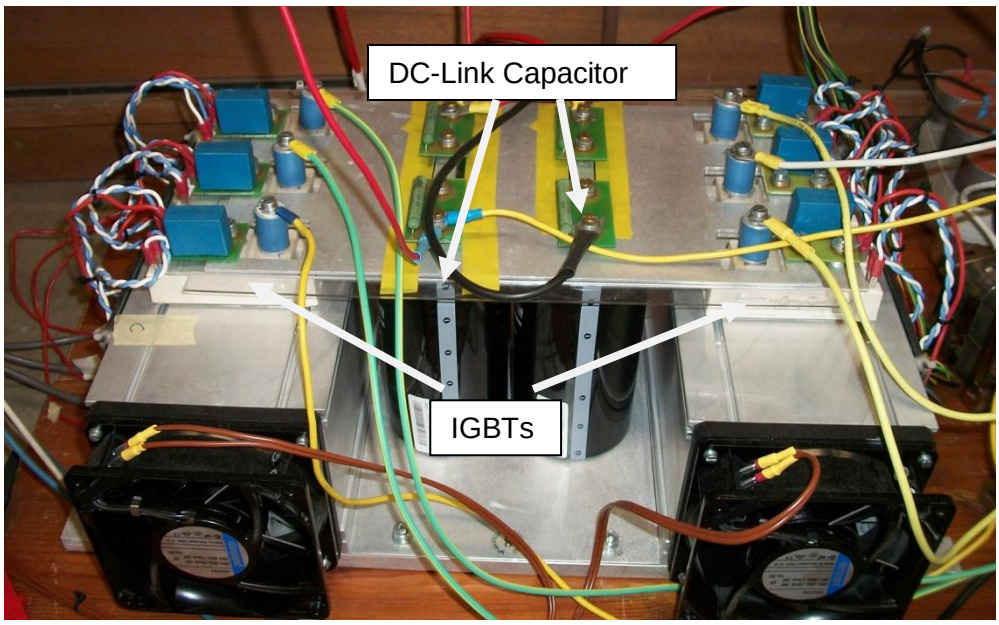

Figure 6.17: Power Converter in the laboratory

The LCL-type grid-filter was implemented according to the values derived in section 3.4.1 and 3.4.2. The required capacitance ($5uF$) was obtained by connecting two capacitors ($10uF$) in series while the grid-side inductance is made up of two inductors. The grid-filter used in the laboratory is shown in figure 6.18 together with the power electronic converters and step-down transformer.

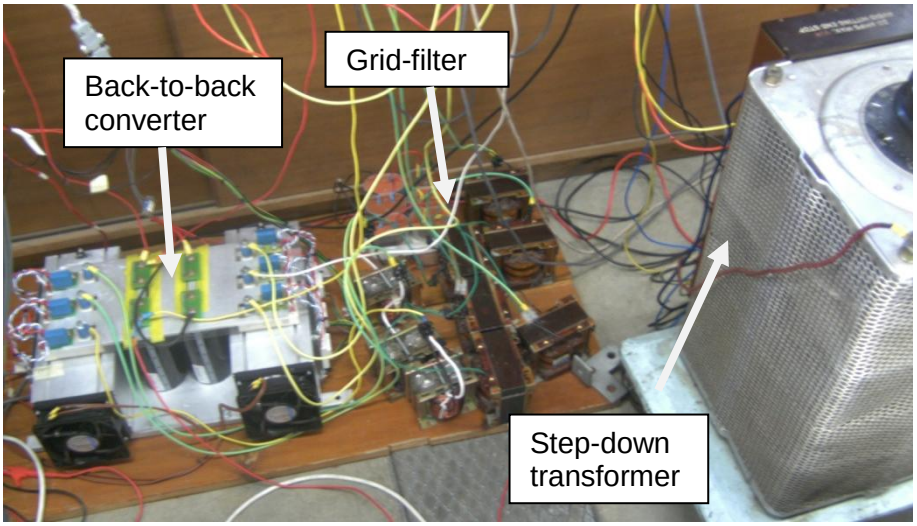

Figure 6.18: LCL-type grid filter and step-down transformer

6.7. Experimental Implementation of the complete system

A schematic of the complete experimental setup in the laboratory is shown in figure 6.19. The turbine emulator as well as the generator control is implemented on one dSPACE kit. The grid side control is implemented on a separate dSPACE kit. The use of two separate dSPACE kits is necessary due to the limited number of ADC channels (8 each) in one kit. Furthermore, each dSPACE only provides 9 SV-PWM ports and hence can only control one converter with SV-PWM switching.

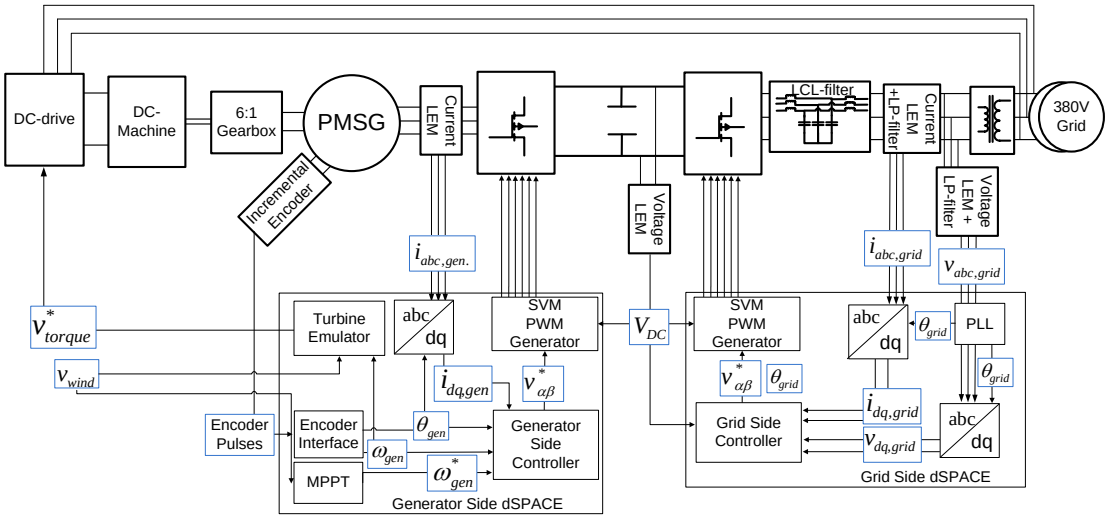

Figure 6.19: Complete schematic of the experimental setup

One major obstacle encountered during the implementation of the system is the accurate conversion of the relevant voltage and current waveforms. Due to the high

frequency noise induced by the PWM and the electromagnetic noise generated by the thyristor drive it is necessary to filter the captured waveforms before sampling them through the ADCs. This is achieved through a RC-type Low-Pass filter. The filter was designed to have a cut-off frequency of ten times that of the fundamental frequency of the relevant signal. A variable resistor was used for the resistive component of the filter. This allows for manual fine-tuning. Filters are mounted within the LEMs as shown in figure 6.20.

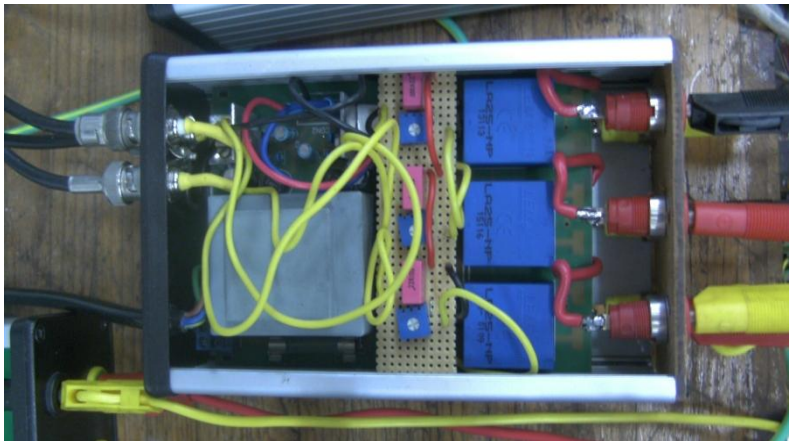

Figure 6.20: Current LEM module with RC-filter

The cut-off frequency of the LP-filter is calculated according to:

$$f_c = \frac{1}{2\pi RC} \tag{6.20}$$

Where R and C are the resistor and capacitor value respectively.

For all voltages and currents measured, the cut-off frequency is set to $f_c = 500Hz$ which is ten times their fundamental. From the LEM data sheet the maximum output current is found to be 25mA which together with the voltage range imposes a lower limit on the resistor value, according to:

$$R_{min} = \frac{\Delta V_{max}}{I_{max}} = \frac{20V}{25mA} = 800\Omega \tag{6.21}$$

To allow for the cut-off frequency to be adjusted within a wide range around the assumed cut-off frequency of 500Hz, a value of 2.5kΩ is assumed for the filter resistance during the calculation of the capacitance. The capacitance value is calculated according to:

$$C = \frac{1}{2\pi R f_c} = \frac{1}{2\pi \cdot 2500 \cdot 500} = 127.3nF \quad (6.22)$$

The next closest capacitance value available is 220nF. The variable resistance easily compensates for the increase in capacitance by reducing the resistance value.

The filters were manually fine-tuned by adjusting the resistance while feeding in a 50Hz signal within the range of applicable frequencies.

Filtering the relevant signals before feeding them to the ADCs significantly reduces the magnitude of the high-frequency noise in the captured signals. Another importance aspect is the correct grounding and earth connection of the relevant components. It is found that the DS1104 dSPACE kit does internally connect the ground signal to earth instead of providing a floating ground. To counter the impact of noise introduced through any earth loops, every component is grounded and all ground signals were connected to a single earth bar as shown in figure 6.21.

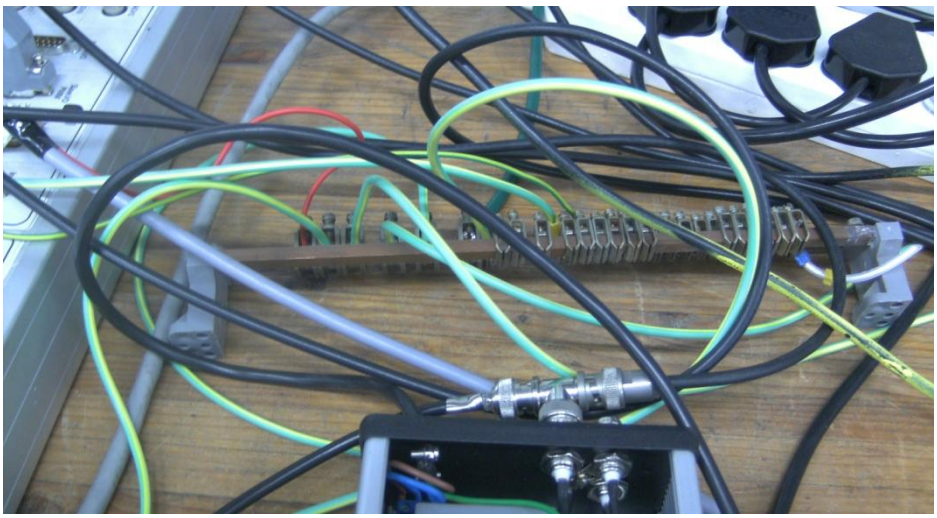

Figure 6.21: Common ground and earth bar

Connecting all ground terminals to earth through the earth terminal shown above is found to further improve the signal quality.

The user interface to control the system is provided by the Control Desk. It allows for real-time modification of applicable parameters as well as the capturing of variables.

6.8. Conclusions

A complete WECS was implemented in the laboratory. The turbine emulator was constructed using a DC-motor operated in torque control mode and coupled to the generator through a gearbox. Machine- and grid-side converters are fully controllable and operated through SV-PWM switching. The relevant operating parameters are captured and digitised through the dSPACE interface. The control of the generator as well as the grid connection is implemented on two PCs interface to the system through the dSPACE kits. A grid-filter was designed and constructed to provide the connection to the grid, while the grid-voltage was reduced through a step-down transformer. The system was tested and the relevant results are presented and discussed in chapter 7.

Chapter 7

Experimental Results and Discussion

7.1. Introduction

In this chapter the experimental results are presented and discussed. Initially the generator and its control were tested independently, in open- and closed loop for motor and generator mode. Furthermore, the correct operation of the turbine emulator is confirmed experimentally. Finally, the results attained from the steady-state operation of the complete system are presented and discussed. The applicable comparisons to analytical and simulated results are also discussed.

7.2. Motor Mode Operation

In this section the operation of the PM machine in motor mode is presented. This was done to validate the correct operation of the generator side converter and its control.

7.2.1. Open-Loop Operation

The machine is initially operated under no-load conditions in motor mode without any speed or current feedback. Varying the quadrature voltage component (v_q) while maintaining the direct axis component (v_d) at zero results in the open-loop characteristic shown in figure 7.1.

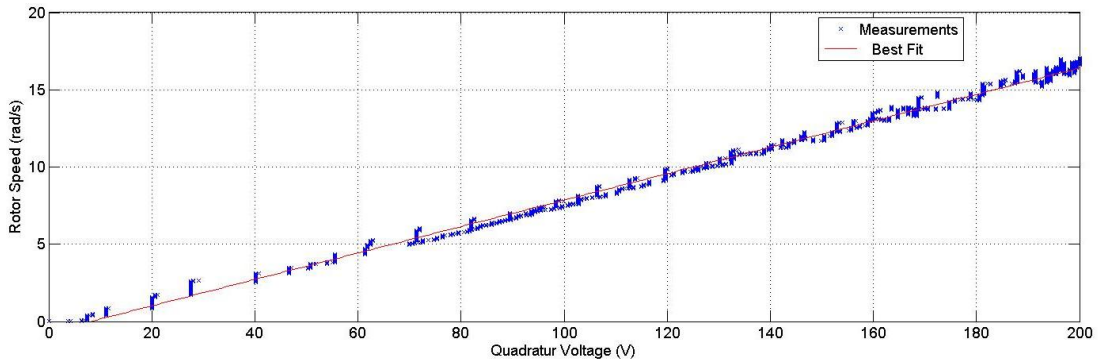

Figure 7.1: Speed vs. Quadrature voltage

From the governing equations (2.12) and (2.13) for a PM machine, the following assumption can be made: Under no-load conditions, the d- and q-axis current components are small and hence the relationship between quadrature voltage and machine speed is expected to be almost linear. This behaviour is observed experimentally as presented in figure 7.1.

7.2.2. Speed Control Mode

To implement effective MPPT, a good speed response is required to track the MPP. This behaviour is validated by applying a step-input to the speed control loop of the machine side controller while the machine is operated in motor-mode. The machine is loaded through the gearbox and the DC-machine, which is operated as a generator in this scenario. Throughout this section the d-axis current component is maintained at zero. The step-input to speed and its response is shown in figure 7.2.

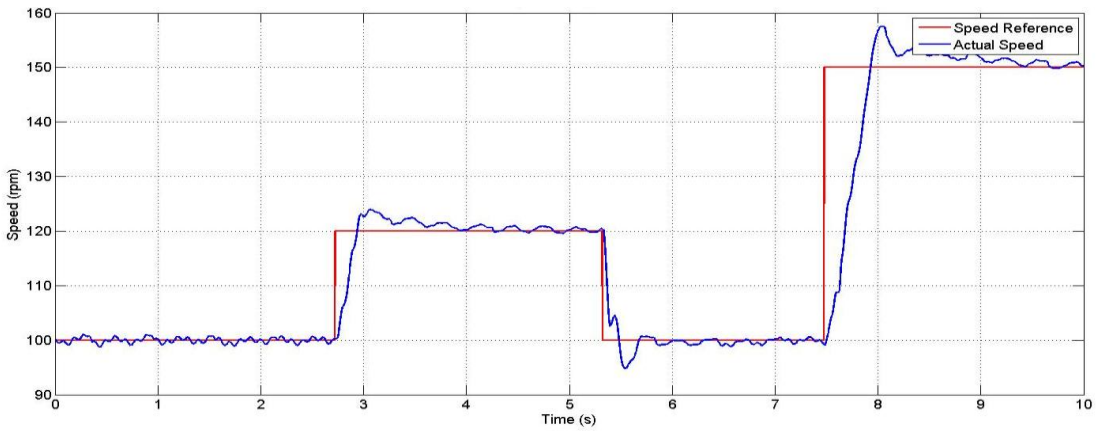

Figure 7.2: Response to a step in speed reference (motor-mode)

It can be seen that the system has a good response to the step-input. It should be noted that step-inputs represent the extreme case, one which is quite unrealistic as wind speeds do not step instantaneously. However, this was done to verify the response of the control system.

From figure 7.2 it can be seen that the reference speed is tracked within half a second although the system requires some time to settle into its steady speed. The change in speed is a result of a change in applied torque which is a function of the quadrature current component. The recorded current components in the dq-frame are shown in figure 7.3.

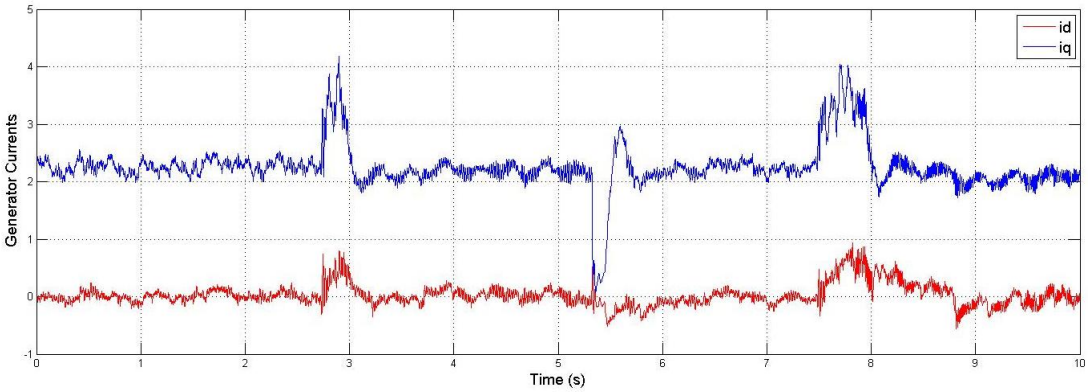

Figure 7.3: Machine dq-current response to a Speed-Step (motor mode)

The direct current component is maintained at zero although small changes are evident as the quadrature current component changes to accelerate the machine to its desired speed.

7.3. Generator Mode Operation

The change from motor-mode to generator-mode is achieved by changing the generator quadrature current from positive to negative values which results in an electromagnetic torque opposing the machines direction of rotation.

7.3.1. Current Control Mode

To verify the correct operation of the current controllers the machine is driven at a constant speed. Constant speed is assured by running the DC-machine used in the turbine emulator in speed-control mode. The speed is adjusted manually to 70rpm. A resistive load has been connected across the DC-Link to dissipate the generated

power. The grid side converter remains switched off. Different set points for the generator currents are applied while the outputs are measured. The dq-transforms of the recorded generator currents are shown in figure 7.4 together with the applied current references. The current reference as well as the resultant response is shown as a function of time.

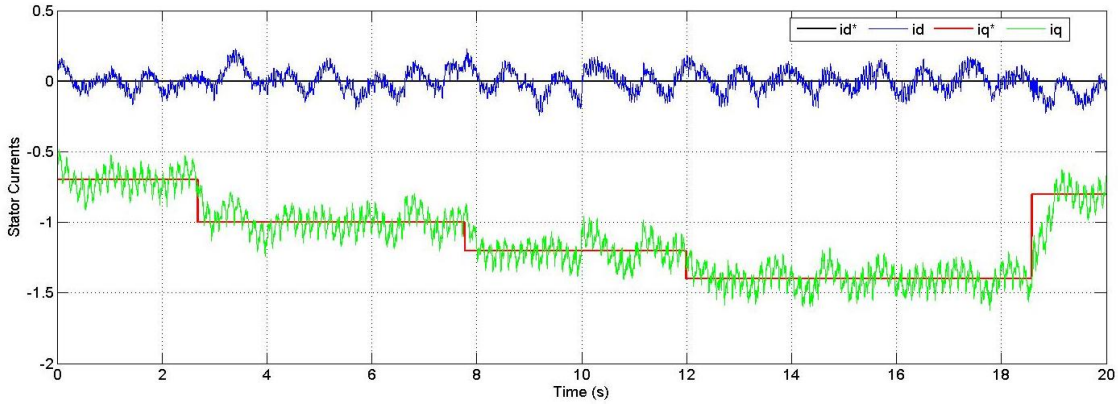

Figure 7.4: Generator Current Response

As expected from theory an increase in generator current results in a change in DC-Link Voltage as shown below. In chapter 5.3.1 the same setup was simulated, although at different speeds. However, the observed behaviour is in line with the simulation results. The higher speeds at which the simulations were carried out together with larger current references results in a higher DC-Link voltage as seen in figure 5.4 (a) and (b).

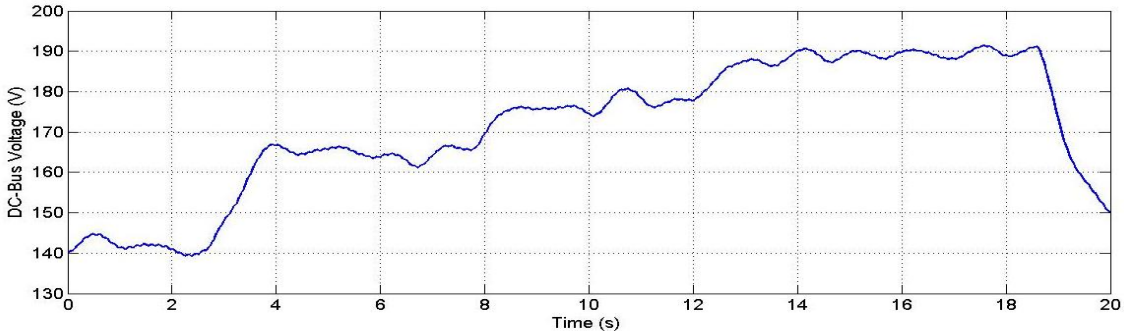

Figure 7.5: DC-Link Voltage

Based on the obtained results the generator side converter and its associated control is proven to work as expected.

7.4. Complete System Operation of the WECS

This section presents the results from operating the system as a whole. Wind Speeds in the range from 4m/s to 7m/s were applied and the results recorded. This was done for all three control strategies. In order to allow for a meaningful comparison, the system was allowed to settle into steady-state conditions before results were recorded. The focus of this work lies with the experimental implementation of a WECS and its operation. Furthermore the performance of the generator under different control strategies is examined to explore whether there is improvement in efficiency as predicted by the theory. Two key factors which directly impact on optimisation of the systems performance include the correct tracking of the MPP to extract maximum power from the incident wind and secondly the efficient operation of the generator to minimise incurred losses.

The first section of this chapter looks at the measured variables at one particular instance and evaluates the systems performance in comparison with the analytical and simulated values. The second section presents the system response to a step in wind speed. Finally the overall performance of the system is presented and discussed without looking at intermediate results.

7.4.1. Experimental Results at a wind speed of 7m/s

The relevant parameters of the system were recorded for all wind speeds investigated. This chapter looks at one set of recorded results, for a constant wind speed of 7m/s. It presents the relevant variables recorded, which impact on the overall system performance.

7.4.1.1. Machine Side Performance

From figure 4.3 in chapter 4 the value for the q-axis current component at a wind speed of 7m/s is expected to be $i_q = -11A$. Figure 7.6 shows the recorded q-axis current components under the three different control strategies applied.

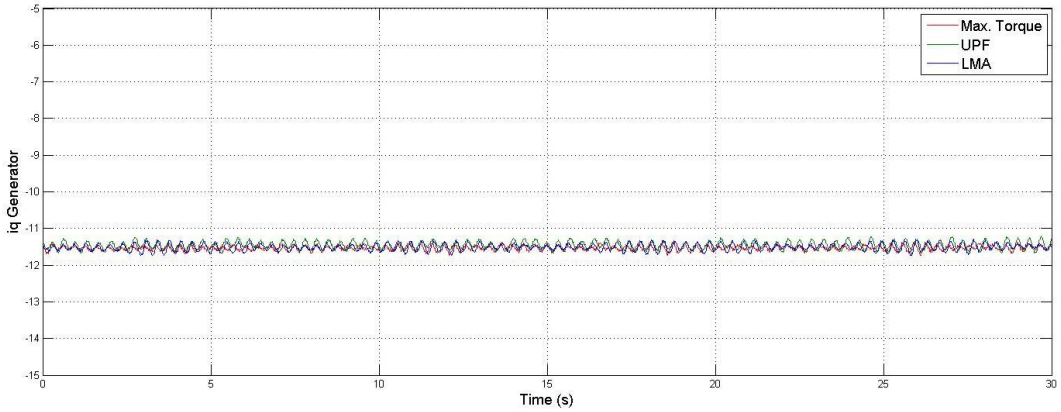

Figure 7.6: Measured q-axis current components under different control strategies

The theory presented in section 2.9 states that the q-axis component determines the developed torque of the machine and is controlled independently from the d-axis current component. It is therefore expected to be the same, regardless of which control strategy is applied as the control strategies merely impact on the d-axis current component. This was proven analytically as well as through simulations in chapters 4 and 5 respectively. The experimental results confirm this behaviour as evident from figure 7.6, which shows the quadrature current components under the three applicable control strategies. All three control strategies results in a q-axis current component of $i_{q,experimental} = -11.5A$, which is close to the value derived analytically. Simulating the system under the same wind speed also yields a value of $i_{q,simulated} = -11.5A$, although the simulations do not include frictional losses, resulting in higher values than predicted analytically.

The analytical values for the d-axis current component as a function of wind speed are shown in figure 4.4. At a wind speed of 7m/s the analytical value of the d-axis components are found to be $i_{d,analyticcal\ ,max.torque} = 0A$, $i_{d,analyticcal\ ,UPF} = -0.134A$ and $i_{d,analyticcal\ ,LMA} = -2.13A$, for the respective control strategies.

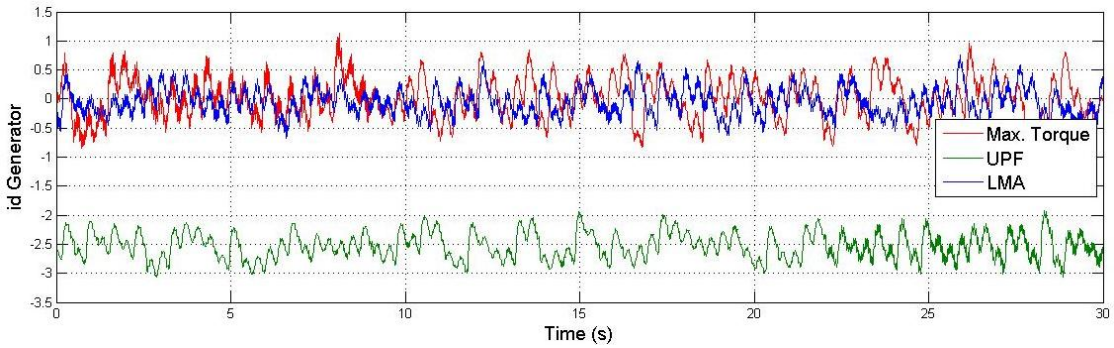

Figure 7.7: Measured d-axis current components under different control strategies

The experimental values differ slightly from the analytical results as shown in figure 7.7. The difference in d-axis current between maximum torque control and LMA control is too small to be observed in the experimental results. The magnitude of the ripple component is larger than the reference value. Under UPF control the d-axis current component is larger than in the analytical result which is a result of the larger q-axis component shown in figure 7.6. The reference for the d-axis component, which is calculated according to equation (3.16), increases accordingly. Using the actual value of the q-axis component in formula (3.16) yields an expected value in line with the recorded d-axis current component in figure 7.7.

The actual phase currents under the three different control strategies are shown in figure 7.8, 7.9 and 7.10 respectively. The figures show the recorded currents as well as a filtered version.

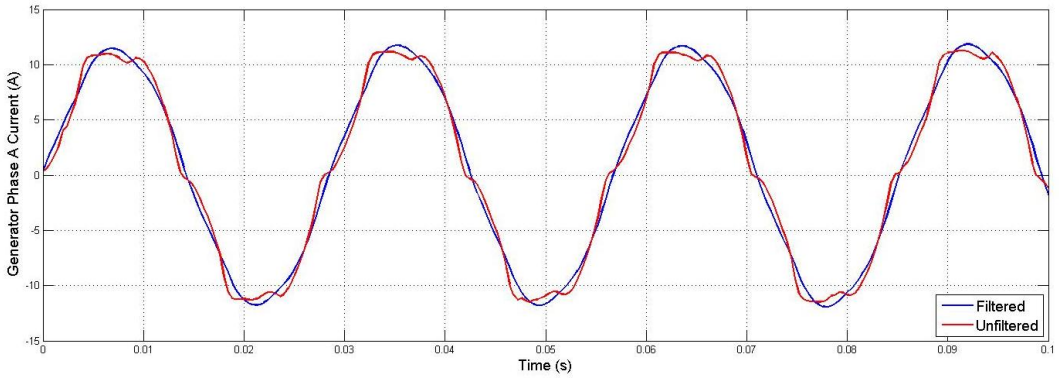

Figure 7.8: Generator Phase A Current (Max. Torque per current control)

The ripple in the current waveform is a result of the EMF waveform of the machine, which is not perfectly sinusoidal. Applying a perfectly sinusoidal voltage waveform to the machine terminals therefore results in a distorted current waveform as observed.

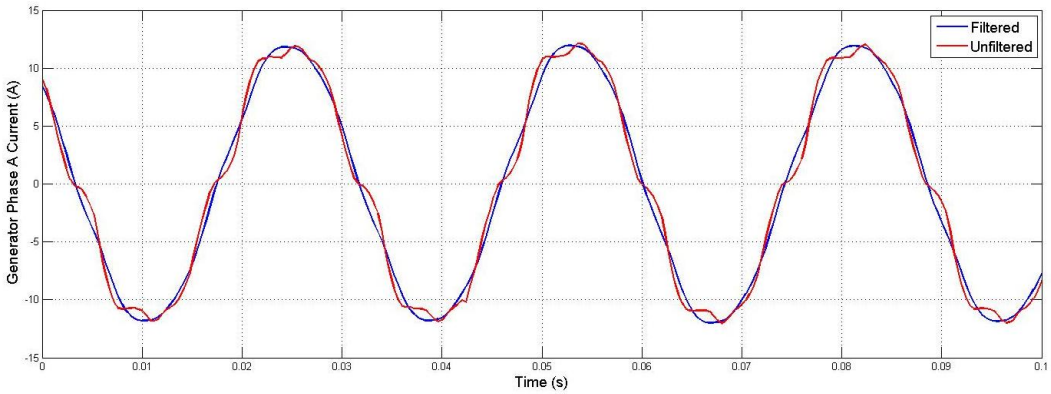

Figure 7.9: Generator Phase A Current (UPF control)

Under UPF control a significant d-axis current is introduced, in accordance with equation (3.16), which increases the total stator current. This can be observed in figure 7.9.

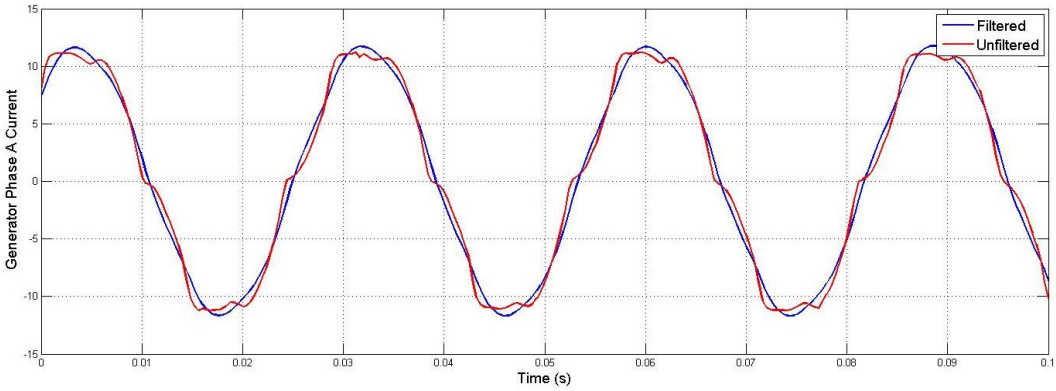

Figure 7.10: Generator Phase A Current (LMA control)

The phase current under LMA control is shown in figure 7.10. No significant changes are observed compared to the maximum torque control. This is expected from the minimal change in d-axis current component.

7.4.1.2. Grid Side Performance

The DC-Link Reference Voltage was kept at 400V throughout all experimental tests. A plot of the actual recorded DC-Link Voltage is shown in figure 7.11.

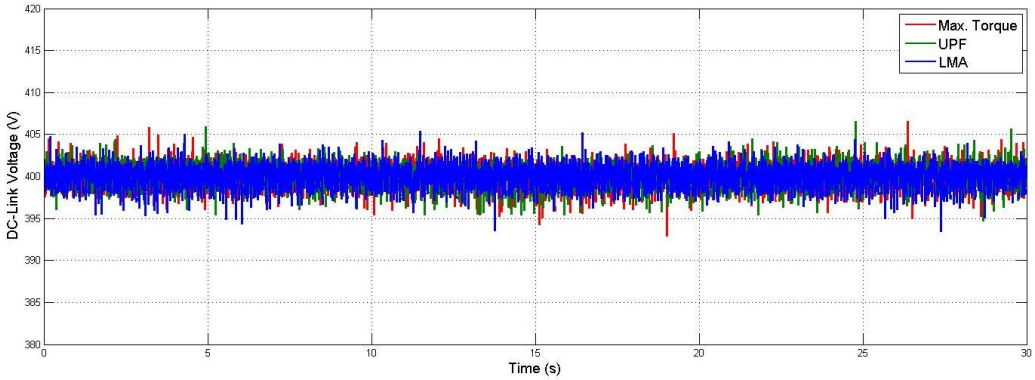

Figure 7.11: DC-Link Voltage

The DC-Voltage is maintained at its desired value under all three control strategies. As discussed in section 3.4, this is achieved by modifying the d-axis current component at the grid-side converter as required. The q-axis current component is maintained at zero throughout, thus forcing the reactive power to 0. The experimentally obtained d-axis current components are shown in figure 7.12. In accordance with the analytical and simulated results all three control strategies result

in the same d-axis current component as the power produced by the generator is essentially the same under all control strategies.

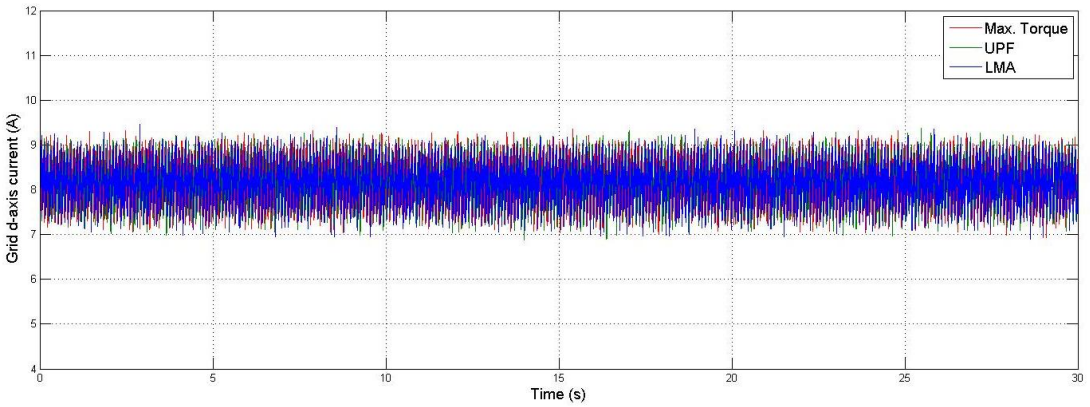

Figure 7.12: Grid-side d-axis current component under different control strategies

Part of the captured current waveform on the grid-side is shown in figure 7.13. This waveform was obtained while operating the system under maximum torque per current control. Waveforms under the other two control schemes have been omitted as they do not differ. Figure 7.14 shows the same currents transformed to the dq-reference frame.

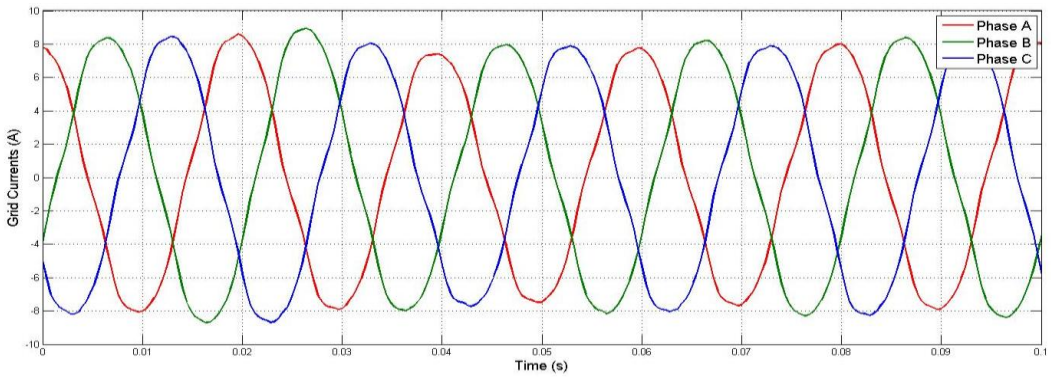

Figure 7.13: Captured grid currents (Generator in Max. Torque Control)

The currents captured on the grid side, shown in figure 7.13, display a considerable variation in magnitude over time which is reflected in the transformed d- and q-axis currents in figure 7.14. During the experimental setup it was found that the 220V provided by the transformer includes some voltage imbalance as well as harmonic distortion. Furthermore the grid-filter components were found to be not completely identical. The inductances in the three phases of the filter were found to vary up to 15%. These two factors contribute to the fluctuations in the grid-currents.

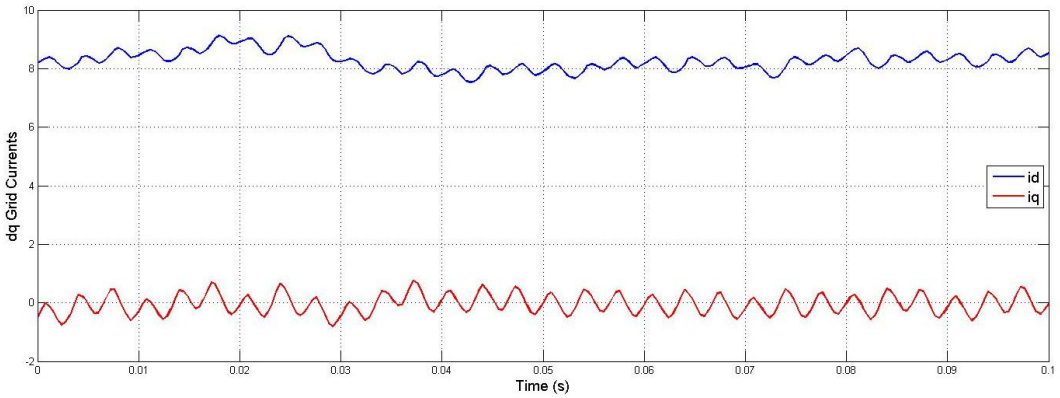

Figure 7.14: Captured grid currents in dq-frame (Generator in Max. Torque Control)

The stepped down grid phase voltages are captured and transformed to the dq-reference frame as shown in figure 7.15 and 7.16 respectively.

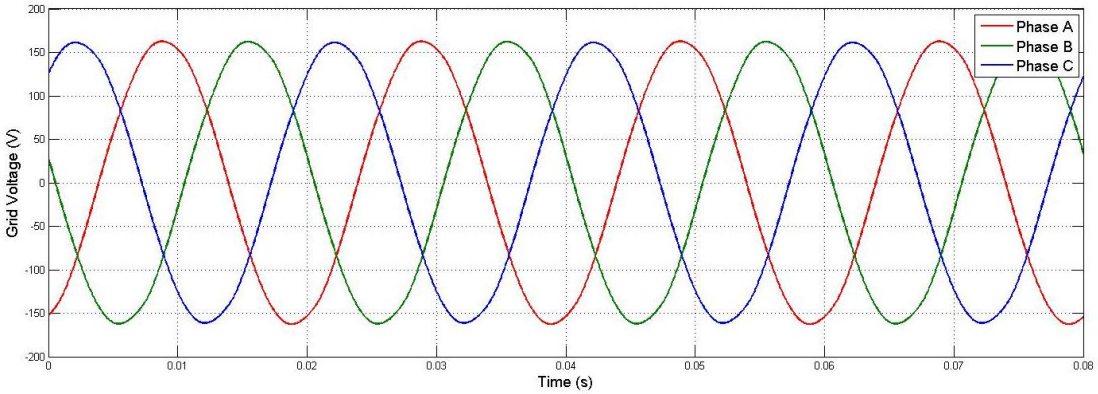

Figure 7.15: Captured grid voltages

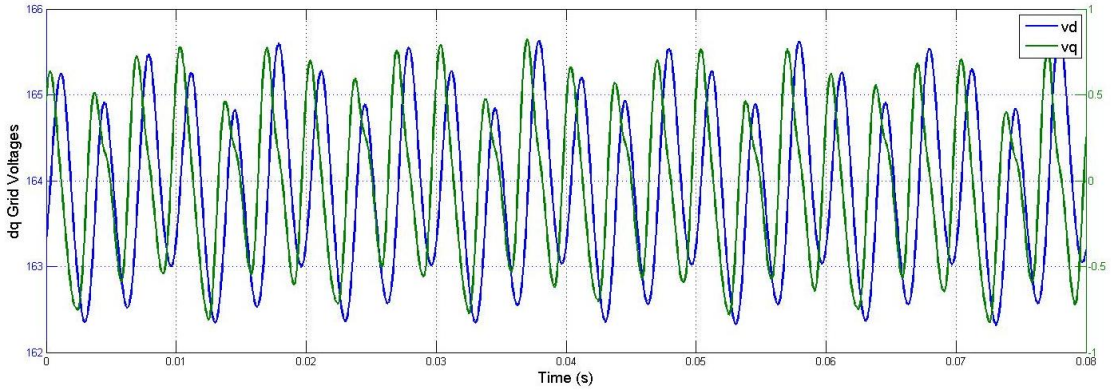

Figure 7.16: Captured grid voltages in the dq-reference frame

The transformed grid voltages, shown in figure 7.16. The imbalance in the grid voltages are evident, which leads to a 3V peak-to-peak ripple in the transformed grid voltages. The grid-side controller uses these voltages to control the grid-currents as shown in figure 3.5. From the current waveforms it is evident that the ripple in the dq-voltages is carried through to the currents as evident in figure 7.14.

7.4.2. Complete System Response to a Step in Wind Speed

The focus of the work carried out lies with implementation and operation of a WECS. Focus is given to the steady-state performance of the system as a whole as well as the individual components as presented earlier. In addition a step-response test was carried out. The purpose of the step test is to verify the dynamic capabilities of the system. It also proves that further work can be carried out on the developed setup, including dynamic behaviour based around real wind data. The wind speed applied was stepped from 3.5m/s to 4m/s as shown in figure 7.17.

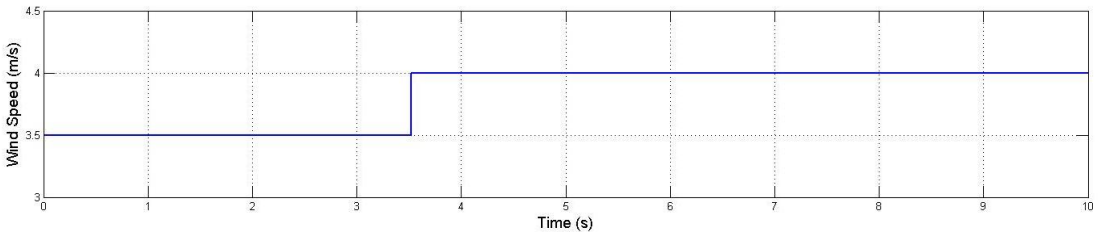

Figure 7.17: Wind Speed Step

In order to track the MPP the generator needs to be accelerated. This is achieved by reducing the quadrature current component to allow the machine to accelerate. The recorded generator currents in the dq-frame are shown in figure 7.18.

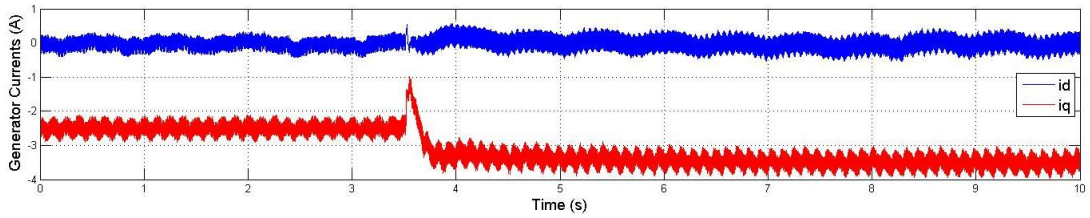

Figure 7.18: Generator Current Response to a step in wind speed

The recorded currents compare favourably to the simulated results presented in figure 5.25. The simulated currents are slightly larger than the experimental currents. This can be attributed to the absence of friction in the simulated results, which produces a large effective torque being applied to the generator. The transient period observed in simulation is much shorter than in the experimental results, which can be attributed to the omission of inertia in the simulation which allows for an almost instantaneous change in machine speed. From the generator currents and voltages the active and reactive power components can be computed according to equations (2.15) and (2.16) as shown in figure 7.19 below.

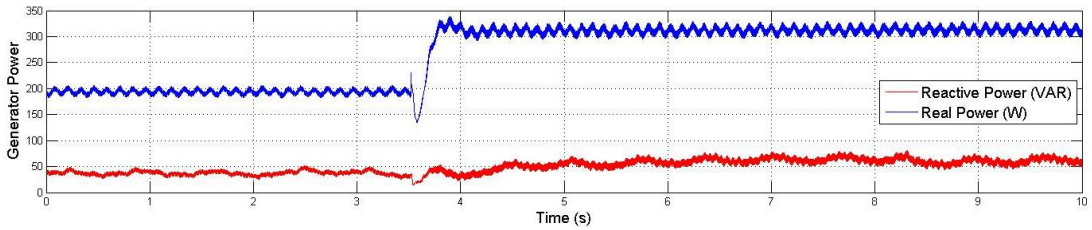

Figure 7.19: Generator power components

Figure 7.20 shows the speed response obtained experimentally.

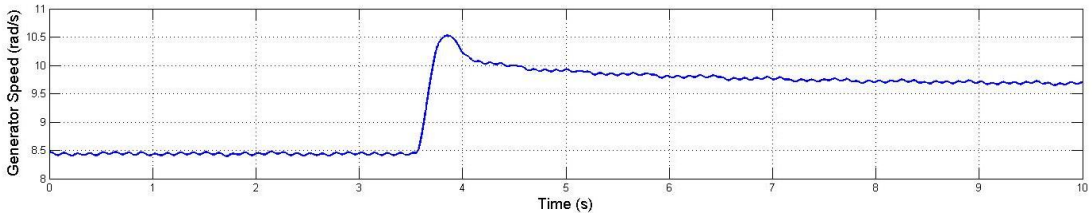

Figure 7.20: Generator speed response to a step in wind speed

Based on the applied wind speed and the measured generator speed the turbine emulator calculated the turbine torque as shown in figure 7.21.

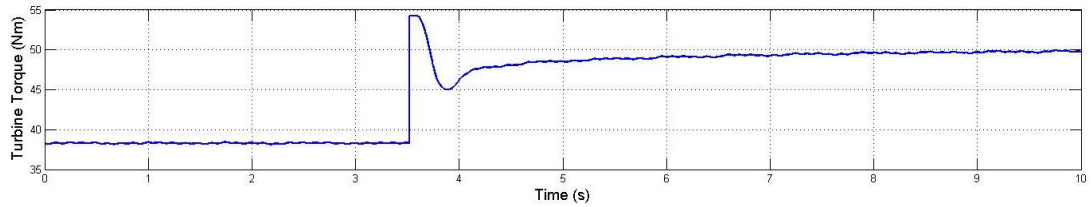

Figure 7.21: Turbine torque response to a step in wind speed

The aim of the MPPT algorithm is to maximise the power coefficient under any given wind condition. Figure 7.22 shows the power coefficient and its behaviour during the transient period.

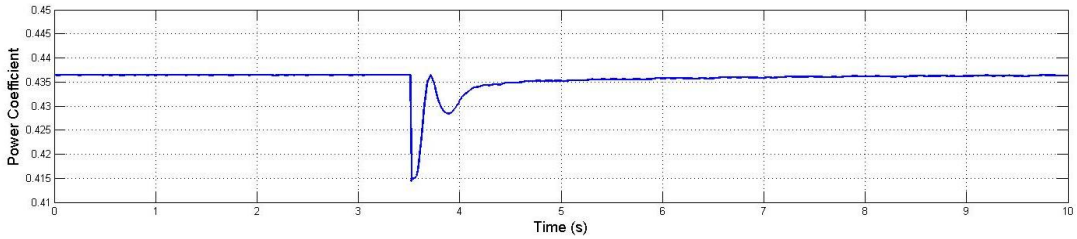

Figure 7.22: Turbine power coefficient response to a step in wind speed

In figure 7.22 it can be observed how the power coefficient initially drops as the wind speed is stepped up at t=3.5seconds. It climbs back up to its maximum values as the turbine speed approaches the optimum speed before dropping again due to the overshoot in turbine speed, evident from figure 7.20. As the turbine speed settles to its optimum value, so does the power coefficient.

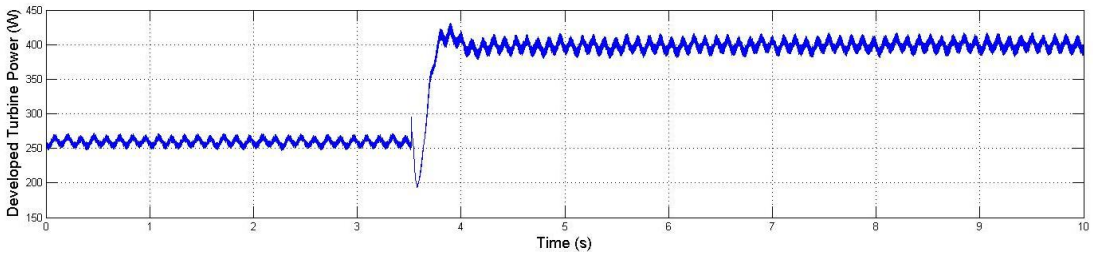

Figure 7.23: Developed turbine power response to a step in wind speed

The power extracted from the wind is shown in figure 7.23. It exhibits the same initial dip as the wind speed is stepped up and overshoots thereafter before settling to its steady-state value after t=4seconds.

The grid-side converter is expected to maintain the DC-voltage at 400V. The actual DC-voltage measured is shown in figure 7.24.

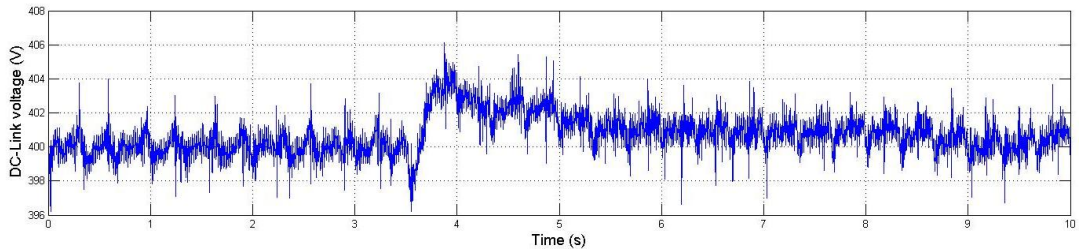

Figure 7.24: DC-Link voltage

In order to maintain the desired DC-Link voltage the d-axis current component of the grid currents is modified accordingly, whilst the q-axis current component remains unchanged. This is shown in figure 7.25.

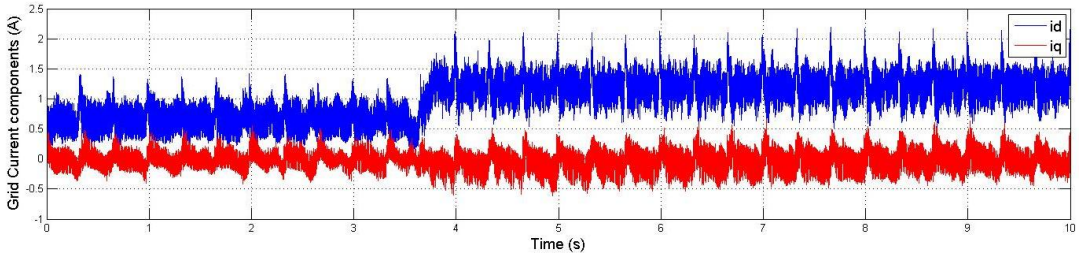

Figure 7.25: Grid currents

It can clearly be observed how the d-axis component of the grid current is increased in response to the increase in DC-Link voltage. This counteracts the rise in DC-voltage by increasing the transfer of real power to the grid, as shown in figure 7.26

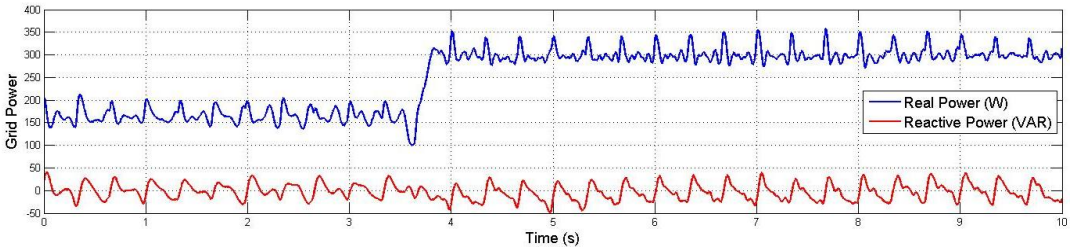

Figure 7.26: Real and Reactive Power transferred to the grid

Based on the results presented in this section it can be concluded that the PM WECS which was implemented provides a valid platform to perform static and dynamic experimental tests on the performance of such a system. The MPPT tracks the MPP accurately within less than 0.5 seconds when a step input is applied. As mentioned previously, wind does not change instantaneously. However, the ability to deal with a step change effectively is evidence that more realistic wind speed profiles can be tracked accurately, within the applicable system limits.

7.4.3. Experimental Evaluation of different generator control strategies and their impact on power production

In chapters 4 and 5, the use of a MPPT algorithm was discussed to obtain maximum power from the incident wind. The control of the generator under three different control strategies was also investigated, to minimise its losses. In the previous section the experimental results for static and dynamic operation have been presented and discussed, with attention given to the intermediate results, such as currents, DC-voltage, etc.

This section presents and discusses the overall performance of the WECS, both at the generator output and the grid side, and the impact that different control strategies have on its performance.

7.4.3.1. Generator Side Performance

The real power output of the generator was measured under the three control strategies. The output power as a function of wind speed is shown in figure 7.27 below.

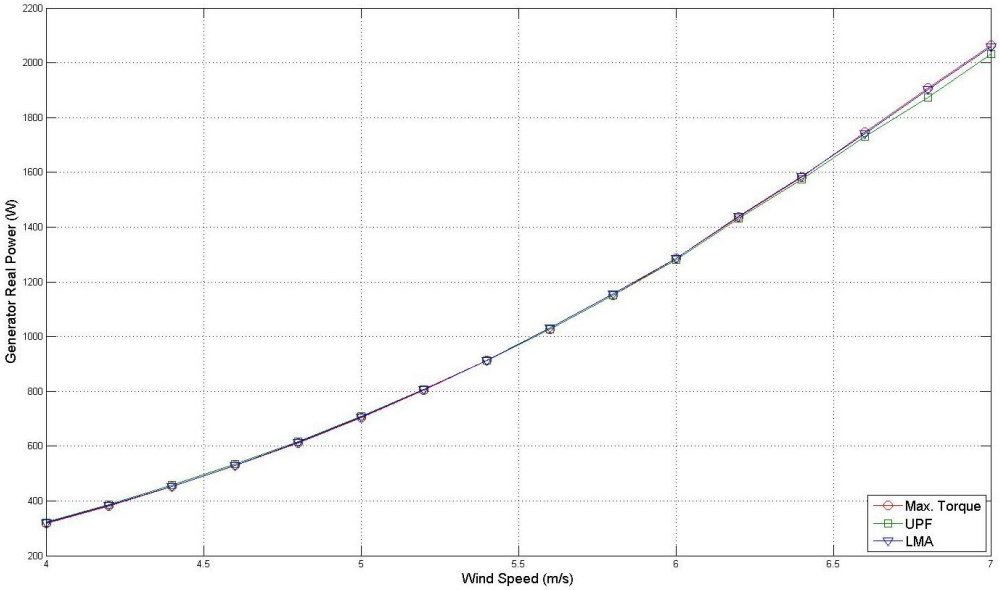

Figure 7.27: Real generator power under the three control strategies investigated

There is no difference in the generator output power until approximately 6m/s. At wind speeds above 6m/s, and therefore loading above 1.3kW, the UPF control strategy produces less power than the maximum torque per current and LMA control. This can be attributed to the increased copper losses, which is a result of the higher stator current. Comparing the experimental results to the analytically calculated generator power, shown in figure 4.10, validates these findings.

The generator efficiency was calculated as the ratio of real power output to the mechanical shaft power applied by the turbine emulator according to:

$$\eta_{Gen} = \frac{P_{Gen}}{P_{shaft}} \cdot 100\% \qquad (7.1)$$

Figure 7.28 shows the obtained generator efficiency as a function of wind speed under steady-state conditions.

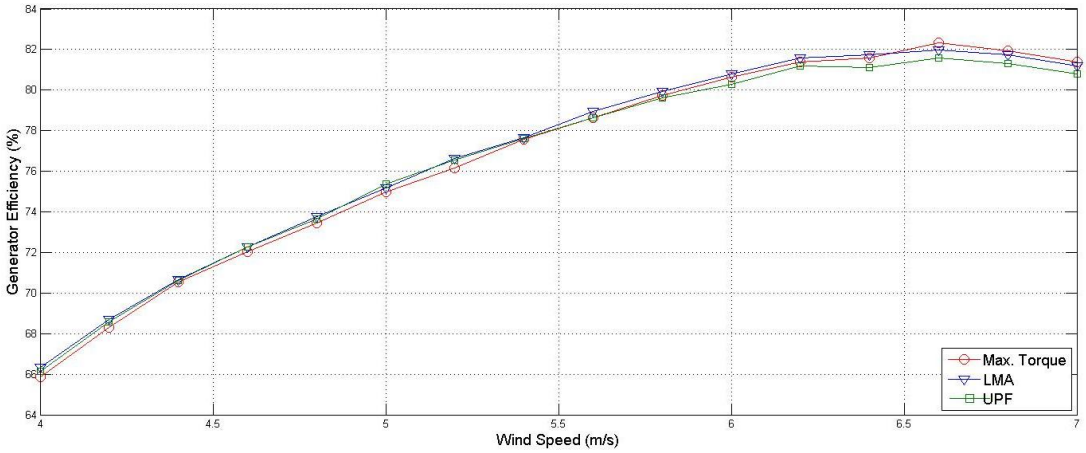

Figure 7.28: Generator Efficiency under Steady-State Conditions vs. Wind Speeds

Comparing the experimental results to the analytical and simulated outcome shows discrepancies between the absolute values obtained through simulations and experimentally. However, the trends observed in the analytical and simulated results are confirmed experimentally. The efficiency curves shown in figure 7.28 are a result of the changing generator efficiency at different loading points. Lower wind speeds translate into lower loading points. At higher wind speeds the PMSG is operated closer to its rated values which results in higher efficiency, as evident in figure 7.28.

In the analytical as well as simulated results the Unity Power Factor control performs worst, especially at higher wind speeds, with the two other control strategies showing no difference in the wind speed range investigated. The experimental results presented in figure 7.28 confirm this.

Several reasons contribute to the almost identical performance of the maximum torque per current control and the LMA. These include the method of extracting mechanical losses of the system as a function of speed, as described in chapter 6.1 and the assumptions made to obtain these values, which can lead to an error in the model for the core losses. The LMA is based on the core loss model and will therefore be affected. Furthermore the impact of temperature change has been neglected in the experimental implementation as well as the analytical and simulated results. However, temperature changes are present and do impact on the results in an experimental environment, which are difficult to model in the analytical or simulation environment.

7.4.3.2. Grid Side Performance

The real power transferred to the grid is shown in figure 7.29 at various wind speeds.

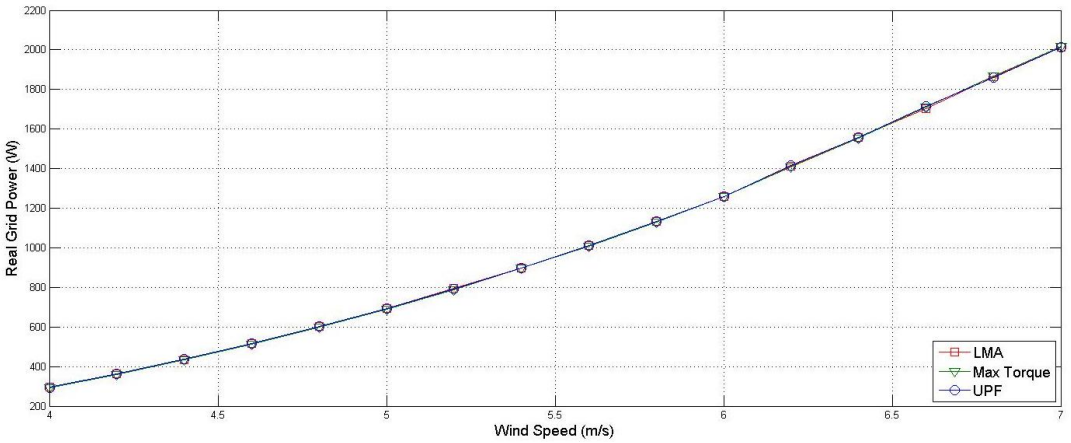

Figure 7.29: Real Grid Power under steady-state conditions vs. Wind speed

In figure 5.22 the simulated real power transferred to the grid is shown as a function of wind speed. Both curves, simulated and experimentally obtained, exhibit the same quadratic behaviour expected from the turbine characteristics. There is a difference in absolute values between the two results. The same reasons as mentioned in the discussion of the generator power and efficiency curves apply here. In addition losses associated with the power converters, mainly switching losses, as well as the grid filter impact on the experimental results. The inductors used in the laboratory have a certain resistance which was not considered in the simulations. This will cause additional losses. However, as previously mentioned these inaccuracies are present under all three control strategies and do not impact on a comparison of those.

To obtain the efficiency of the system as a whole, the real power transferred to the grid was calculated as a percentage of turbine shaft power.

$$\eta_{System} = \frac{P_{Grid}}{P_{shaft}} \cdot 100\% \qquad (7.2)$$

Overall system efficiency at different wind speeds is shown in figure 7.30.

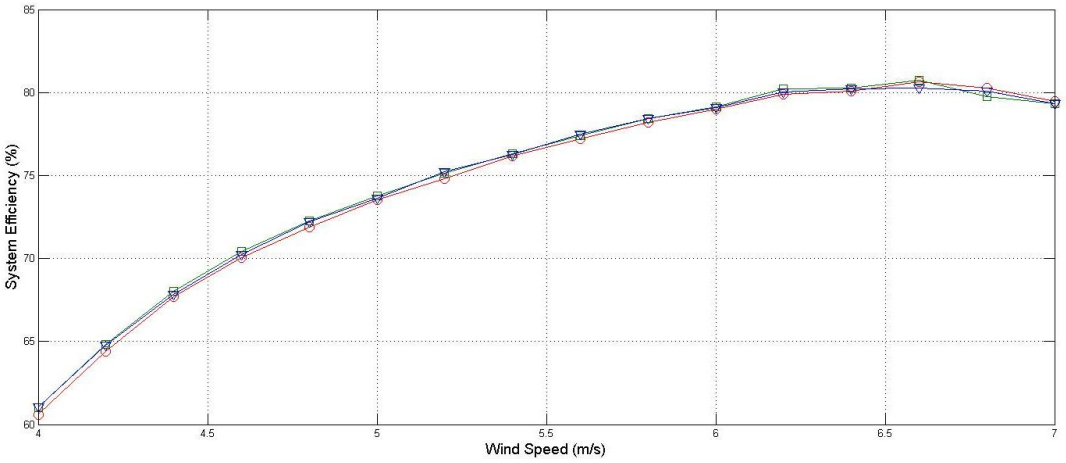

Figure 7.30: System Efficiency under Steady-State Conditions vs. Wind speed

The system efficiency curves are very close and differ less than one percent. As the generator power measured shows the same behaviour, this is an expected outcome. Losses associated with the power converters and grid filter do not differ as the grid side converter control strategy is always the same.

7.5. Conclusions

The experimental results obtained in the laboratory have been presented and discussed in this section. The individual system components were tested individually to validate the correct operation of each part of the system. Subsequently, the WECS was operated as a whole. A thorough analysis of the captured parameters under steady-state conditions was presented and the outcome discussed. Furthermore, the response of the system to a step change in wind change was shown and analysed. Finally the impact of three different machine control strategies on the performance of the WECS is presented.

Chapter 8

Conclusion and Recommendations

From the analytical, simulated and experimental results obtained throughout this thesis certain conclusion can be drawn. These are discussed here. Based on these conclusions, certain recommendations are given.

8.1. Conclusions

In this thesis the analysis and implementation of a PM WECS is presented. Based on the findings of the thesis, the following conclusions can be drawn:

8.1.1 The model of a wind turbine and its governing equations was formulated. Based on the developed model, a wind turbine emulator was simulated and implemented experimentally. The correct operation of the turbine emulator was validated through simulation and a set of experimental tests. Based on the experimental results obtained, it can be concluded that the turbine emulator behaves as predicted in theory. The effect of furling, tower shadowing and turbine inertia were omitted for simplicity. Due to the DC-motor available the operating range was limited to 2.23kW, or a wind speed of 7m/s.

8.1.2 A detailed model of the PMSG has been developed. The control of the machine has been discussed and investigated. This was done in theory, simulation and finally experimentally. A series of tests were carried out to validate the correct operation of the machine-side control, including current and speed control as well as motor-mode and generator mode of operation. These validated the correct operation of the controllers. Reference speeds were applied to the controller and tracked correctly.

Due to the absence of a torque transducer the developed shaft torque was estimated from loss models. In addition the impact of temperature changes was neglected.

8.1.3 The options available to interface the WECS to the grid were investigated and a grid-converter, together with a LCL-type grid filter was evaluated. Through simulations the correct operation of the grid-tied inverter was validated. The grid-current components were found to have some imbalance as well as a considerable amount of current ripple. This can partly be attributed to the mismatch between the components used as well as the use of non-ideal components. This was necessitated by the available components.

Maintaining the DC-link voltage by transferring any energy to the grid is the main objective of the grid-side converter. This was validated in simulation as well as experimentally during the operation of the WECS as a whole. The DC-link voltage was maintained as desired while the reactive power reference was set to zero and tracked successfully.

8.1.4 The complete operation of the WECS was investigated. Combining the wind turbine emulator, machine-side controller and the grid-tied inverter completes the WECS. Steady-state operation is presented and discussed. Furthermore the dynamic response to a step change is investigated in a simulated environment as well as experimentally. The complete system was implemented on two dSPACE kits, to control each converter through SVM. Controlling the PMSG under the three proposed control strategies, while observing overall system efficiency showed no considerable impact. The non-salient machine design reduces the impact of the proposed LMA on the machine efficiency.

8.2. Recommendations

8.2.1 The wind turbine emulator can be further improved by including the following phenomena: turbine shadowing, furling as well as the impact of inertia and friction on the turbine performance. Furthermore, the use of a large motor will extend the operating range and match the PMSG's full rating.

8.2.2 Using a torque transducer to accurately measure the developed shaft torque should be investigated. This could lead to a more accurate loss model of the machine, thereby increasing the accuracy of the predicted losses. The impact of temperature on the PMSG's performance should be investigated.

8.2.3 Using better matched and more ideal components to construct the grid-filter should be considered. This could improve the performance of the grid-side converter, whilst decreasing current ripple and imbalance.

Using more sophisticated design methods to obtain the filter components should be investigated.

8.2.4 The operation of the whole system under a wider range of wind speeds should be investigated to investigate the impact of loading on system performance. Furthermore the system could be implemented using a different PM machine, with saliency, to validate the LMA.

In addition, further investigation of the system's performance under dynamic wind conditions should be considered. This could be used to investigate performance under real wind speed data.

References

1. D.C. Aliprantis, S.A. Papathanassiou, M.P. Papadopoulos, A.G. Kladas. "Modeling and control of a variable-speed wind turbine equipped with permanent magnet synchronous generator", *Proc. Of ICEM*, 2000, Vol.3, pp.558-562.

2. Kenji Amei, Yukichi Takayasu, Takahisa Ohji, Masaaki Sakui, "A Maximum Power Control of Wmd Generator System Using a Permanent Magnet Synchronous Generator and a Boost Chopper Circuit", *IEEE PCC*, Osaka, 2002, pp. 1447-1452.

3. Christos Mademlis, Jannis Zypteras, Nikos Margaris, "Loss Minimization in Surface Permanent-Magnet Synchronous Motor Drives", *IEEE Transactions*, Vol. 47, 2000

4. Antonio O. Di Tommaso, Rosario Miceli, Giuseppe Ricco Galluzzo, Marco Trapanese, "Efficiency Maximization of Permanent Magnet Synchronous Generators Coupled to Wind Turbines", *Power Electronics Specialists Conference*, 2007, PESC 2007

5. M. Chinchilla, S. Arnalte, J.C. Burgos, J.L. Rodriques, "Efficient Control of Permanent Magnet Synchronous Generators Applied to Variable Speed Wind Energy Systems", *Renewable Energy Journal*, Volume 31, Issue 9, July 2006, pp. 1455-1470

6. M. Chinchilla, Santiago Arnaltes, Juan Carlos Burgos, "Control of Permanent-Magnet Generators Applied to Variable-Speed Wind-Energy Systems Connected to the Grid", *IEEE Transactions on Energy Conversion*, Volume 21, Issue 1, 2006, pp. 130-135

7. Shigeo Morimoto, Yi Tong, Yoji Takeda, Takao Hirasa , "Loss Minimization Control of permanent Magnet Synchronous Motor Drives", *IEEE Transactions on Industrial Electronics*, Volume 41, Issue 5, 1994, pp 511-517

8. Shigeo Morimoto, Hajime Kato, Masayuki Sanada, Yoji Takeda, "Output Maximization Control for Wind Generation System with Interior Permanent Magnet Synchronous Generator", *Conference Record of the 41st IEEE Industry Applications Conference,* 2006*,* Volume 1, pp. 503-510

9. Shigeo Mrimoto, Hideaki Nakayama, Masayuki Sanada, Yoji Takeda, "Sensorless Output Maximization Control for Variable-Speed Wind Generation System Using IPMSG", *Conference Record of the Industry Applications Conference*, 2003, Volume 3, pp. 1464-1471

10. Bunlung Neammanee, Somporn Sirisumrannukul and Somchai Chatratana, "Development of a Wind Turbine Simulator for Wind Generator Testing", *International Energy Journal*, Volume 8, Issue 1, March 2007

11. M.B. Bana Sharifian, Y. Mohamadrezapour, M. Hosseinpour, S. Torabzade, "Maximum Power Control of Grid Connected Variable Speed Wind System

through Back to Back Converters", *Journal of Applied Science*, 2008, Volume 8, pp. 4416-4421

12. Harri Vihriala, "Control of Variable Speed Wind Turbines", *PhD Thesis*, October 2002, Tampere University of Technology

13. Seung-Ho Song, Shin-il Kang, Nyeon-Kun Hahm, "Implementation and Control of Grid Connected AC-DC-AC Power Converter for Variable Speed Wind Energy Conversion System", *Eighteenth Annual IEEE Applied Power Electronics Conference and Exposition,* 2003*,* Volume 1, pp. 154-158

14. Remus Teodorescu, Florin Iov and Frede Blaabjerg, "Flexible development and test system for llkW wind turbine", *IEEE 34th Annual Power Electronics Specialist Conference,* 2003*,* Volume 1, pp. 67-72

15. M. Chinchilla, S. Arnaltes, J.L. Rodriquiez-Amenedo, "Laboratory set-up for Wind Turbine Emulation", *IEEE International Conference on Industrial Technology*, 2004, Volume 1, pp. 553-557

16. P.E. Battaiotto, R.J. Mantz, P.F. Puleston, "A Wind Turbine Emulator based on a Dual DSP Processor System", *Control Engineering Practice*, Volume 4, Number 9, September 1996 , pp. 1261-1266

17. Bunlung Neammanee, Somporn Sirisumrannukul, Somchai Chatratana, "Development of a Wind Turbine Simulator for Wind Generator Testing", *International Energy Journal*, Volume 8, Issue 1, March 2007

18. Iulian Munteanu, Antoneta Iuliana Bratcu, Nicholas-Antonio Cutululis, Emil Caenga, "Optimal Control of Wind Energy Systems", 2008, Springer

19. Siegfried Heier, "Grid Integration of Wind Energy Conversion Systems", 2006, Wiley

20. Freede Blaabjerg, Remus Reodorescu, Zhe Chen, Marco Liserre, "Power Converters and Control of Renewable Energy Systems", *Proceedings of the 6th International Conference on Power Electronics*, 2004, Volume. 1, pp. 1–20

21. Kelvin Tan, Syed Islam, "Optimum Control Strategies in Energy Conversion of PMSG Wind Turbine System Without Mechanical Sensors", *IEEE Transactions on Energy Conversion*, Vol. 19, No. 2, June 2004, pp. 392-400.

22. Mariusz Malinowski, Steffen Brenet, "Simple Control Scheme of Three-Level PWM Converter Connecting Wind Turbine with Grid", Chalmers University of Technology

23. Jianzhong Zhang, Ming Cheng, Zhe Chen, "Nonlinear Control for Variable-Speed Wind Turbines with Permanent Magnet Generators", *International Conference on Electrical Machines and Systems,* 2007*,* pp. 324-329

24. M. F. Moussa, A. helal, Y. Gaber H. A. Youssef, "Unity Power Factor Control of Permanent Magnet Motor Drive System", *12th International Power System Conference*, 2008, pp.360-367

25. Quincy Wang, Liuchen Chang, "PWM control strategies for wind turbine inverters", *IEEE Canadian Conference on Electrical and Computer Engineering,* 1998*,* Volume 1, pp. 309-312

26. Samuel Vasconcelos Araujo, Alfred Engler, Benjamin Sahan, Fernando Luiz Marcelo Antunes, "LCL Filter Design for grid-connected NPC inverters in offshore wind turbines", *7th International Conference on Power Electronics,* 2007, pp.1133-1138

27. Mustapha Raou, Moulay Tahar Lamchich, "Average Current Moder Control of a Voltage SOurce Inverter connected to the Grid: Application to different filter cells ", *Journal of Electrical Engineering*, Volume 54, Number 3-4, 2004, pp.77-82

28. Pasi Peltoniemi, "Comparison of the Effect of Output Voltage Filters in the Total Harmonix Distortion of Line Current in Voltage Source Line Converters - Simulation Study", *International Conference on Renewable Energies and Power Quality*, 2006

29. Wei Sun, Zhe Chen and Xiaojie Wu, "Intelligent Optimize Design of LCL Filter for Three-Phase Voltage-Source PWM Rectifier", *IEEE 6th International Power Electronics and Motion Control Conference,* 2009, pp.970-974

30. M. Tavakoli Bina, E. Pashajavid, "An efficient procedure to design passive LCL-filters for active power filters", *Electric Power Systems Research on Science Direct*, Volume 79, 2008, pp. 606–614

31. M.A. Khan, "Contributions to Permanent Magnet Wind Generator Design Including the Application of Soft Magnetic Composites", *PhD Thesis*, 2006, University of Cape Town

32. P. Barendse, "Equivalent Circuit Parameters of the Permanent Magnet Machine", University of Cape Town

Appendix A: Analytical Results

Table A.1: Theoretical Generator Output Power as a function of wind speed for the machine used in this project

Wind Speed (m/s)	Output Power Max. Torque	Output Power UPF	% Change compared to Max. Torque	Output Power LMA	% Change compared to Max. Torque
4.00	379.21	379.18	-0.01	379.21	0.002
4.20	444.90	444.84	-0.01	444.91	0.002
4.40	517.13	517.03	-0.02	517.14	0.002
4.60	596.16	595.99	-0.03	596.17	0.002
4.80	682.25	681.98	-0.04	682.26	0.002
5.00	775.63	775.23	-0.05	775.64	0.002
5.20	876.56	875.97	-0.07	876.58	0.002
5.40	985.27	984.42	-0.09	985.29	0.002
5.60	1102.00	1100.79	-0.11	1102.02	0.002
5.80	1226.97	1225.30	-0.14	1226.99	0.002
6.00	1360.41	1358.13	-0.17	1360.44	0.002
6.20	1502.54	1499.46	-0.20	1502.57	0.002
6.40	1653.57	1649.48	-0.25	1653.60	0.002
6.60	1813.71	1808.33	-0.30	1813.74	0.002
6.80	1983.16	1976.16	-0.35	1983.20	0.002
7.00	2162.13	2153.11	-0.42	2162.18	0.002
7.20	2350.81	2339.27	-0.49	2350.86	0.002
7.40	2549.39	2534.76	-0.57	2549.44	0.002
7.60	2758.06	2739.65	-0.67	2758.11	0.002
7.80	2976.98	2953.98	-0.77	2977.04	0.002
8.00	3206.35	3177.79	-0.89	3206.41	0.002
8.20	3446.33	3411.09	-1.02	3446.39	0.002
8.40	3697.08	3653.85	-1.17	3697.15	0.002
8.60	3958.76	3906.03	-1.33	3958.84	0.002
8.80	4231.54	4167.53	-1.51	4231.62	0.002
9.00	4515.55	4438.24	-1.71	4515.64	0.002

Table A.2: Theoretical Generator Output Power as a function of wind speed for the modified machine

Wind Speed (m/s)	Output Power Max. Torque	Output Power UPF	% Change compared to Max. Torque	Output Power LMA	% Change compared to Max. Torque
4.00	63.38	63.43	0.07	63.83	0.71
4.20	81.44	81.51	0.08	81.95	0.63
4.40	101.67	101.77	0.10	102.26	0.58
4.60	124.18	124.32	0.11	124.86	0.54
4.80	149.08	149.27	0.13	149.84	0.51
5.00	176.46	176.70	0.14	177.31	0.48
5.20	206.42	206.74	0.16	207.38	0.46
5.40	239.07	239.48	0.17	240.15	0.45
5.60	274.51	275.03	0.19	275.71	0.44
5.80	312.84	313.48	0.20	314.17	0.42
6.00	354.16	354.94	0.22	355.63	0.41
6.20	398.58	399.52	0.24	400.19	0.41
6.40	446.18	447.30	0.25	447.96	0.40
6.60	497.07	498.40	0.27	499.02	0.39
6.80	551.35	552.92	0.28	553.49	0.39
7.00	609.12	610.94	0.30	611.46	0.38
7.20	670.48	672.58	0.31	673.03	0.38
7.40	735.53	737.92	0.33	738.30	0.38
7.60	804.36	807.07	0.34	807.36	0.37
7.80	877.07	880.11	0.35	880.33	0.37
8.00	953.76	957.15	0.35	957.28	0.37
8.20	1034.53	1038.26	0.36	1038.33	0.37
8.40	1119.47	1123.55	0.36	1123.57	0.37
8.60	1208.69	1213.10	0.36	1213.10	0.36
8.80	1302.27	1306.98	0.36	1307.00	0.36
9.00	1400.31	1405.29	0.36	1405.39	0.36

Appendix B: Tabulated Simulation Results

Table B.1: Simulated Grid Power vs. Wind Speed

Wind Speed (m/s)	Shaft Power (W)	Grid Power (W) under Max. Torque Control	Grid Power (W) under UPF Control	Grid Power (W) und LMA Control
4	482.33	390.35	390.35	390.35
4.5	686.75	577.08	577.08	577.18
5	942.05	810.91	810.91	810.91
5.5	1253.9	1096.55	1095.65	1096.65
6	1627.8	1438.68	1436.78	1438.68
6.5	2069.7	1841.71	1838.21	1841.71
7	2585	2310.24	2304.04	2310.34

Appendix C: Tabulated Experimental Results

Table C.1: Real Generator power under Steady-State Conditions

Wind Speed [m/s]	Tmax	UPF	% Change compared to Max. Torque	LMA	% Change compared to Max. Torque
4	350.6	354.9	1.2	353.1	0.7
4.2	421.0	426.2	1.2	423.5	0.6
4.4	499.9	504.5	0.9	500.9	0.2
4.6	583.3	589.4	1.0	585.1	0.3
4.8	675.4	681.4	0.9	678.2	0.4
5	777.8	781.8	0.5	779.5	0.2
5.2	886.8	891.6	0.5	892.0	0.6
5.4	1007.3	1008.2	0.1	1008.3	0.1
5.6	1134.5	1134.6	0.0	1138.4	0.3
5.8	1272.1	1270.8	-0.1	1275.4	0.3
6	1418.4	1412.8	-0.4	1420.8	0.2
6.2	1585.1	1581.0	-0.3	1588.3	0.2
6.4	1747.6	1738.0	-0.5	1750.8	0.2
6.6	1929.0	1911.8	-0.9	1921.4	-0.4
6.8	2106.5	2069.5	-1.8	2100.9	-0.3
7	2278.1	2242.3	-1.6	2272.9	-0.2

Table C.2: Real Grid Power under Steady-State Conditions

Wind Speed [m/s]	Tmax	UPF	% Change compared to Max. Torque	LMA	% Change compared to Max. Torque
4	321.5	323.8	0.7	323.7	0.7
4.2	395.6	398.1	0.6	397.9	0.6
4.4	478.2	480.2	0.4	479.1	0.2
4.6	565.1	568.4	0.6	566.7	0.3
4.8	658.8	662.3	0.5	661.6	0.4
5	759.9	762.1	0.3	760.9	0.1
5.2	868.0	871.9	0.5	872.9	0.6
5.4	985.6	986.8	0.2	987.5	0.1
5.6	1109.6	1112.8	0.3	1113.4	0.3
5.8	1243.1	1246.6	0.3	1247.1	0.3
6	1384.2	1385.9	0.2	1387.0	0.1
6.2	1550.4	1553.1	0.4	1556.4	0.2
6.4	1709.6	1711.7	0.2	1713.5	0.1
6.6	1885.3	1874.4	0.1	1882.8	-0.4
6.8	2055.8	2044.1	-0.6	2050.9	-0.2
7	2217.4	2213.0	-0.2	2215.5	-0.2

Appendix D: Simulink Models

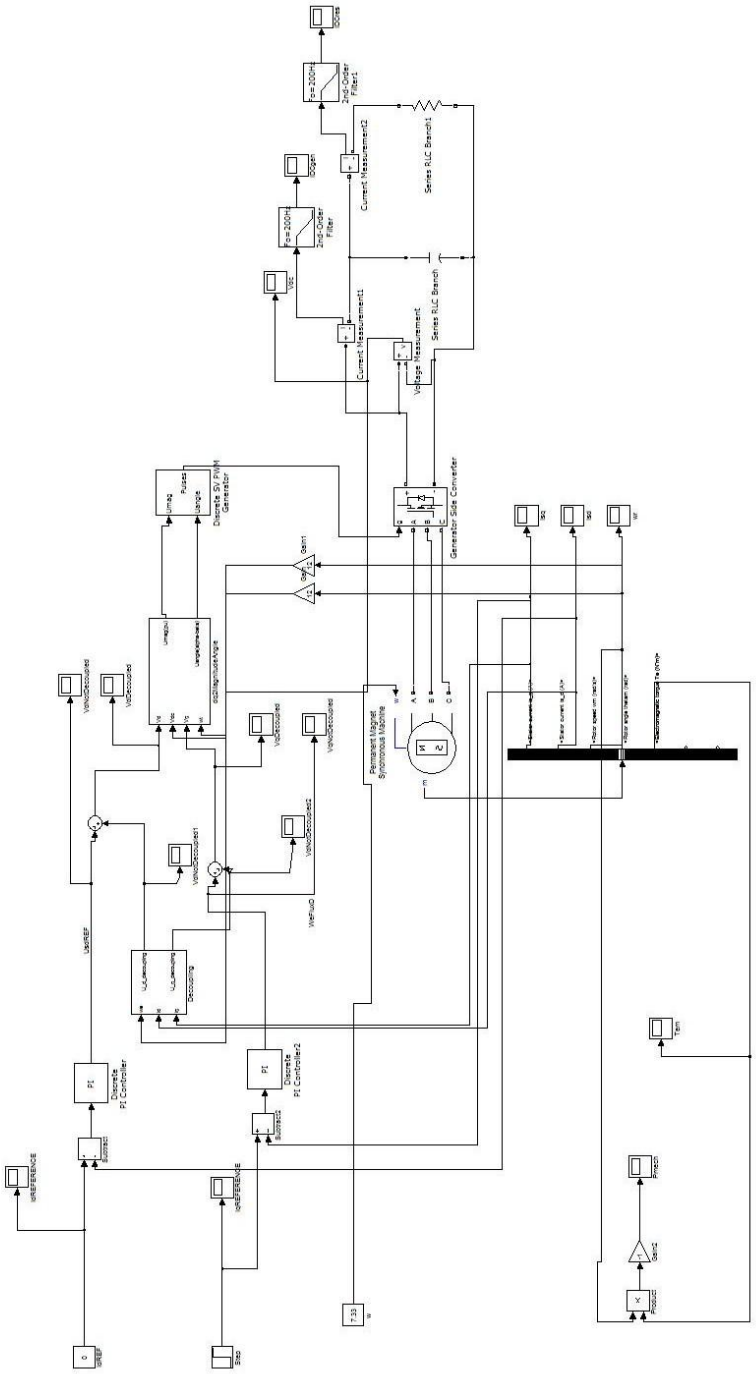

Figure D.1: Simulink Model of the Generator Side Current Control Simulations

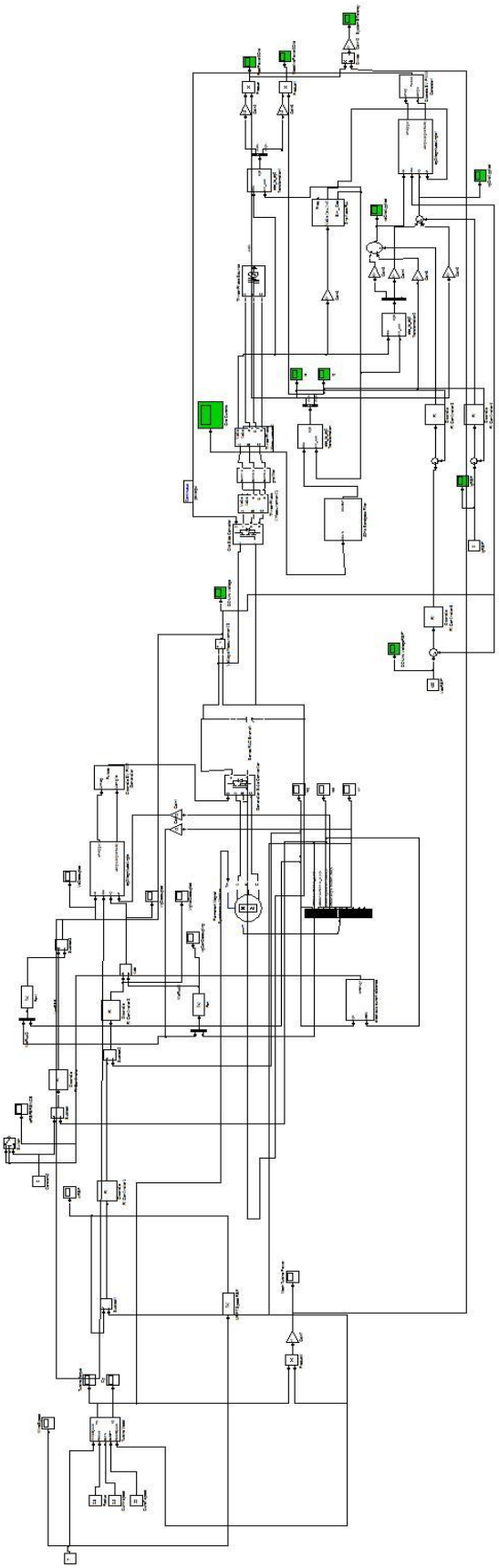

Figure D.2: Simulink Model used in the complete system simulations